UNITED STATES AIR FORCE

1998 SUMMER RESEARCH PROGRAM

GRADUATE STUDENT RESERACH PROGRAM
FINAL REPORTS

VOLUME 8

PHILLIPS LABORATORY

RESEARCH & DEVELOPMENT LABORATORIES

5800 UPLANDER WAY

CULVER CITY, CA 90230-6608

SUBMITTED TO:

COLONEL JAN CERVENY

PROGRAM MANAGER

AIR FORCE OFFICE OF SCIENTIFIC RESEARCH

BOLLING AIR FORCE BASE

WASHINGTON, D.C.

DECEMBER 1998

20010319 038   *AQM01-06-1214*

PREFACE

Reports in this volume are numbered consecutively beginning with number 1. Each report is paginated with the report number followed by consecutive page numbers, e.g., 1-1, 1-2, 1-3; 2-1, 2-2, 2-3.

This document is one of a set of 15 volumes describing the 1998 AFOSR Summer Research Program. The following volumes comprise the set:

VOLUME	TITLE
1	Program Management Report
	Summer Faculty Research Program (SFRP) Reports
2	Armstrong Laboratory
3	Phillips Laboratory
4	Rome Laboratory
5A & 5B	Wright Laboratory
6	Arnold Engineering Development Center, Air Logistics Centers, United States Air Force Academy and Wilford Hall Medical Center
	Graduate Student Research Program (GSRP) Reports
7	Armstrong Laboratory
8	Phillips Laboratory
9	Rome Laboratory
10	Wright Laboratory
11	Arnold Engineering Development Center, and Wilford Hall Medical Center
	High School Apprenticeship Program (HSAP) Reports
12	Armstrong Laboratory
13	Phillips Laboratory
14	Rome Laboratory
15A, 15B & 15C	Wright Laboratory

REPORT DOCUMENTATION PAGE

AFRL-SR-BL-TR-00-

O 784

1. AGENCY USE ONLY *(Leave blank)*	2. REPORT DATE	3. REPORT TYPE AND DATES COVERED
	December, 1998	

4. TITLE AND SUBTITLE
1998 Summer Research Program (SRP), Graduate Student Research Program (GSRP), Final Reports, Volume 8, Phillips Laboratory

5. FUNDING NUMBERS
F49620-93-C-0063

6. AUTHOR(S)
Gary Moore

7. PERFORMING ORGANIZATION NAME(S) AND ADDRESS(ES)
Research & Development Laboratories (RDL)
5800 Uplander Way
Culver City, CA 90230-6608

8. PERFORMING ORGANIZATION REPORT NUMBER

9. SPONSORING/MONITORING AGENCY NAME(S) AND ADDRESS(ES)
Air Force Office of Scientific Research (AFOSR)
801 N. Randolph St.
Arlington, VA 22203-1977

10. SPONSORING/MONITORING AGENCY REPORT NUMBER

11. SUPPLEMENTARY NOTES

12a. DISTRIBUTION AVAILABILITY STATEMENT
Approved for Public Release

12b. DISTRIBUTION CODE

13. ABSTRACT *(Maximum 200 words)*
The United States Air Force Summer Research Program (USAF-SRP) is designed to introduce university, college, and technical institute faculty members, graduate students, and high school students to Air Force research. This is accomplished by the faculty members (Summer Faculty Research Program, (SFRP)), graduate students (Graduate Student Research Program (GSRP)), and high school students (High School Apprenticeship Program (HSAP)) being selected on a nationally advertised competitive basis during the summer intersession period to perform research at Air Force Research Laboratory (AFRL) Technical Directorates, Air Force Air Logistics Centers (ALC), and other AF Laboratories. This volume consists of a program overview, program management statistics, and the final technical reports from the GSRP participants at the Phillips Laboratory.

14. SUBJECT TERMS
Air Force Research, Air Force, Engineering, Laboratories, Reports, Summer, Universities, Faculty, Graduate Student, High School Student

15. NUMBER OF PAGES

16. PRICE CODE

17. SECURITY CLASSIFICATION OF REPORT	18. SECURITY CLASSIFICATION OF THIS PAGE	19. SECURITY CLASSIFICATION OF ABSTRACT	20. LIMITATION OF ABSTRACT
Unclassified	Unclassified	Unclassified	UL

GENERAL INSTRUCTIONS FOR COMPLETING SF 298

The Report Documentation Page (RDP) is used in announcing and cataloging reports. It is important that this information be consistent with the rest of the report, particularly the cover and title page. Instructions for filling in each block of the form follow. It is important to *stay within the lines* to meet *optical scanning requirements.*

Block 1. Agency Use Only *(Leave blank)*.

Block 2. Report Date. Full publication date including day, month, and year, if available
(e.g. 1 Jan 88). Must cite at least the year.

Block 3. Type of Report and Dates Covered. State whether report is interim, final, etc. If applicable, enter inclusive report dates (e.g. 10 Jun 87 - 30 Jun 88).

Block 4. Title and Subtitle. A title is taken from the part of the report that provides the most meaningful and complete information. When a report is prepared in more than one volume, repeat the primary title, add volume number, and include subtitle for the specific volume. On classified documents enter the title classification in parentheses.

Block 5. Funding Numbers. To include contract and grant numbers; may include program element number(s), project number(s), task number(s), and work unit number(s). Use the following labels:

C - Contract	**PR** - Project
G - Grant	**TA** - Task
PE - Program	**WU** - Work Unit
Element	Accession No.

Block 6. Author(s). Name(s) of person(s) responsible for writing the report, performing the research, or credited with the content of the report. If editor or compiler, this should follow the name(s).

Block 7. Performing Organization Name(s) and Address(es).
Self-explanatory.

Block 8. Performing Organization Report Number. Enter the unique alphanumeric report number(s) assigned by the organization performing the report.

Block 9. Sponsoring/Monitoring Agency Name(s) and Address(es).
Self-explanatory.

Block 10. Sponsoring/Monitoring Agency Report Number. *(If known)*

Block 11. Supplementary Notes. Enter information not included elsewhere such as: Prepared in cooperation with....; Trans. of....; To be published in.... When a report is revised, include a statement whether the new report supersedes or supplements the older report.

Block 12a. Distribution/Availability Statement. Denotes public availability or limitations. Cite any availability to the public. Enter additional limitations or special markings in all capitals (e.g. NOFORN, REL, ITAR).

DOD -	See DoDD 5230.24, "Distribution Statements on Technical Documents."
DOE -	See authorities.
NASA -	See Handbook NHB 2200.2.
NTIS -	Leave blank.

Block 12b. Distribution Code.

DOD -	Leave blank.
DOE -	Enter DOE distribution categories from the Standard Distribution for Unclassified Scientific and Technical Reports.
	Leave blank.
NASA -	Leave blank.
NTIS -	

Block 13. Abstract. Include a brief *(Maximum 200 words)* factual summary of the most significant information contained in the report.

Block 14. Subject Terms. Keywords or phrases identifying major subjects in the report.

Block 15. Number of Pages. Enter the total number of pages.

Block 16. Price Code. Enter appropriate price code *(NTIS only)*.

Blocks 17. - 19. Security Classifications. Self- explanatory. Enter U.S. Security Classification in accordance with U.S. Security Regulations (i.e., UNCLASSIFIED). If form contains classified information, stamp classification on the top and bottom of the page.

Block 20. Limitation of Abstract. This block must be completed to assign a limitation to the abstract. Enter either UL (unlimited) or SAR (same as report). An entry in this block is necessary if the abstract is to be limited. If blank, the abstract is assumed to be unlimited.

GSRP FINAL REPORT TABLE OF CONTENTS   i-vi

GSRP FINAL REPORTS

SRP Final Report Table of Contents

SRP Final Report Table of Contents

SRP Final Report Table of Contents

SRP Final Report Table of Contents

SRP Final Report Table of Contents

SRP Final Report Table of Contents

1. INTRODUCTION

The Summer Research Program (SRP), sponsored by the Air Force Office of Scientific Research (AFOSR), offers paid opportunities for university faculty, graduate students, and high school students to conduct research in U.S. Air Force research laboratories nationwide during the summer.

Introduced by AFOSR in 1978, this innovative program is based on the concept of teaming academic researchers with Air Force scientists in the same disciplines using laboratory facilities and equipment not often available at associates' institutions.

The Summer Faculty Research Program (SFRP) is open annually to approximately 150 faculty members with at least two years of teaching and/or research experience in accredited U.S. colleges, universities, or technical institutions. SFRP associates must be either U.S. citizens or permanent residents.

The Graduate Student Research Program (GSRP) is open annually to approximately 100 graduate students holding a bachelor's or a master's degree; GSRP associates must be U.S. citizens enrolled full time at an accredited institution.

The High School Apprentice Program (HSAP) annually selects about 125 high school students located within a twenty mile commuting distance of participating Air Force laboratories.

AFOSR also offers its research associates an opportunity, under the Summer Research Extension Program (SREP), to continue their AFOSR-sponsored research at their home institutions through the award of research grants. In 1994 the maximum amount of each grant was increased from $20,000 to $25,000, and the number of AFOSR-sponsored grants decreased from 75 to 60. A separate annual report is compiled on the SREP.

The numbers of projected summer research participants in each of the three categories and SREP "grants" are usually increased through direct sponsorship by participating laboratories.

AFOSR's SRP has well served its objectives of building critical links between Air Force research laboratories and the academic community, opening avenues of communications and forging new research relationships between Air Force and academic technical experts in areas of national interest, and strengthening the nation's efforts to sustain careers in science and engineering. The success of the SRP can be gauged from its growth from inception (see Table 1) and from the favorable responses the 1997 participants expressed in end-of-tour SRP evaluations (Appendix B).

AFOSR contracts for administration of the SRP by civilian contractors. The contract was first awarded to Research & Development Laboratories (RDL) in September 1990. After completion of the 1990 contract, RDL (in 1993) won the recompetition for the basic year and four 1-year options.

1

2. PARTICIPATION IN THE SUMMER RESEARCH PROGRAM

The SRP began with faculty associates in 1979; graduate students were added in 1982 and high school students in 1986. The following table shows the number of associates in the program each year.

YEAR	SRP Participation, by Year			TOTAL
	SFRP	GSRP	HSAP	
1979	70			70
1980	87			87
1981	87			87
1982	91	17		108
1983	101	53		154
1984	152	84		236
1985	154	92		246
1986	158	100	42	300
1987	159	101	73	333
1988	153	107	101	361
1989	168	102	103	373
1990	165	121	132	418
1991	170	142	132	444
1992	185	121	159	464
1993	187	117	136	440
1994	192	117	133	442
1995	190	115	137	442
1996	188	109	138	435
1997	148	98	140	427
1998	85	40	88	213

Beginning in 1993, due to budget cuts, some of the laboratories weren't able to afford to fund as many associates as in previous years. Since then, the number of funded positions has remained fairly constant at a slightly lower level.

3. RECRUITING AND SELECTION

The SRP is conducted on a nationally advertised and competitive-selection basis. The advertising for faculty and graduate students consisted primarily of the mailing of 8,000 52-page SRP brochures to chairpersons of departments relevant to AFOSR research and to administrators of grants in accredited universities, colleges, and technical institutions. Historically Black Colleges and Universities (HBCUs) and Minority Institutions (MIs) were included. Brochures also went to all participating USAF laboratories, the previous year's participants, and numerous individual requesters (over 1000 annually).

RDL placed advertisements in the following publications: *Black Issues in Higher Education, Winds of Change,* and *IEEE Spectrum.* Because no participants list either *Physics Today* or *Chemical & Engineering News* as being their source of learning about the program for the past several years, advertisements in these magazines were dropped, and the funds were used to cover increases in brochure printing costs.

High school applicants can participate only in laboratories located no more than 20 miles from their residence. Tailored brochures on the HSAP were sent to the head counselors of 180 high schools in the vicinity of participating laboratories, with instructions for publicizing the program in their schools. High school students selected to serve at Wright Laboratory's Armament Directorate (Eglin Air Force Base, Florida) serve eleven weeks as opposed to the eight weeks normally worked by high school students at all other participating laboratories.

Each SFRP or GSRP applicant is given a first, second, and third choice of laboratory. High school students who have more than one laboratory or directorate near their homes are also given first, second, and third choices.

Laboratories make their selections and prioritize their nominees. AFOSR then determines the number to be funded at each laboratory and approves laboratories' selections.

Subsequently, laboratories use their own funds to sponsor additional candidates. Some selectees do not accept the appointment, so alternate candidates are chosen. This multi-step selection procedure results in some candidates being notified of their acceptance after scheduled deadlines. The total applicants and participants for 1998 are shown in this table.

1998 Applicants and Participants			
PARTICIPANT CATEGORY	TOTAL APPLICANTS	SELECTEES	DECLINING SELECTEES
SFRP	382	85	13
(HBCU/MI)	(0)	(0)	(0)
GSRP	130	40	7
(HBCU/MI)	(0)	(0)	(0)
HSAP	328	88	22
TOTAL	840	213	42

4.   SITE VISITS

During June and July of 1998, representatives of both AFOSR/NI and RDL visited each participating laboratory to provide briefings, answer questions, and resolve problems for both laboratory personnel and participants. The objective was to ensure that the SRP would be as constructive as possible for all participants. Both SRP participants and RDL representatives found these visits beneficial. At many of the laboratories, this was the only opportunity for all participants to meet at one time to share their experiences and exchange ideas.

5.   HISTORICALLY BLACK COLLEGES AND UNIVERSITIES AND MINORITY INSTITUTIONS (HBCU/MIs)

Before 1993, an RDL program representative visited from seven to ten different HBCU/MIs annually to promote interest in the SRP among the faculty and graduate students. These efforts were marginally effective, yielding a doubling of HBCI/MI applicants. In an effort to achieve AFOSR's goal of 10% of all applicants and selectees being HBCU/MI qualified, the RDL team decided to try other avenues of approach to increase the number of qualified applicants. Through the combined efforts of the AFOSR Program Office at Bolling AFB and RDL, two very active minority groups were found, HACU (Hispanic American Colleges and Universities) and AISES (American Indian Science and Engineering Society). RDL is in communication with representatives of each of these organizations on a monthly basis to keep up with the their activities and special events. Both organizations have widely-distributed magazines/quarterlies in which RDL placed ads.

Since 1994 the number of both SFRP and GSRP HBCU/MI applicants and participants has increased ten-fold, from about two dozen SFRP applicants and a half dozen selectees to over 100 applicants and two dozen selectees, and a half-dozen GSRP applicants and two or three selectees to 18 applicants and 7 or 8 selectees. Since 1993, the SFRP had a two-fold applicant increase and a two-fold selectee increase. Since 1993, the GSRP had a three-fold applicant increase and a three to four-fold increase in selectees.

In addition to RDL's special recruiting efforts, AFOSR attempts each year to obtain additional funding or use leftover funding from cancellations the past year to fund HBCU/MI associates.

SRP HBCU/MI Participation, By Year				
YEAR	SFRP		GSRP	
	Applicants	Participants	Applicants	Participants
1985	76	23	15	11
1986	70	18	20	10
1987	82	32	32	10
1988	53	17	23	14
1989	39	15	13	4
1990	43	14	17	3
1991	42	13	8	5
1992	70	13	9	5
1993	60	13	6	2
1994	90	16	11	6
1995	90	21	20	8
1996	119	27	18	7

6.   SRP FUNDING SOURCES

Funding sources for the 1998 SRP were the AFOSR-provided slots for the basic contract and laboratory funds. Funding sources by category for the 1998 SRP selected participants are shown here.

1998 SRP FUNDING CATEGORY	SFRP	GSRP	HSAP
AFOSR Basic Allocation Funds	67	38	75
USAF Laboratory Funds	17	2	13
Slots Added by AFOSR (Leftover Funds)	0	0	0
HBCU/MI By AFOSR (Using Procured Addn'l Funds)	0	0	N/A
TOTAL	84	40	88

7. COMPENSATION FOR PARTICIPANTS

Compensation for SRP participants, per five-day work week, is shown in this table.

1998 SRP Associate Compensation

PARTICIPANT CATEGORY	1991	1992	1993	1994	1995	1996	1997	1998
Faculty Members	$690	$718	$740	$740	$740	$770	$770	$793
Graduate Student (Master's Degree)	$425	$442	$455	$455	$455	$470	$470	$484
Graduate Student (Bachelor's Degree)	$365	$380	$391	$391	$391	$400	$400	$412
High School Student (First Year)	$200	$200	$200	$200	$200	$200	$200	$200
High School Student (Subsequent Years)	$240	$240	$240	$240	$240	$240	$240	$240

The program also offered associates whose homes were more than 50 miles from the laboratory an expense allowance (seven days per week) of $52/day for faculty and $41/day for graduate students. Transportation to the laboratory at the beginning of their tour and back to their home destinations at the end was also reimbursed for these participants. Of the combined SFRP and GSRP associates, 65 % claimed travel reimbursements at an average round-trip cost of $730.

Faculty members were encouraged to visit their laboratories before their summer tour began. All costs of these orientation visits were reimbursed. Forty-three percent (85 out of 188) of faculty associates took orientation trips at an average cost of $449. By contrast, in 1993, 58 % of SFRP associates elected to take an orientation visits at an average cost of $685; that was the highest

percentage of associates opting to take an orientation trip since RDL has administered the SRP, and the highest average cost of an orientation trip.

Program participants submitted biweekly vouchers countersigned by their laboratory research focal point, and RDL issued paychecks so as to arrive in associates' hands two weeks later.

This is the third year of using direct deposit for the SFRP and GSRP associates. The process went much more smoothly with respect to obtaining required information from the associates, about 15% of the associates' information needed clarification in order for direct deposit to properly function as opposed to 7% from last year. The remaining associates received their stipend and expense payments via checks sent in the US mail.

HSAP program participants were considered actual RDL employees, and their respective state and federal income tax and Social Security were withheld from their paychecks. By the nature of their independent research, SFRP and GSRP program participants were considered to be consultants or independent contractors. As such, SFRP and GSRP associates were responsible for their own income taxes, Social Security, and insurance.

8. CONTENTS OF THE 1998 REPORT

The complete set of reports for the 1998 SRP includes this program management report (Volume 1) augmented by fifteen volumes of final research reports by the 1998 associates, as indicated below:

1998 SRP Final Report Volume Assignments

LABORATORY	SFRP	GSRP	HSAP
Armstrong	2	7	12
Phillips	3	8	13
Rome	4	9	14
Wright	5A, 5B	10	15
AEDC, ALCs, USAFA, WHMC	6	11	

APPENDIX A -- PROGRAM STATISTICAL SUMMARY

A. Colleges/Universities Represented

Selected SFRP associates represented 169 different colleges, universities, and institutions, GSRP associates represented 95 different colleges, universities, and institutions.

B. States Represented

SFRP -Applicants came from 47 states plus Washington D.C. Selectees represent 44 states.

GSRP - Applicants came from 44 states. Selectees represent 32 states.

HSAP - Applicants came from thirteen states. Selectees represent nine states.

Total Number of Participants	
SFRP	85
GSRP	40
HSAP	88
TOTAL	213

Degrees Represented			
	SFRP	GSRP	TOTAL
Doctoral	83	0	83
Master's	1	3	4
Bachelor's	0	22	22
TOTAL	186	25	109

SFRP Academic Titles	
Assistant Professor	36
Associate Professor	34
Professor	15
Instructor	0
Chairman	0
Visiting Professor	0
Visiting Assoc. Prof.	0
Research Associate	0
TOTAL	85

Source of Learning About the SRP		
Category	Applicants	Selectees
Applied/participated in prior years	177	47
Colleague familiar with SRP	104	24
Brochure mailed to institution	101	21
Contact with Air Force laboratory	101	39
IEEE Spectrum	12	1
BIIHE	4	0
Other source	117	30
TOTAL	616	162

APPENDIX B -- SRP EVALUATION RESPONSES

1. OVERVIEW

Evaluations were completed and returned to RDL by four groups at the completion of the SRP. The number of respondents in each group is shown below.

Table B-1. Total SRP Evaluations Received

Evaluation Group	Responses
SFRP & GSRPs	100
HSAPs	75
USAF Laboratory Focal Points	84
USAF Laboratory HSAP Mentors	6

All groups indicate unanimous enthusiasm for the SRP experience.

The summarized recommendations for program improvement from both associates and laboratory personnel are listed below:

A.   Better preparation on the labs' part prior to associates' arrival (i.e., office space, computer assets, clearly defined scope of work).

B.   Faculty Associates suggest higher stipends for SFRP associates.

C.   Both HSAP Air Force laboratory mentors and associates would like the summer tour extended from the current 8 weeks to either 10 or 11 weeks; the groups state it takes 4-6 weeks just to get high school students up-to-speed on what's going on at laboratory. (Note: this same argument was used to raise the faculty and graduate student participation time a few years ago.)

2. 1998 USAF LABORATORY FOCAL POINT (LFP) EVALUATION RESPONSES

The summarized results listed below are from the 84 LFP evaluations received.

1. LFP evaluations received and associate preferences:

Table B-2. Air Force LFP Evaluation Responses (By Type)

| | | How Many Associates Would You Prefer To Get ? | | | | | | | | (% Response) | | | |
| | | SFRP | | | | GSRP (w/Univ Professor) | | | | GSRP (w/o Univ Professor) | | | |
Lab	Evals Recv'd	0	1	2	3+	0	1	2	3+	0	1	2	3+
AEDC	0	-	-	-	-	-	-	-	-	-	-	-	-
WHMC	0	-	-	-	-	-	-	-	-	-	-	-	-
AL	7	28	28	28	14	54	14	28	0	86	0	14	0
USAFA	1	0	100	0	0	100	0	0	0	0	100	0	0
PL	25	40	40	16	4	88	12	0	0	84	12	4	0
RL	5	60	40	0	0	80	10	0	0	100	0	0	0
WL	46	30	43	20	6	78	17	4	0	93	4	2	0
Total	84	32%	50%	13%	5%	80%	11%	6%	0%	73%	23%	4%	0%

LFP Evaluation Summary. The summarized responses, by laboratory, are listed on the following page. LFPs were asked to rate the following questions on a scale from 1 (below average) to 5 (above average).

2. LFPs involved in SRP associate application evaluation process:
   a. Time available for evaluation of applications:
   b. Adequacy of applications for selection process:
3. Value of orientation trips:
4. Length of research tour:
5 a. Benefits of associate's work to laboratory:
   b. Benefits of associate's work to Air Force:
6. a. Enhancement of research qualifications for LFP and staff:
   b. Enhancement of research qualifications for SFRP associate:
   c. Enhancement of research qualifications for GSRP associate:
7. a. Enhancement of knowledge for LFP and staff:
   b. Enhancement of knowledge for SFRP associate:
   c. Enhancement of knowledge for GSRP associate:
8. Value of Air Force and university links:
9. Potential for future collaboration:
10. a. Your working relationship with SFRP:
    b. Your working relationship with GSRP:
11. Expenditure of your time worthwhile:

12. Quality of program literature for associate:
13.   a. Quality of RDL's communications with you:
        b. Quality of RDL's communications with associates:
14. Overall assessment of SRP:

Table B-3. Laboratory Focal Point Reponses to above questions

	AEDC	AL	USAF A	PL	RL	WHMC	WL
# Evals Recv'd	0	7	1	14	5	0	46
Question #							
2	-	86 %	0 %	88 %	80 %	-	85 %
2a	-	4.3	n/a	3.8	4.0	-	3.6
2b	-	4.0	n/a	3.9	4.5	-	4.1
3	-	4.5	n/a	4.3	4.3	-	3.7
4	-	4.1	4.0	4.1	4.2	-	3.9
5a	-	4.3	5.0	4.3	4.6	-	4.4
5b	-	4.5	n/a	4.2	4.6	-	4.3
6a	-	4.5	5.0	4.0	4.4	-	4.3
6b	-	4.3	n/a	4.1	5.0	-	4.4
6c	-	3.7	5.0	3.5	5.0	-	4.3
7a	-	4.7	5.0	4.0	4.4	-	4.3
7b	-	4.3	n/a	4.2	5.0	-	4.4
7c	-	4.0	5.0	3.9	5.0	-	4.3
8	-	4.6	4.0	4.5	4.6	-	4.3
9	-	4.9	5.0	4.4	4.8	-	4.2
10a	-	5.0	n/a	4.6	4.6	-	4.6
10b	-	4.7	5.0	3.9	5.0	-	4.4
11	-	4.6	5.0	4.4	4.8	-	4.4
12	-	4.0	4.0	4.0	4.2	-	3.8
13a	-	3.2	4.0	3.5	3.8	-	3.4
13b	-	3.4	4.0	3.6	4.5	-	3.6
14	-	4.4	5.0	4.4	4.8	-	4.4

3. 1998 SFRP & GSRP EVALUATION RESPONSES

The summarized results listed below are from the 120 SFRP/GSRP evaluations received.

Associates were asked to rate the following questions on a scale from 1 (below average) to 5 (above average) - by Air Force base results and over-all results of the 1998 evaluations are listed after the questions.

1. The match between the laboratories research and your field:
2. Your working relationship with your LFP:
3. Enhancement of your academic qualifications:
4. Enhancement of your research qualifications:
5. Lab readiness for you: LFP, task, plan:
6. Lab readiness for you: equipment, supplies, facilities:
7. Lab resources:
8. Lab research and administrative support:
9. Adequacy of brochure and associate handbook:
10. RDL communications with you:
11. Overall payment procedures:
12. Overall assessment of the SRP:
13.   a. Would you apply again?
         b. Will you continue this or related research?
14. Was length of your tour satisfactory?
15. Percentage of associates who experienced difficulties in finding housing:
16. Where did you stay during your SRP tour?
         a.   At Home:
         b.   With Friend:
         c.   On Local Economy:
         d.   Base Quarters:
17. Value of orientation visit:
         a.   Essential:
         b.   Convenient:
         c.   Not Worth Cost:
         d.   Not Used:

SFRP and GSRP associate's responses are listed in tabular format on the following page.

Table B-4. 1997 SFRP & GSRP Associate Responses to SRP Evaluation

	Arnold	Brooks	Edwards	Eglin	Griffis	Hanscom	Kelly	Kirtland	Lackland	Robins	Tyndall	WPAFB	average
# res	6	48	6	14	31	19	3	32	1	2	10	85	257
1	4.8	4.4	4.6	4.7	4.4	4.9	4.6	4.6	5.0	5.0	4.0	4.7	4.6
2	5.0	4.6	4.1	4.9	4.7	4.7	5.0	4.7	5.0	5.0	4.6	4.8	4.7
3	4.5	4.4	4.0	4.6	4.3	4.2	4.3	4.4	5.0	5.0	4.5	4.3	4.4
4	4.3	4.5	3.8	4.6	4.4	4.4	4.3	4.6	5.0	4.0	4.4	4.5	4.5
5	4.5	4.3	3.3	4.8	4.4	4.5	4.3	4.2	5.0	5.0	3.9	4.4	4.4
6	4.3	4.3	3.7	4.7	4.4	4.5	4.0	3.8	5.0	5.0	3.8	4.2	4.2
7	4.5	4.4	4.2	4.8	4.5	4.3	4.3	4.1	5.0	5.0	4.3	4.3	4.4
8	4.5	4.6	3.0	4.9	4.4	4.3	4.3	4.5	5.0	5.0	4.7	4.5	4.5
9	4.7	4.5	4.7	4.5	4.3	4.5	4.7	4.3	5.0	5.0	4.1	4.5	4.5
10	4.2	4.4	4.7	4.4	4.1	4.1	4.0	4.2	5.0	4.5	3.6	4.4	4.3
11	3.8	4.1	4.5	4.0	3.9	4.1	4.0	4.0	3.0	4.0	3.7	4.0	4.0
12	5.7	4.7	4.3	4.9	4.5	4.9	4.7	4.6	5.0	4.5	4.6	4.5	4.6
Numbers below are percentages													
13a	83	90	83	93	87	75	100	81	100	100	100	86	87
13b	100	89	83	100	94	98	100	94	100	100	100	94	93
14	83	96	100	90	87	80	100	92	100	100	70	84	88
15	17	6	0	33	20	76	33	25	0	100	20	8	39
16a	-	26	17	9	38	23	33	4	-	-	-	30	
16b	100	33	-	40	-	8	-	-	-	-	36	2	
16c	-	41	83	40	62	69	67	96	100	100	64	68	
16d	-	-	-	-	-	-	-	-	-	-	-	0	
17a	-	33	100	17	50	14	67	39	-	50	40	31	35
17b	-	21	-	17	10	14	-	24	-	50	20	16	16
17c	-	-	-	-	10	7	-	-	-	-	-	2	3
17d	100	46	-	66	30	69	33	37	100	-	40	51	46

4. 1998 USAF LABORATORY HSAP MENTOR EVALUATION RESPONSES

Not enough evaluations received (5 total) from Mentors to do useful summary.

5. 1998 HSAP EVALUATION RESPONSES

The summarized results listed below are from the 23 HSAP evaluations received.

HSAP apprentices were asked to rate the following questions on a scale from
1 (below average) to 5 (above average)

1. Your influence on selection of topic/type of work.
2. Working relationship with mentor, other lab scientists.
3. Enhancement of your academic qualifications.
4. Technically challenging work.
5. Lab readiness for you: mentor, task, work plan, equipment.
6. Influence on your career.
7. Increased interest in math/science.
8. Lab research & administrative support.
9. Adequacy of RDL's Apprentice Handbook and administrative materials.
10. Responsiveness of RDL communications.
11. Overall payment procedures.
12. Overall assessment of SRP value to you.
13. Would you apply again next year?   Yes (92 %)
14. Will you pursue future studies related to this research?   Yes (68 %)
15. Was Tour length satisfactory?   Yes (82 %)

	Arnold	Brooks	Edwards	Eglin	Griffiss	Hanscom	Kirtland	Tyndall	WPAFB	Totals
# resp	5	19	7	15	13	2	7	5	40	113
1	2.8	3.3	3.4	3.5	3.4	4.0	3.2	3.6	3.6	3.4
2	4.4	4.6	4.5	4.8	4.6	4.0	4.4	4.0	4.6	4.6
3	4.0	4.2	4.1	4.3	4.5	5.0	4.3	4.6	4.4	4.4
4	3.6	3.9	4.0	4.5	4.2	5.0	4.6	3.8	4.3	4.2
5	4.4	4.1	3.7	4.5	4.1	3.0	3.9	3.6	3.9	4.0
6	3.2	3.6	3.6	4.1	3.8	5.0	3.3	3.8	3.6	3.7
7	2.8	4.1	4.0	3.9	3.9	5.0	3.6	4.0	4.0	3.9
8	3.8	4.1	4.0	4.3	4.0	4.0	4.3	3.8	4.3	4.2
9	4.4	3.6	4.1	4.1	3.5	4.0	3.9	4.0	3.7	3.8
10	4.0	3.8	4.1	3.7	4.1	4.0	3.9	2.4	3.8	3.8
11	4.2	4.2	3.7	3.9	3.8	3.0	3.7	2.6	3.7	3.8
12	4.0	4.5	4.9	4.6	4.6	5.0	4.6	4.2	4.3	4.5
Numbers below are percentages										
13	60%	95%	100%	100%	85%	100%	100%	100%	90%	92%
14	20%	80%	71%	80%	54%	100%	71%	80%	65%	68%
15	100%	70%	71%	100%	100%	50%	86%	60%	80%	82%

A STUDY OF OPTIMAL FINITE–THRUST SPACECRAFT TRAJECTORIES FOR THE TECHSAT 21 MISSION

Benjamin J. Bernocco
Graduate Student
Department of Aerospace Engineering

The Pennsylvania State University
233 Hammond Building
University Park, PA 16802

1-1

A STUDY OF OPTIMAL FINITE–THRUST SPACECRAFT TRAJECTORIES FOR THE TECHSAT 21 MISSION

Benjamin J. Bernocco
Graduate Student
Department of Aerospace Engineering
The Pennsylvania State University

Abstract

A preliminary study of optimal finite-thrust spacecraft trajectories for the TechSat 21 mission was examined. The study looked only at one satellite orbiting in the ecliptic plane, i.e. two-dimensional motion, with no explicit orbit perturbations included. Optimization of the spacecraft trajectory was accomplished using a direct collocation with nonlinear programming approach. This approach requires that the equations of motion and integrals of the motion for the spacecraft trajectory be calculated from state vector values and then feed into an optimization subroutine. The optimization subroutine changes the state vector values to minimize the objective function, i.e. the thruster firing time, which is subject to constraints dictated by the mission requirements. An example simulation for this mission was performed. The trajectory was divided up into a sequence of twelve thrust arcs separated by twelve coast arcs. Constraints were placed on the objective function to insure that the state vector values yielded results that represented an actual, predetermined trajectory. A general perturbation was incorporated into the problem by including thrust acceleration terms in the equations of motion. The initial conditions used to start the process were chosen to be the state vector values for a pure Keplerian orbit with no perturbations. After only two iterations the code converged to an optimized solution. This solution was very close to the initial condition with only the thrust level and thruster firing times being altered by the program. It is a reasonable solution since the thrusters are only used to maintain the same orbit, hence most of the state vector values would not change. The solution was plugged back into the code as initial conditions and the code yielded the same solution after one iteration. Although this does not guarantee a global minimum was found, it instills confidence that the solution is a valid one. Future work to be done includes expanding the code to three dimensions, including perturbation effects like atmospheric drag, luni-solar, and the Earth's oblateness, and including multiple satellites in the analysis.

A STUDY OF OPTIMAL FINITE–THRUST SPACECRAFT TRAJECTORIES FOR THE TECHSAT 21 MISSION

Benjamin J. Bernocco

Introduction

The Air Force is currently looking for new technologies to take it into the twenty-first century. One of those technologies high on the Air Force's list is Space-Based Radar (SBR). SBR will provide the Air Force with a virtual presence that will allow constant monitoring of situations around the globe. It will be able to provide theater-wide, near real-time, undeniable, all-weather, and round-the-clock surveillance of any place on the globe. The TechSat 21 program was setup to help make the concept of SBR a reality for the twenty-first century. It will consist of clusters of small, lightweight formation flying satellites. These satellite clusters will form a virtual satellite that functions cooperatively as a multiple aperture sparse array. This array would be capable of active sensing, communications, and passive radiometry. Each satellite in a cluster could receive its own as well as other satellites' radar pulses. The radar pulses are of different frequencies and each satellite performs range/Doppler and angle of arrival processing on the pulses [1]. In order to maximize data collection time of radar signals, the thruster firing time of the satellite must be minimized. The optimization of finite-thrust spacecraft trajectories can be accomplished by a method using direct collocation with nonlinear programming.

Methodology

This study deals with the optimization of finite-thrust spacecraft trajectories by using the direct collocation with nonlinear programming (DCNLP) approach. A complete history of the development of the DCNLP approach can be found in references 2 and 3. The DCNLP approach approximates the spacecraft trajectory with piecewise polynomials that are represented by state and control variables at a given number of nodes. State variables are stored in the state vector x and the control variables are stored in the control vector u. The spacecraft trajectory is divided up into a series of thrust arcs and coast arcs and the thrust arcs are subdivided into evenly spaced segments. Thrust arcs and coast arcs require different means of evaluation. In a thrust arc segment each state variable has a state trajectory which is taken to be a Hermite cubic. This is a "unique cubic that goes through the endpoints of the thrust segment with the appropriate derivatives that are dictated by the evaluation of the differential equations of

motion at the endpoints" [2]. Each control variable is assumed to have a linear control trajectory across the thrust segment. At the center of each thrust segment a collocation point is found and then the difference between the derivative of the Hermite cubic at the collocation point and the trajectory equations of motion evaluated at the collocation point is calculated. This difference is called the defect and it is one of the constraints that the objective function, the thruster firing time, is subject to. When the defect is zero the differential equations of motion are satisfied at the collocation point and the endpoints. Allowing the trajectory equations of motion to be given by $\dot{x} = f(x,u)$ and the length of time of a thrust segment to be T, the Hermite interpolated state vector at the collocation point is given by

$$x_c = (1/2){\cdot}(x_l + x_r) + (T/8){\cdot}[f(x_l, u_l) - f(x_r, u_r)] \tag{1}$$

where x_l and x_r are the state vectors at the left and right nodes. The linearly interpolated control vector is given by

$$u_c = (1/2){\cdot}(u_l + u_r) \tag{2}$$

where u_l and u_r are the control vectors at the left and right nodes. The derivative of the Hermite interpolated state vector at the collocation point is

$$\dot{x}_c = -[3/(2{\cdot}T)]{\cdot}(x_l - x_r) - (1/4){\cdot}[f(x_l, u_l) + f(x_r, u_r)] \tag{3}$$

Finally, the defect vector is

$$\mathbf{d} = f(x_c, u_c) - \dot{x}_c \tag{4}$$

where both the equations of motion and the derivative of the Hermite interpolated state vector are evaluated at the collocation point [2],[3].

For the case of two-dimensional motion, which this study focuses on, there are five state variables and one control variable. Based on this information there will be five equations of motion for the system. In polar coordinates using canonical units ($\mu = 1.0$) the two-dimensional equations of motion are

$$\dot{x}_1 = x_3 \tag{5a}$$

$$\dot{x}_2 = x_4 / x_1 \tag{5b}$$

$$\dot{x}_3 = x_4^2 / x_1 - 1 / x_1^2 + x_5 {\cdot}\sin(u_1) \tag{5c}$$

$$\dot{x}_4 = -x_3{\cdot}x_4 / x_1 + x_5 {\cdot}\cos(u_1) \tag{5d}$$

$$\dot{x}_5 = x_5^2 / c \tag{5e}$$

1-4

where x_1 is the orbital radius, x_2 is the true anomaly, x_3 is the velocity component along the radial direction, x_4 is the velocity component along the local horizontal direction, x_5 is the magnitude of the thrust acceleration, u_1 is the thrust vector angle measured from the local horizontal direction, and c is the rocket exhaust velocity [2],[4],[5].

A coast arc is handled differently from a thrust arc since its solution can be determined analytically. For a coast arc, integrals of the motion are calculated at the left and right endpoints of the arc and then subtracted to yield a generalized defect. When the generalized defect is zero, the integrals of motion at the left and right endpoints of the coast arc are equal. For the case of two-dimensional motion four integrals of the motion are needed. The integrals of motion chosen for this study are angular momentum, specific energy, longitude of periapsis, and the fact that the thrust acceleration must be zero across the coast arc [2]. The two-dimensional integrals of the motion in polar coordinates using canonical units ($\mu = 1.0$) are

$$Q_1(x) = x_1 \cdot x_4 \tag{6a}$$

$$Q_2(x) = (x_3^2 + x_4^2) / 2.0 - 1.0 / x_1 \tag{6b}$$

$$Q_3(x) = x_2 + \tan^{-1}[-x_3 \cdot x_4 / (x_4^2 - 1.0 / x_1)] \tag{6c}$$

$$Q_4(x) = x_5 \tag{6d}$$

where $Q_1(x)$ is the angular momentum of the orbit, $Q_2(x)$ is the specific energy of the orbit, $Q_3(x)$ is the longitude of periapsis of the orbit, and $Q_4(x)$ is the thrust magnitude [2],[4],[5]. The generalized defect for the integrals of the motion is written as

$$\mathbf{q} = \mathbf{Q}(x_l) - \mathbf{Q}(x_r) \tag{7}$$

Besides the defect and generalized defect vectors, equality and inequality constraints can also be added to the analysis. These are totally up the user and can include things like constraints on the initial or final conditions or path constraints. All of the defects and constraints are used as bounds on the objective function, what you want to minimize. In the case of spacecraft trajectories the objective function is the sum of the thrust arc durations. The state, control, and defect variables for both thrust and coast arcs plus any other problem constraints make up a nonlinear programming problem. To solve this problem the variables must first be assembled into state and constraint vectors. The state and control vectors and the thrust arc duration time are assembled into the nonlinear programming (NLP) state vector as follows

$$X^T = [\; x_1^T, u_1^T, x_2^T, u_2^T, \dots, x_n^T, u_n^T, t_1, t_2, \dots, t_k] \tag{8}$$

1-5

where $\mathcal{X}$ is the NLP state vector, n is the number of nodes that the trajectory is divided into, t is the thrust arc duration time, and k is the number of thrust arcs on the trajectory [2]. The defects, generalized defects, equality constraints, and inequality constraints are assembled into the NLP constraint vector as follows

$$\mathbf{C^T} = [\ \mathbf{d_1}, \mathbf{q_1}, \mathbf{d_2}, \mathbf{q_2}, ..., \mathbf{d_m}, \mathbf{q_p}, h_1, h_2, ..., h_j, g_1, g_2, ..., g_i] \qquad (9)$$

where **C** is the NLP constraint vector, m is the number thrust arc segments, p is the number of coast arcs, h are the equality constraints, j is the number of equality constraints, g are inequality constraints, and i is the number of inequality constraints [2]. The NLP state vector must always be larger in length than the NLP constraint vector or an optimized solution will not be found. Once the NLP state and constraint vectors are found, a solution can be computed by placing these vectors into an optimization subroutine.

For this study the optimization subroutine used was the Sequential Quadratic Programming (SQP) subroutine [6]. This subroutine approximates the nonlinear problem with a sequence of quadratic programming problems. It minimizes the objective function subject to making the defects and constraints values as small as possible. The SQP subroutine must be provided with the initial state and control conditions and with subroutines that evaluate the trajectory equations of motion, the Hermite cubic and its derivative, the thrust arc defects, the generalized defects, any constraints included, and the objective function. It also requires the size of the NLP state and constraint vectors as a check to make sure that the problem is solvable.

The two-dimensional TechSat 21 example was setup using the following orbital parameters in canonical units ($\mu = 1.0$): 1) the orbital period equals 2π TU; 2) the semi-major axis equals 1.1098 DU/TU; 3) the eccentricity equals 0.0096; 4) the Earth's gravitational constant at sea level equals 1.00 DU/TU^2; and 5) the rocket engine specific impulse equals 0.37183 TU. One DU equals 6378.1 km and one TU equals 806.811 seconds. The trajectory was divided into twelve thrust arcs and twelve coast arcs with each thrust arc divided into four equal segments. This arrangement occurs over a two-year period and results in a trajectory composed of sixty nodes. The equality constraints used required that the initial and final eccentricity, angular momentum, and specific energy calculated from the state and control variables must equal the actual values for the orbit described above. No inequality constraints were used for this study. The initial conditions for the orbit were based on a perfectly Keplerian orbit and the thrust level and angle were randomly guessed at. Results based on this setup follow.

Results

The initial conditions in Table 1 below were input into the SQP subroutine, which then optimized the state and control values to yield a minimum thruster firing time.

Table 1: Trajectory Initial Conditions for the SQP Subroutine

| Orbit Radius (DU)	True Anomaly (rad.)	Thrust (kg-DU/TU^2)	Thrust Angle (rad.)	Thrust Firing Time (TU)	Orbit Radius (DU)	True Anomaly (rad.)	Thrust (kg-DU/TU^2)	Thrust Angle (rad.)	Thrust Firing Time (TU)
1.088648	0.0000	8.00E-32	-0.5236	0.1	1.088648	6.2832	8.00E-32	-0.5236	0.1
1.088868	0.2094	8.00E-32	-0.5236	0.1	1.088868	6.4926	8.00E-32	-0.5236	0.1
1.089527	0.4189	8.00E-32	-0.5236	0.1	1.089527	6.7021	8.00E-32	-0.5236	0.1
1.090626	0.6283	8.00E-32	-0.5236	0.1	1.090626	6.9115	8.00E-32	-0.5236	0.1
1.092055	0.8378	0.00E+00	0	0	1.092055	7.1209	0.00E+00	0	0
1.093814	1.0472	8.00E-32	-0.5236	0.1	1.093814	7.3304	8.00E-32	-0.5236	0.1
1.095902	1.2566	8.00E-32	-0.5236	0.1	1.095902	7.5398	8.00E-32	-0.5236	0.1
1.097991	1.4661	8.00E-32	-0.5236	0.1	1.097991	7.7493	8.00E-32	-0.5236	0.1
1.100189	1.6755	8.00E-32	-0.5236	0.1	1.100189	7.9587	8.00E-32	-0.5236	0.1
1.102388	1.8850	0.00E+00	0	0	1.102388	8.1681	0.00E+00	0	0
1.104366	2.0944	8.00E-32	-0.5236	0.1	1.104366	8.3776	8.00E-32	-0.5236	0.1
1.106235	2.3038	8.00E-32	-0.5236	0.1	1.106235	8.5870	8.00E-32	-0.5236	0.1
1.107664	2.5133	8.00E-32	-0.5236	0.1	1.107664	8.7965	8.00E-32	-0.5236	0.1
1.108873	2.7227	8.00E-32	-0.5236	0.1	1.108873	9.0059	8.00E-32	-0.5236	0.1
1.109532	2.9322	0.00E+00	0	0	1.109532	9.2153	0.00E+00	0	0
1.109752	3.1416	8.00E-32	-0.5236	0.1	1.109752	9.4248	8.00E-32	-0.5236	0.1
1.109532	3.3510	8.00E-32	-0.5236	0.1	1.109532	9.6342	8.00E-32	-0.5236	0.1
1.108873	3.5605	8.00E-32	-0.5236	0.1	1.108873	9.8437	8.00E-32	-0.5236	0.1
1.107664	3.7699	8.00E-32	-0.5236	0.1	1.107664	10.0531	8.00E-32	-0.5236	0.1
1.106235	3.9794	0.00E+00	0	0	1.106235	10.2625	0.00E+00	0	0
1.104366	4.1888	8.00E-32	-0.5236	0.1	1.104366	10.4720	8.00E-32	-0.5236	0.1
1.102388	4.3982	8.00E-32	-0.5236	0.1	1.102388	10.6814	8.00E-32	-0.5236	0.1
1.100189	4.6077	8.00E-32	-0.5236	0.1	1.100189	10.8909	8.00E-32	-0.5236	0.1
1.097991	4.8171	8.00E-32	-0.5236	0.1	1.097991	11.1003	8.00E-32	-0.5236	0.1
1.095902	5.0265	0.00E+00	0	0	1.095902	11.3097	0.00E+00	0	0
1.093814	5.2360	8.00E-32	-0.5236	0.1	1.093814	11.5192	8.00E-32	-0.5236	0.1
1.092055	5.4454	8.00E-32	-0.5236	0.1	1.092055	11.7286	8.00E-32	-0.5236	0.1
1.090626	5.6549	8.00E-32	-0.5236	0.1	1.090626	11.9381	8.00E-32	-0.5236	0.1
1.089527	5.8643	8.00E-32	-0.5236	0.1	1.089527	12.1475	8.00E-32	-0.5236	0.1
1.088868	6.0737	0.00E+00	0	0	1.088868	12.3569	0.00E+00	0	0

This data was plugged into the SQP subroutine along with the subroutines needed for the DCNLP calculations and after only two iterations it converged to an optimized solution. The optimized trajectory values are shown in Table 2.

Table 2: Optimized Trajectory Values

Orbit Radius (DU)	True Anomaly (rad.)	Thrust (kg-DU/TU²)	Thrust Angle (rad.)	Thrust Firing Time (TU)	Orbit Radius (DU)	True Anomaly (rad.)	Thrust (kg-DU/TU²)	Thrust Angle (rad.)	Thrust Firing Time (TU)
1.088648	0.0880	2.11E-05	0.4363	0.1568	1.096672	6.4667	2.47E-05	0.4363	0.1350
1.089527	0.2240	2.11E-05	0.4363	0.1568	1.096892	6.5568	2.49E-05	0.4363	0.1350
1.090736	0.3599	2.11E-05	0.4363	0.1568	1.097221	6.6469	2.50E-05	0.4363	0.1350
1.092165	0.4958	2.09E-05	0.4363	0.1568	1.097771	6.7369	2.47E-05	0.4363	0.1350
1.093814	0.6317	0.00E+00	0	0	1.098431	6.8270	0.00E+00	0	0
1.104036	1.3169	2.11E-05	0.4363	0.1295	1.104146	7.5420	2.48E-05	0.4363	0.1518
1.105026	1.3953	2.06E-05	0.4363	0.1295	1.105026	7.6671	2.47E-05	0.4363	0.1518
1.106125	1.4737	2.19E-05	0.4363	0.1295	1.106015	7.7922	2.47E-05	0.4363	0.1518
1.107334	1.5521	2.33E-05	0.4363	0.1295	1.107114	7.9172	2.45E-05	0.4363	0.1518
1.108433	1.6305	0.00E+00	0	0	1.108104	8.0423	0.00E+00	0	0
1.107554	2.1322	2.28E-05	0.4363	0.1990	1.112061	8.2113	2.47E-05	0.4363	0.2566
1.110082	2.3561	2.31E-05	0.4363	0.1990	1.114809	8.5557	2.47E-05	0.4363	0.2566
1.11228	2.5800	2.29E-05	0.4363	0.1990	1.117007	8.9002	2.46E-05	0.4363	0.2566
1.114039	2.8039	2.21E-05	0.4363	0.1990	1.118656	9.2447	2.46E-05	0.4363	0.2566
1.115358	3.0278	0.00E+00	0	0	1.119645	9.5892	0.00E+00	0	0
1.11272	3.2260	2.30E-05	0.4363	0.1852	1.119315	9.3690	2.21E-05	0.4363	0.2199
1.11327	3.4210	2.31E-05	0.4363	0.1852	1.118766	9.6358	2.94E-05	0.4363	0.2199
1.11338	3.6160	2.34E-05	0.4363	0.1852	1.117557	9.9044	1.92E-05	0.4363	0.2199
1.11316	3.8110	2.30E-05	0.4363	0.1852	1.115688	10.1686	1.64E-05	0.4363	0.2199
1.1125	4.0059	0.00E+00	0	0	1.11349	10.4348	0.00E+00	0	0
1.111841	4.1750	2.46E-05	0.4363	0.1895	1.109313	10.4393	0.00E+00	0	0.1834
1.110632	4.3789	2.49E-05	0.4363	0.1895	1.107224	10.6302	5.47E-06	0.4363	0.1834
1.109313	4.5827	2.40E-05	0.4363	0.1895	1.105026	10.8213	1.03E-06	0.4363	0.1834
1.107994	4.7866	2.50E-05	0.4363	0.1895	1.102717	11.0124	1.00E-06	0.4363	0.1834
1.106675	4.9904	0.00E+00	0	0	1.100409	11.2035	0.00E+00	0	0
1.098101	5.4931	2.47E-05	0.4363	0.1114	1.093484	11.7332	5.27E-07	0.4363	0.1162
1.098431	5.5336	2.48E-05	0.4363	0.1114	1.092495	11.7843	5.27E-07	0.4363	0.1162
1.09887	5.5740	2.48E-05	0.4363	0.1114	1.091506	11.8354	5.27E-07	0.4363	0.1162
1.09942	5.6145	2.48E-05	0.4363	0.1114	1.090626	11.8867	5.27E-07	0.4363	0.1162
1.09986	5.6549	0.00E+00	0	0	1.089857	11.9377	0.00E+00	0	0

As can be seen from Table 1 and 2, the optimized trajectory is close to the original perfect Keplerian orbit. This result is true because the thrusters are only firing to maintain the same orbit; to cancel out the general perturbation included in the equations of motion of the system via the thrust acceleration terms. Figure 1 below shows a plot of

the trajectory initial conditions and the final optimized trajectory values. The Earth is not shown to scale on this

figure.
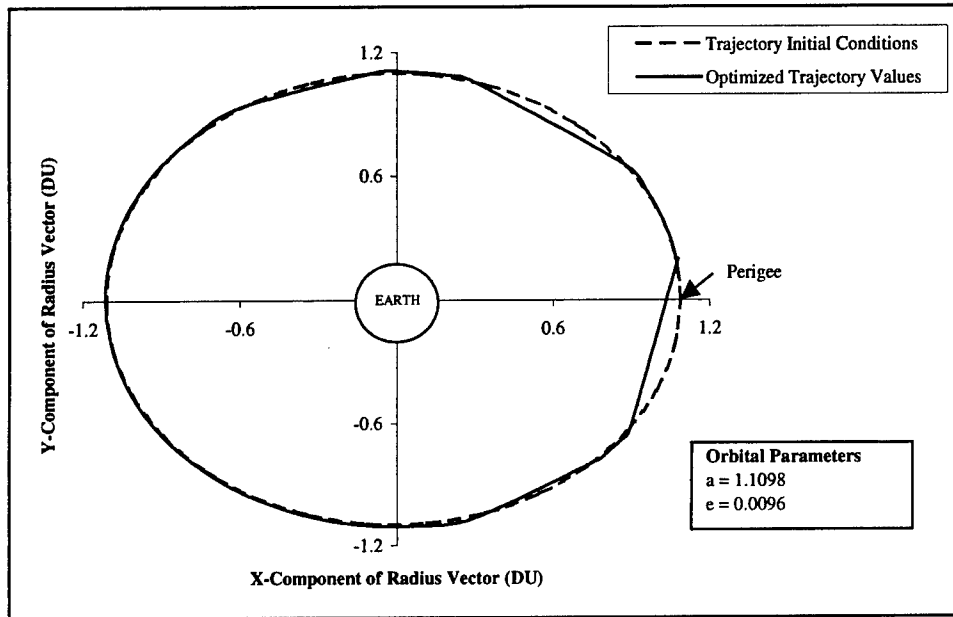
Figure 1: Initial and Optimized Trajectories

The major differences between the initial and the optimized values are the thrust magnitude, the thrust

angle, and the thruster firing time. For the thrust level the optimization code gave values which stayed between 0.1

to 10 milli-Newtons of thrust. At one point in the trajectory it erased a thrust segment to make a longer coast arc.

The thrust angle was changed to a fix value of 0.4363 radians for all thrust segments. This seems odd that the thrust

segments would all require the same thrust angle but no error was found in the coding of the problem. It may have

something to do with the way the optimization subroutine handles the control values; this problem will have to be

looked at in greater detail. The thruster firing time increased from its initial value but this was necessary in order for

the objective function to meet the defect and equality constraints placed on it. After the first run the optimized

trajectory values were placed back into the SQP subroutine to produce new optimized values. The second time

through the routine finished after only one iteration. It gave the exact same solution as is shown in Table 2. This

process was repeated five times in a row and each time yielded the same solution as in Table 2 after one iteration. Such consistency in getting back the same answer implies that this solution is a fairly optimized solution to the problem and it could be used for real mission planning. Next the initial conditions were offset slightly from the original values and it converged to basically the same solution with only the radius and the true anomaly values changing slightly. A really bad guess for the trajectory was attempted but the code couldn't converge to a solution. The SQP may not be robust enough for bad guesses so a more efficient and robust subroutine like NPSOL or MINOS should be used if the there is no good guess for the optimized solution.

Now that the two-dimensional code is working, a three-dimensional code needs to be developed since all real orbits are three-dimensional. Currently the three-dimensional equations of motion and integrals of the motion are developed and only need to be coded into the DCNLP program. Once the three-dimensional code is fully functional perturbations due to atmospheric drag, luni-solar, and the Earth's oblateness effect can be included as well as adding multiple satellites to make a realistic model of the TechSat 21 mission. Numbers returned by a fully developed three-dimensional code with perturbations could be used for actual future mission planning.

Conclusion

An optimal finite-thrust two-dimensional spacecraft trajectory for the TechSat 21 mission was found using the direct collocation with nonlinear programming approach. This approach has proven itself to be quite effective at calculating optimized trajectories. The optimized trajectory was found to be very close to the estimated trajectory, which instills confidence that the solution is a valid one. Future work includes expanding the code to three-dimensions, the inclusion of perturbations caused by atmospheric drag and the Earth's oblateness effects, and the inclusion of multiple satellites flying in formation. The only improvement to be made is to get a more robust and efficient optimization subroutine like NPSOL or MINOS that can handle bad guesses for the initial conditions. This would be a great help in situations where no obvious solution is known and would allow greater flexibility in the choice of initial conditions.

References

[1]   "TechSat 21 Program Overview,' Air Force Research Laboratory/ Space Vehicles Directorate, March 1998.

[2]   Enright, P.J., and Conway, B.A., "Optimal Finite-Thrust Spacecraft Trajectories Using Collocation and Nonlinear Programming," *Journal of Guidance, Control, and Dynamics*, Vol. 14, No. 5, September-October 1991, pp. 981-985.

[3]   Enright, P.J., and Conway, B.A., "Discrete Approximations to Optimal Trajectories Using Direct Transcription and Nonlinear Programming," *Journal of Guidance, Control, and Dynamics*, Vol. 15, No. 4, July-August 1992, pp. 994-1002.

[4]   Battin, R.H., *An Introduction to the Mathematics and Methods of Astrodynamics*, AIAA Education Series, American Institute of Aeronautics and Astronautics, New York, 1987.

[5]   Vallado, D.A., *Fundamentals of Astrodynamics and Applications*, Space Technology Series, McGraw Hill, New York, 1997.

[6]   Pouliot, Michael R., *Sequential Quadratic Programming (SQP) Subroutine*, June 27, 1980.

[7]   Prussing, J.E., and Conway, B.A., *Orbital Mechanics*, Oxford Press, New York, 1993.

[8]   Bate, R.R., Mueller, D.D., and White, J.E., *Fundamentals of Astrodynamics*, Dover Publications, New York, 1971.

STABLE CONTROLLER DESIGN FOR DEPLOYABLE PRECISION
STRUCTURES USING PERTURBATION THEORY

Robert J. Fuentes
Research Assistant
Department of Aerospace Engineering

University of Colorado at Boulder
Campus Box 429
Boulder, CO 80309-0429

Final Report for:
Graduate Student Research Program
Phillips Laboratory Site

Sponsored by:
Air Force Research Laboratory
Kirtland Air Force Base, Albuquerque, NM

September 1998

Stable Controller Design for Deployable Precision Structures Using Perturbation Theory

ROBERT J. FUENTES

MARK J. BALAS

Center for Aerospace Structures
University of Colorado at Boulder,
Boulder, CO 80309-0429

ABSTRACT. Perturbation methods for linear operators are commonly used in the analysis of systems that tend to deviate linearly from a given reference model. The construction of an operator with a first order perturbation is investigated and the resulting eigenvalue series is constructed. It is shown that a simplified perturbation series can be obtained for matrix operators with special structure. The given theory is applied to a reduced order model (ROM) control scenario and an algorithm for computing an $O(\varepsilon^3)$ eigenvalue approximation is described.

INTRODUCTION

Modern modeling of large dimensional physical systems primarily employs matrix methods, often via finite elements or partial differential equations. Due to implementation constraints from a control standpoint, however, an adequate model reduction is needed. Model approximations can be used to design controllers, but compensation for observation spillover may be required for stability. It has been shown in [1] that addition of a residual mode filter to the reduced order model controller can stabilize the entire system in modal coordinates. The question now becomes: What components of the spectrum were destabilized? An eigenvalue perturbation method, developed in [3], has been proposed for full rank operators with no multiplicities. In this paper, we have expanded this technique to consider multiple eigenvalues and also provide proof of the order of approximation.

Applied mathematicians, engineers and physicists frequently use perturbation methods to solve a variety of different problems. Even though solutions to intractable nonlinear differential equations can be approximated using perturbation theory, this paper's focus will only encompass linear deviations of finite-dimensional linear operators. The reader is also referred to an "in-depth" treatment of the perturbation theory of linear operators [4], where the subsequent derivations become special cases.

The following definitions lay the groundwork for the construction of an eigenvalue perturbation series. The type of structure imparted upon a matrix operator of interest is illustrated and the corresponding eigenvalue series is given. An example of the application to the control design of a spectral system is explained. A proof and the numerical algorithm for this approach are given in the appendices.

OPERATOR PERTURBATIONS

Beginning with an operator with a first order perturbation,

$$A(\varepsilon) = A^0 + \varepsilon \Delta A \tag{1}$$

$$A^0 \in \mathrm{R}^{\mathrm{L \times L}} \text{ (diagonalizable, full rank)}$$

$$\varepsilon \in \mathrm{C}, \Delta A \in \mathrm{R}^{\mathrm{L \times L}}$$

the resolvent of $A(\varepsilon)$ is defined by the following inverse:

$$R(\lambda, A(\varepsilon)) \equiv [A(\varepsilon) - \lambda \mathrm{I}]^{-1} \tag{2}$$

and is analytic everywhere except at the eigenvalues of $A(\varepsilon)$. It has been shown in [3] that the resolvent can be written in series form,

$$R(\lambda, A(\varepsilon)) = R(\lambda, A^0) + \sum_{n=1}^{\infty} R^{(n)}(\lambda)\varepsilon^n \tag{3}$$

$$R^{(n)}(\lambda) \equiv R(\lambda, A^0)\left[-\Delta A\, R(\lambda, A^0)\right]^n$$

and the series is convergent if the following inequality holds.

$$0 \le \left\| \Delta A\, R(\lambda, A^0) \right\| |\varepsilon| < 1$$

The spectral factorization of A^0 can be expressed as a sum of S orthogonal eigen-projections, P_l.

$$A^0 = U\overline{\Lambda}U^{-1} = \sum_{k=1}^{L} \overline{\lambda}_k P_k' = \sum_{l=1}^{S} \lambda_l P_l^0 = \sum_{l=1}^{S} \lambda_l\, U E_l U^{-1} \tag{4}$$

$$E_l \equiv \begin{bmatrix} 0 & 0 & . & 0 \\ 0 & I_{m \times m} & . & 0 \\ . & . & . & . \\ 0 & 0 & . & 0 \end{bmatrix}$$

Note that S < N if any of the eigenvalues in $\overline{\Lambda}$ are repeated. The multiplicity of the lth eigenvalue is computed by taking the trace of the lth factor in equation (4).

$$Tr\left[U\, E_l\, U^{-1}\right] = Tr\left[E_l\, U^{-1}U\right] = Tr\left[E_l\right] = m_l$$

Similarly, the resolvent can be written as a sum of projections:

$$R(\lambda, A^0) = \sum_{l=1}^{S} \frac{P_l}{\lambda_l - \lambda} \tag{5}$$

and the reduced resolvent, $S_n(\lambda)$, is defined in equation (6) as the complement of the nth projection.

$$S_n(\lambda) \equiv \sum_{\substack{l=1 \\ l \ne n}}^{S} \frac{P_l}{\lambda_l - \lambda} \tag{6}$$

Each of these eigen-projections can be recovered from the integration of the resolvent around a closed curve in the complex plane.

$$P_l = \frac{-1}{2\pi j} \oint_{\Gamma_l} R(\lambda, A^0)\, d\lambda \tag{7}$$

OPERATOR PARTITIONING

Assume that the linear operator $A(\varepsilon)$ can be partitioned in the following manner:

$$A(\varepsilon) = \begin{bmatrix} A^{1,1} & \varepsilon\,\Delta A^{1,2} \\ \varepsilon\,\Delta A^{2,1} & A^{2,2} \end{bmatrix} = \begin{bmatrix} A^{1,1} & 0 \\ 0 & A^{2,2} \end{bmatrix} + \varepsilon \begin{bmatrix} 0 & \Delta A^{1,2} \\ \Delta A^{2,1} & 0 \end{bmatrix} \qquad (8)$$

$$= A^0 + \varepsilon\,\Delta A$$

$$A^0 \in X_{BD} \quad \text{(Block Diagonal)}$$

$$\Delta A \in X_{OD} \quad \text{(Block Off-Diagonal)}$$

The first factor, A^0, is an element in the space of block diagonal matrices. The perturbing matrix, ΔA, is a member of the complementary block off-diagonal space. In fact, matrix multiplication of these operators can be interpreted as mappings between these spaces.

It is said that A and B are partitioned when A is a complement matrix of B (A and B do not overlap) and $A \in X_{BD}$; $B \in X_{OD}$, then the following definitions hold:

$$(1.)\; A^n \in X_{BD} \quad \forall\, n = 1, 2, \ldots$$

$$(2.)\; B^n \in \begin{cases} X_{BD} & \text{for } n \text{ even} \\ X_{OD} & \text{for } n \text{ odd} \end{cases}$$

$$(3.)\; \left.\begin{matrix} A \cdot B \\ B \cdot A \end{matrix}\right\} \in X_{OD}$$

EIGENVALUE PERTURBATIONS

The kth projection of an operator, $A(\varepsilon)$, can be written as the corresponding eigenvalue scaling that projection.

$$A(\varepsilon)\,P_k(\varepsilon) = P_k(\varepsilon)\,A(\varepsilon) = \lambda_k(\varepsilon)\,P_k(\varepsilon) \qquad (9)$$

$P_k(\varepsilon)$ is determined from integrating the resolvent, $R(\lambda, A(\varepsilon))$, around the kth eigenvalue and results in an infinite series in ε.

$$P_k(\varepsilon) = \frac{-1}{2\pi j}\oint_{\Gamma_k} R(\lambda, A(\varepsilon))\, d\lambda = \frac{-1}{2\pi j}\oint_{\Gamma_k} R(\lambda, A^0)\, d\lambda + \frac{-1}{2\pi j}\varepsilon^n \oint_{\Gamma_k}\sum_{n=1}^{\infty} R^{(n)}(\lambda)\, d\lambda$$

$$= P_k^0 + \sum_{n=1}^{\infty} P_k^{(n)}\varepsilon^n \qquad (10)$$

By taking the trace of equation (9), the kth eigenvalue series is recovered:

$$\lambda_k(\varepsilon) = \frac{1}{m_k} Tr\big[A(\varepsilon)\,P_k(\varepsilon)\big] \qquad (11)$$

$$= \lambda_k^0 + \sum_{n=1}^{\infty} \lambda_k^{(n)}\varepsilon^n$$

where λ^0 represents an eigenvalue of A^0. If $A(\varepsilon)$ is partitioned into the form given in (8), the previous equation is simplified to an even series.

$$\lambda_k(\varepsilon) = \lambda_k^0 + \lambda_k^{(2)} \varepsilon^2 + \lambda_k^{(4)} \varepsilon^4 + \dots = \lambda_k^0 + \sum_{n=1}^{\infty} \lambda_k^{(2n)} \varepsilon^{2n} \qquad (12)$$

Proof of this result is given in Appendix A.

DETERMINATION OF INSTABILITY IN LINEARLY PERTURBED SYSTEMS

At this point, the application of this method to the state space control approach given in [1], [2], and [5] is considered. Given a linear plant governed by the following vector differential equation:

$$\dot{\underline{x}} = A\,\underline{x} + B\,\underline{u}$$
$$\underline{y} = C\,\underline{x} + D\,\underline{u} \qquad (13)$$

$\underline{x} \equiv$ plant state vector
$\underline{u} \equiv$ control input vector
$\underline{y} \equiv$ output observation vector

the objective is to stabilize (13) through the use of M actuator inputs and P sensor outputs. Matrix operators B and C will have the finite rank of M and P, respectively, with the linear differential operator, A, possibly of infinite dimension.

Using the ROM (reduced order model) methodology, it is possible to transform the plant to a modal coordinate system and separate (13) into two state equations. Assuming the feed-through term, D, is zero:

$$\dot{\underline{x}}_N = A_N\,\underline{x}_N + B_N\,\underline{u}$$
$$\underline{y}_N = C_N\,\underline{x}_N \qquad (14a)$$

$$\dot{\underline{x}}_R = A_R\,\underline{x}_R + B_R\,\underline{u}$$
$$\underline{y}_R = C_R\,\underline{x}_R \qquad (14b)$$

$$\underline{y} = \underline{y}_N + \underline{y}_R$$

The preliminary control design of the entire plant is based upon the dynamics of (14a). A finite number of modes are chosen for A_N, which is an operator of rank N. Equation (14b) consists of modes that are not of immediate consideration and are open loop stable. (Re $(\lambda (A_R)) < 0$) The use of state estimation and N state feedback results in the system of equations in (15).

$$\dot{\hat{\underline{x}}}_N = A_N\,\hat{\underline{x}}_N + B_N\,\underline{u} + K_N(\underline{y} - \hat{\underline{y}}_N)$$
$$\hat{\underline{y}}_N = C_N\,\hat{\underline{x}}_N \qquad (15)$$
$$\underline{u} = G_N\,\hat{\underline{x}}_N$$

Defining the error between estimated and actual states by a vector $\underline{e}_N$, the differential equation governing error progression becomes the difference between state equations:

$$\underline{e}_N = \hat{\underline{x}}_N - \underline{x}_N \tag{16}$$

$$\dot{\underline{e}}_N = (A_N - K_N C_N)\,\underline{e}_N + K_N C_R \underline{x}_R$$

If controllability and observability requirements are met for the system, arbitrary decay rates for the designed subsystem can be achieved by choosing the appropriate estimator gain, K_N, and feedback gain, G_N, matrices for the desired eigenvalues of A-KC and A+BG.

Writing equations (14a), (14b), and (16) in matrix form, the probable causes of instability in the closed loop system can be clearly determined.

$$\begin{bmatrix} \dot{\underline{x}}_N \\ \dot{\underline{e}}_N \\ \underline{x}_R \end{bmatrix} = \underbrace{\begin{bmatrix} A_N + B_N G_N & B_N G_N & 0 \\ 0 & A_N - K_N C_N & \mathbf{K_N C_R} \\ \mathbf{B_R G_N} & \mathbf{B_R G_N} & A_R \end{bmatrix}}_{A_c} \cdot \begin{bmatrix} \underline{x}_N \\ \underline{e}_N \\ \underline{x}_R \end{bmatrix} \tag{17}$$

Cross-coupling terms in (17), illustrated in bold, characterize the introduction of estimator feedback which can destabilize the residual state equation. One option to remedy this problem is given in [1], in which a residual mode filter (RMF) is developed to compensate for eigenvalues that are drawn unstable. However, knowledge of those open loop eigenvalues contained in A_R is needed in order to implement the method. Previous work by Gooyabadi [3] offers a limited perturbation solution to this problem.

Partitioning equation (17) according to the method given in section (2), the matrix A_c can be considered to be the sum of a stable, linear operator, A^0, and a perturbing operator, ΔA.

$$A(\varepsilon) \equiv \begin{bmatrix} A_N + B_N G_N & B_N G_N & 0 \\ 0 & A_N - K_N C_N & 0 \\ 0 & 0 & A_R \end{bmatrix} + \varepsilon \begin{bmatrix} 0 & 0 & 0 \\ 0 & 0 & K_N C_R \\ B_R G_N & B_R G_N & 0 \end{bmatrix} \tag{18}$$

$$= A^0 + \varepsilon \, \Delta A$$

Our objective is to find out which eigenvalues of A^0 are driven unstable by ΔA through the computation of the first few non-zero terms of the perturbation series (12). Taking $\varepsilon = 1$ would give equation (17), but convergence of the eigenvalue series solely rests upon the condition that $\|\Delta A\, R(\lambda, A^0)\| < 1$. Therefore, it is possible that (12) is divergent for arbitrary $\|\Delta A\, R(\lambda, A^0)\| \neq 1$ and may have asymptotic convergence.

An example of implementation of this perturbation scheme is given for a simple Euler-Bernoulli beam with pinned ends:

$$m z_{,tt}(x,t) - 2\xi z_{,txx}(x,t) + E \cdot I z_{,xxxx}(x,t) = u(t)\delta(x - 0.1 \cdot l) \tag{19}$$

$$\text{B.C.:} \quad \begin{array}{l} z(0,\,t) = z(l,\,t) = 0 \\ z_{xx}(0,\,t) = z_{xx}(l,\,t) = 0 \end{array}$$

$$y(t) = \int_0^l z(x,t)\delta(x - 0.9 \cdot l)\,dx = z(0.9 \cdot l, t)$$

All of the constants in (19) are normalized with the exception of the damping ratio. ($|\xi| = 5.0\ 10^{-6}$) Actuation of the beam occurs at the point $x = 0.1$. Observations of the beam

displacement, $y(t)$, are taken at $x = 0.9$. Using the method of eigenfunction expansions, a temporal differential equation can be constructed:

$$\ddot{z}_k(t) = -(k\pi)^4 z_k(t) - 2\xi(k\pi)^2 \dot{z}_k(t) + \phi_k(0.1) u(t) \tag{20}$$

The spatial eigenfunctions, ϕ_k, transform the input, $u(t)$, into the modal system of equations given in (20). Control is introduced to dampen the first few modes, where $k = 1, 2,$ and 3. There exist an infinite number of residual modes ($k \geq 4$), but for computational purposes only the next 12 are considered. Putting the equations derived from (13) in the form given in (18), we can calculate an estimate of the residual eigenvalue perturbation resulting from the control design:

$$\lambda_k(\varepsilon)\big|_{\varepsilon=1} \cong \lambda_k^0 + \lambda_k^{(2)} \tag{21}$$

The results of this $O(\varepsilon^3)$ approximation are illustrated below in Figure 1. from this graph, it can be determined that modes $n = 5, 7$ are driven unstable. Using these modes in an RMF control design, exponential stability for the entire system can be achieved.
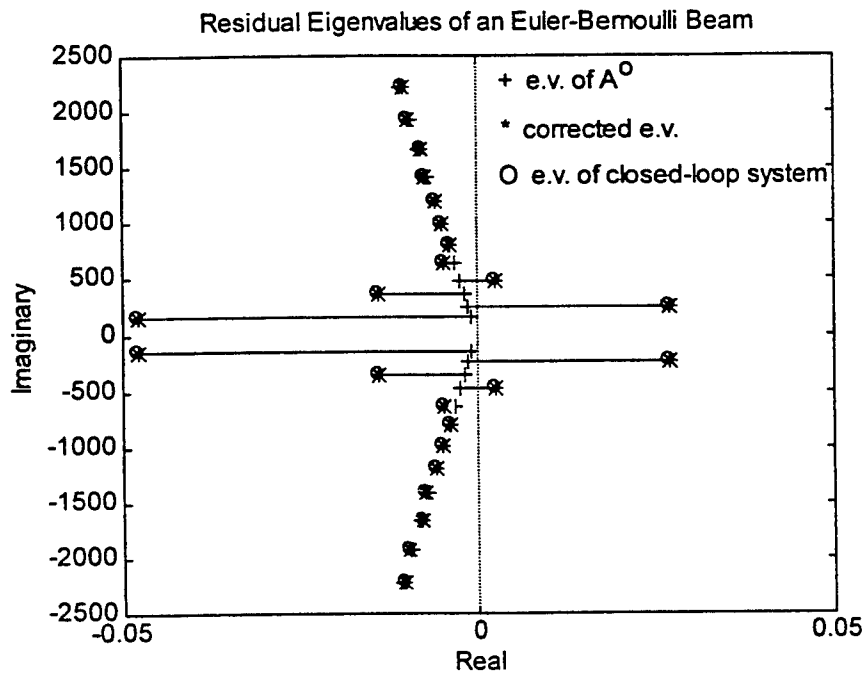

FIGURE 1.

CONCLUSIONS

A generalized approach to the perturbation method outlined in [3] has been developed. Given a block diagonal linear operator with a first order perturbation in partitioned form, it has been shown that there exists a corresponding even perturbation series. An algorithm is outlined to find the $O(\varepsilon^3)$ correction for block diagonal operators

containing eigenvalue multiplicities. Application of this technique to a simple structural model illustrates that this method is a viable approach to ROM control design. This procedure is shown to be successful in other structural problems with no repeated eigenvalues using finite element models [3].

REFERENCES

1. M. Balas, Finite-Dimensional Controllers for Linear Distributed Parameter Systems: Exponential Stability Using Residual Mode Filters, *J. Math. Anal. Appl.*, Vol. 133, No.2, 1988.

2. M. Balas et. al., Low Order Control of Large Aerospace Structures Using Residual Mode Filters, CU-CSSC-88-05, 1988.

3. A. Gooyabadi, Doctoral Thesis, University of Colorado at Boulder, Boulder, CO, 1992.

4. T. Kato, Perturbation Theory for Linear Operators, Springer-Verlag, New York, 1980 Reprint.

5. B. Reisenauer and M. Balas, Master's Thesis, CSI Compensation for Reduced-Order Model Based Control of a Flexible Robot Manipulator, 1990.

APPENDIX A.

Equation (12) is derived from (11) as follows:

Let $A(\varepsilon) = A^0 + \varepsilon \Delta A$, where $A^0 \in X_{BD}$ and $\Delta A \in X_{OD}$.

$$\lambda_k(\varepsilon) = \frac{1}{m_k} Tr[A(\varepsilon) P_k(\varepsilon)] \tag{B1}$$

$$= \frac{1}{m_k} Tr[(A(\varepsilon) - \lambda_k^0 I) P_k(\varepsilon) + \lambda_k^0 P_k(\varepsilon)]$$

$$= \lambda_k^0 + \frac{1}{m_k} Tr[(A(\varepsilon) - \lambda_k^0 I) P_k(\varepsilon)]$$

$$\lambda_k(\varepsilon) - \lambda_k^0 = \frac{1}{m_k} Tr[(A(\varepsilon) - \lambda_k^0 I) P_k(\varepsilon)]$$

Rewriting part of the previous result:

$$(A(\varepsilon) - \lambda_k^0 I) P_k(\varepsilon) = \frac{-1}{2\pi j} \oint_{\Gamma_k} (A(\varepsilon) - \lambda_k^0 I) R(\lambda, A(\varepsilon)) \, d\lambda$$

$$= \frac{-1}{2\pi j} \oint_{\Gamma_k} (A(\varepsilon) - \lambda I + \lambda I - \lambda_k^0 I) R(\lambda, A(\varepsilon)) \, d\lambda$$

$$= \frac{-1}{2\pi j} \left[\oint_{\Gamma_k} (A(\varepsilon) - \lambda I) R(\lambda, A(\varepsilon)) \, d\lambda + \oint_{\Gamma_k} (\lambda - \lambda_k^0) R(\lambda, A(\varepsilon)) \, d\lambda \right] \tag{B2}$$

The first integral in (B2) is analytic since $(A(\varepsilon) - \lambda I) \cdot R(\lambda, A(\varepsilon)) = I$. Therefore:

$$\lambda(\varepsilon) - \lambda_k^0 = \frac{-1}{2\pi j m_k} Tr \left[\oint_{\Gamma_k} (\lambda - \lambda_k^0) R(\lambda, A(\varepsilon)) \, d\lambda \right] \tag{B3}$$

A series form is desired for (B3). Rewriting the kernel of this equation:

$$(\lambda - \lambda_k^0) R(\lambda, A(\varepsilon)) = (\lambda - \lambda_k^0) R(\lambda, A^0) + \sum_{n=1}^{\infty} (\lambda - \lambda_k^0) R^{(n)}(\lambda) \varepsilon^n \tag{B4}$$

Integrating the first term in the right hand side of the equation, we find that this is completely analytic inside Γ_k.

$$\oint_{\Gamma_k} (\lambda - \lambda_k^0) R(\lambda, A^0) \, d\lambda = \oint_{\Gamma_k} (\lambda - \lambda_k^0) \sum_l \frac{P_l^0}{\lambda_l^0 - \lambda} \, d\lambda$$

$$= \oint_{\Gamma_k} (\lambda - \lambda_k^0) \left[\frac{P_k^0}{\lambda_k^0 - \lambda} + S_k^0(\lambda) \right] d\lambda = 0$$

From equation (B4):

$$\lambda(\varepsilon) - \lambda_k^0 = \frac{-1}{2\pi j m_k} Tr \left[\oint_{\Gamma_k} \sum_{n=1}^{\infty} (\lambda - \lambda_k^0) R^{(n)}(\lambda) \varepsilon^n \, d\lambda \right]$$

$$= \frac{-1}{2\pi j m_k} Tr \left[\oint_{\Gamma_k} \sum_{n=1}^{\infty} (-1)^n (\lambda - \lambda_k^0) R(\lambda, A^0) [\Delta A R(\lambda, A^0)]^n \varepsilon^n \, d\lambda \right] \tag{B5}$$

2-9

Using the cyclic permutation property of the trace operator:

$$Tr\left[\frac{d}{d\lambda}\left[\Delta A\, R(\lambda, A^0)\right]^n\right] = n \cdot Tr\left[R(\lambda, A^0)\left[\Delta A\, R(\lambda, A^0)\right]^n\right] \tag{B6}$$

Substitution of (B6) into equation (B5) yields a form that can be integrated by parts:

$$\lambda(\varepsilon) - \lambda_k^0 = \frac{-1}{2\pi j\, m_k} Tr\left[\oint_{\Gamma_k} \sum_{n=1}^{\infty} \frac{(-1)^n}{n}(\lambda - \lambda_k^0)\frac{d}{d\lambda}\left[\Delta A\, R(\lambda, A^0)\right]^n \varepsilon^n\, d\lambda\right]$$

$$= \frac{-1}{2\pi j\, m_k} Tr\left[\oint_{\Gamma_k} \frac{d}{d\lambda}\left[\sum_{n=1}^{\infty}\frac{(-1)^n}{n}(\lambda - \lambda_k^0)\left[\Delta A\, R(\lambda, A^0)\right]^n \varepsilon^n\right] d\lambda - \oint_{\Gamma_k}\sum_{n=1}^{\infty}\frac{(-1)^n}{n}\left[\Delta A\, R(\lambda, A^0)\right]^n \varepsilon^n\, d\lambda\right] \tag{B7}$$

The first term in (B7) can be evaluated about the circle centered at λ^0. Making the substitution: $\lambda = \lambda^0{}_k + r\, e^{jt}$, this integral is zero:

$$\oint_{\Gamma_k}\frac{d}{d\lambda}\left[\sum_{n=1}^{\infty}\frac{(-1)^n}{n}(\lambda - \lambda_k^0)\left[\Delta A\, R(\lambda, A^0)\right]^n \varepsilon^n\right] d\lambda = \sum_{n=1}^{\infty}\frac{(-1)^n\, r\, e^{jt}}{n}\left[\Delta A\, R(\lambda_k^0 + r\, e^{jt}, A^0)\right]^n \varepsilon^n\bigg|_0^{2\pi} = 0$$

The remaining non-zero term in (B7) gives a series in ε. However, the goal is to prove that the odd terms are zero. By equation (10), it is seen that the remainder of (B7) can be rewritten:

$$\lambda_k(\varepsilon) - \lambda_k^0 = \frac{1}{2\pi j\, m_k} Tr\left[\oint_{\Gamma_k}\sum_{n=1}^{\infty}(-\Delta A\, R(\lambda, A^0)) \cdot \frac{(-1)^{n-1}}{n}\left[\Delta A\, R(\lambda, A^0)\right]^{n-1} \varepsilon^n\, d\lambda\right]$$

$$= \frac{1}{m_k} Tr\left[\Delta A \cdot \sum_{n=1}^{\infty}\frac{\varepsilon^n}{n}\left(\frac{-1}{2\pi j}\underbrace{\oint_{\Gamma_k}(-1)^{n-1} R(\lambda, A^0)\left[\Delta A\, R(\lambda, A^0)\right]^{n-1} d\lambda}_{R^{(n-1)}(\lambda)}\right)\right]$$

$$= \frac{1}{m_k} Tr\left[\Delta A \cdot \sum_{n=1}^{\infty}\frac{\varepsilon^n\, P_k^{(n-1)}}{n}\right]$$

For each coefficient, $\lambda^{(n)}$, in this expansion:

$$\lambda_k^{(n)} = \frac{1}{m_k\, n} Tr\left[\Delta A\, P_k^{(n-1)}\right] \tag{B8}$$

Integrating $P^{(n-1)}$ yields an expansion in terms of the reduced resolvent, $S(\lambda_\kappa)$, and the projection, P^0.

$$\lambda_k^{(n)} = \frac{1}{m_k\, n} Tr\left[\sum_{\substack{l_1+\ldots+l_n = n-1 \\ l_i \geq 0}} \Delta A\, S_k^{(l_1)}(\lambda_k)\, \Delta A\, S_k^{(l_2)}(\lambda_k) \ldots \Delta A\, S_k^{(l_n)}(\lambda_k)\right] \tag{B9}$$

where $S^{(0)} \equiv P^0$ and $S^{(i)} \equiv S^i$ for $i \geq 1$.

Writing (B9) in terms of an ordered multiplication:

$$\lambda_k^{(n)} = \frac{1}{m_k n} Tr \left[\sum_{\substack{l_1 + \ldots + l_n = n-1 \\ l_i \geq 0}} \prod_{r=1}^{n} \left[\Delta A \, S_k^{(l_r)}(\lambda_k) \right] \right] \tag{B10}$$

Since $\Delta A \in X_{OD}$ and $S^{(j)} \in X_{BD}$ for all $j \geq 0$ by definition (1) of section (2), then ΔA $S^{(j)} \in X_{OD}$ by definition (3). Therefore, equation (B10) is the sum of a multiplication of n block off-diagonal matrices that are contained in either X_{OD} or X_{BD}, depending on whether n is odd or even. The trace of a block off diagonal matrix is zero, therefore the only non-zero coefficients in (11) are even. Q.E.D.

Assume all of the eigenvalues of the full-rank block diagonal matrix, $A^0 \in R^{L \times L}$, and the corresponding right and left eigenvector matrices, U and U^{-1} can be found. An algorithm for computing the first two non-zero terms in the eigenvalue perturbation series is given below.

1.) Diagonalize A^0, where the eigenvalues in $\overline{\Lambda}^{i,i}$ are ordered $Re(\ \overline{\lambda}^{i,i}_1) \geq Re(\ \overline{\lambda}^{i,i}_2) \geq \dots \geq Re(\ \overline{\lambda}^{i,i}_L)$:

$$A^0 = \begin{bmatrix} A^{1,1} & 0 \\ 0 & A^{2,2} \end{bmatrix} = \begin{bmatrix} U^{1,1} & 0 \\ 0 & U^{2,2} \end{bmatrix} \cdot \begin{bmatrix} \overline{\Lambda}^{1,1} & 0 \\ 0 & \overline{\Lambda}^{2,2} \end{bmatrix} \cdot \begin{bmatrix} (U^{1,1})^{-1} & 0 \\ 0 & (U^{2,2})^{-1} \end{bmatrix}$$

2.) Form the eigen-projections $P^{i,i}_k$ from P'_k for each distinct eigenvalue:

$$A^0 = \begin{bmatrix} \sum_{k=1}^{N1} \overline{\lambda}^{1,1}_k P'_k & 0 \\ 0 & \sum_{k=1}^{N2} \overline{\lambda}^{2,2}_k P'_k \end{bmatrix}$$

N(1) = # of eigenvalues in $\overline{\Lambda}^{1,1}$
N(2) = # of e.v. in $\overline{\Lambda}^{2,2}$.
For $i = 1$ to 2,
    $k = 1$
    $L = N(i)$
    $P' = 0^{L \times L}$
    $P' = Col_1(U^{i,i}) \otimes Row_1((U^{i,i})^{-1})$ **
    $m(k, i) = 1$
    For $j = 2$ to L,
        $P_{temp} = Col_j(U^{i,i}) \otimes Row_j((U^{i,i})^{-1})$
        If $\overline{\lambda}^{i,i}_{j-1} = \overline{\lambda}^{i,i}_j$,
            $P' = P' + P_{temp}$
            $m(k, i) = m(k, i) + 1$
        Else,
            $P^{i,i}_k = P'$
            $\lambda^{i,i}_k = \overline{\lambda}^{i,i}_{j-1}$
            $k = k + 1$
            $m(k, i) = 1$
            $P' = P_{temp}$
        End If
    End
    $P^{i,i}_k = P'$
    $\lambda^{i,i}_k = \overline{\lambda}^{i,i}_L$
    $S(i) = k$
End
** $\otimes$ denotes an outer-product.

3.) Compute reduced resolvents, correcting coefficients, $\lambda^{(2)}{}_k$, and eigenvalue estimates:

For $k = 1$ to S(1),

$$S_k^{2,2} = \sum_{j=1}^{S(2)} \frac{P_j^{2,2}}{\lambda_k^{1,1} - \lambda_j^{2,2}}$$

$$\left(\lambda_k^{1,1}\right)^{(2)} = \frac{1}{m(k,1)} Tr\left[\Delta A^{1,2} S_k^{2,2} \Delta A^{2,1} P_k^{1,1}\right]$$

$$\lambda_k^{1,1}(\varepsilon) = \lambda_k^{1,1} + \left(\lambda_k^{1,1}\right)^{(2)} \varepsilon^2$$

End

For $k = 1$ to S(2),

$$S_k^{1,1} = \sum_{j=1}^{S(1)} \frac{P_j^{1,1}}{\lambda_k^{2,2} - \lambda_j^{1,1}}$$

$$\left(\lambda_k^{2,2}\right)^{(2)} = \frac{1}{m(k,2)} Tr\left[\Delta A^{2,1} S_k^{1,1} \Delta A^{1,2} P_k^{2,2}\right]$$

$$\lambda_k^{2,2}(\varepsilon) = \lambda_k^{2,2} + \left(\lambda_k^{2,2}\right)^{(2)} \varepsilon^2$$

End If

End

2-13

DETERMINATION OF THE RESIDUAL STRESS
PROFILE IN A THIN COMPOSITE PART

Jeff M Ganley
Graduate Research Assistant

University of New Mexico
Department of Civil Engineering
Albuquerque, NM 87131-1351

Final Report for:
Graduate Student Research Program

Sponsored by:
Air Force Office of Scientific Research,
Bolling AFB, Washington D.C.

and

Air Force Research Labs
Kirtland AFB, Albuquerque, NM

August 1998

3-1

DETERMINATION OF THE RESIDUAL STRESS
PROFILE IN A THIN COMPOSITE PART

Jeff M Ganley
Graduate Research Assistant
Department of Civil Engineering
University of New Mexico

Abstract

Composite materials are advantageous for aerospace applications due to their light weight and high stiffness/weight ratio. However, composite parts which are autoclave cured experience problems associated with cure residual stresses, including a reduction in load carrying capacity and 'spring-in', a permanent deformation due to the residual stresses (Stover, 1993). This paper develops an experimental procedure that can be used to obtain the residual stress profile in a thin composite part. This procedure involves progressive cutting of the composite part (i.e. stress relief) and associated strain gage monitoring. The strain gage data is then combined with a finite element analysis to determine the through-thickness residual stress profile in the composite part. This analysis procedure can be used as a tool in the understanding and prediction of spring-in, or simply for measuring the residual stresses in a composite part.

DETERMINATION OF THE RESIDUAL STRESS PROFILE IN A THIN COMPOSITE PART

Jeff M Ganley

Introduction

Composite materials are advantageous for aerospace applications due to their light weight and high stiffness/weight ratio. Many other factors give composites superior performance over traditional materials, including the fact that composite materials can be tailored to meet specific design and loading requirements. However, a significant problem in the composites industry is that autoclave cured composite parts experience problems associated with curing residual stresses, including a reduction in load carrying capacity and spring-in. This paper will present an experimental methodology for determining the residual stress profile in a thin composite part. This methodology was originally developed as a tool to aid in understanding spring-in in thin composite parts. However, the methodology can easily be extended to either thick composite parts or isotropic material applications. In fact, the methodology is applicable, with certain limitations, to any solid where the residual stress profile is desired.

Determination of Residual Stress Profile

The purpose of the methodology developed in this paper is to be able to precisely determine the stress (or strain, given a linear elastic assumption) profile through the thickness of a thin composite part. For most composite materials, including the IM7/977-2 carbon fiber/epoxy material used in the current research, the material response is linear elastic to initial failure. Thus, the linear elastic assumption is typically a good one for stresses below initial failure thresholds. The residual stress profile determination will be accomplished through a methodology that involves a step-by-step cutting of the composite part through the thickness, combined with finite element modeling using IDEAS Master Series 4.0 finite element software (SDRC, 1990). A brief overview of the procedure for finding the residual stress profile through the composite part thickness is given by the following:

1. Mount strain gages to the composite part on the inside and outside faces.

2. Cut the part through the thickness near the strain gage in ten equal steps, stopping after each cut to read the strain gage output. The strain change measured by the gage at each step is due to the relieving of residual stresses at the cut.

3. Model the part in IDEAS, creating finite element models for each of the ten cuts. Place a unit load at each modeled cut and record the associated strains from IDEAS at the real strain gage location.

4. Correlate the IDEAS strains with the actual strain gage strains to obtain the residual stresses in the part at each cut.

20 Layer Part Residual Stress Profile Experiment

The procedure given above was completed for a 20 layer thick, 17.8 N winding tension IM7/977-2 unidirectional hoop composite part. The part had the following dimensions: thickness (radially) = 0.3175 cm, width = 4.064 cm, and original inner radius = 6.585 cm. In preparation for the test, the part was cut longitudinally and allowed to spring-in, then the overlap due to the spring-in was cut out. The part was then mounted with 8 strain gages, mounted 2.54 cm apart center to center, on alternating faces of the part (4 on the inside face and 4 on the outside face). The part was then mounted in a Bridgeport C&C machine and secured (i.e. fixed condition) at 2.54 cm below the first strain gage. The machine was then programmed to cut the part in ten equal steps at the centerline of the first strain gage from inside to outside (the first gage was mounted on the outside face). After each of the ten cuts, the machine was paused for approximately 30 seconds while the output from the strain gage signal conditioner was recorded. When the cutting process at the first gage was completed, the part was rotated to align the cutting blade with the centerline of the second gage and re-clamped, and the cutting process repeated. For each strain gage, the cutting was from the opposite face of the part, toward the gage, at the centerline of the gage. In addition, for each cutting process there was 2.54 cm of free composite part above the cut, and 2.54 cm from the cut location to the fixed condition. This process was repeated for all eight strain gages.

The reason for cutting at the centerline of the strain gage, which will cut through and destroy the gage on the final cut, is that this will give more robust results than mounting the strain gage offset to the cut. As can be seen in Figure 1 on the following page, the FEM strain values due to the cutting and relieving of residual

3-4

stresses in the part are fairly constant over a range approximately equal to the thickness of the part (-5 to 5 in Figure 1). However, the strains quickly drop off as you move away from the center of the cut.
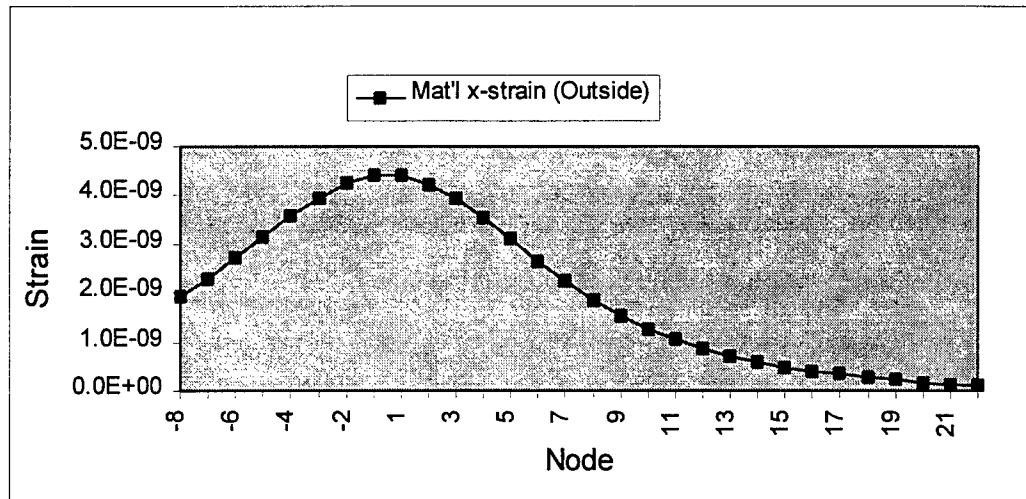

Figure 1 – Strains on the Outer Face of the 20 Layer Part Due to the First Cut
          as a Function of Distance from the Cut

If the strain gage is placed offset to the cut and the strain gage is not precisely located relative to the cut, the actual gage location and the FEM modeled gage location will not be the same, and thus the two will measure differing strains (refer to Figure 1 above). This will lead to error in the prediction of the residual stresses in the part. However, if the strain gage is placed at the centerline of the cut, a slight misplacement of the gage will not effect the results significantly. This is because the strains near the cut centerline are relatively constant and because of the symmetry of the strain values about the centerline of the cut (refer to Figure 1). Thus, a slight misalignment of the strain gage relative to the cut will not significantly change the *average* strain over the length of the strain gage.

In addition to the requirements given above, it is important to consider other factors when performing a residual stress profile test on a thin composite part. First, one must be sure to use a sealed strain gage. If not, the carbon dust that results from the cutting will settle on the face of the strain gage and short the gage, yielding inaccurate strain readings. Second, because of the thin nature of the part and the placement of the strain gage close to the cut, the strain gage and part will experience heating due to the cutting operation. This must be

accounted for during the testing. This was accomplished in this research by selecting a thin diamond cutting blade (i.e. less heat production), and allowing the part and gage to return to room temperature prior to recording the strain gage output.

The results of the 20 layer part residual stress profile test are given in Table 1 below. The values in the first part of the table are from the strain gage signal conditioner and are given in Volts. The second part of Table 1 gives the average values from the eight strain gages in the first part of the table (in Volts, V_o), then converts the average to microstrains ($\mu\varepsilon$) using the following equation:

$$\mu\varepsilon = V_o * 382.7751196 \qquad \text{(Equation 1)}$$

Table 1 – Residual Stress Profile Strain Gage Results (20 Layer Part)

Cut	1st gage / inside-out	2nd gage / outside-in	3rd gage / inside-out	4th gage / outside-in	5th gage / inside-out	6th gage / outside-in	7th gage / inside-out	8th gage / outside-in
No Cut	0.002	0.004	0.002	0.000	0.002	0.000	0.003	0.000
0.03175 cm	-0.403	-0.237	-0.393	-0.217	-0.436	-0.208	-0.504	-0.293
0.06350 cm	-0.942	-0.600	-0.952	-0.614	-0.942	-0.578	-1.060	-0.713
0.09525 cm	-1.416	-1.066	-1.432	-1.093	-1.335	-1.058	-1.520	-1.235
0.12700 cm	-1.660	-1.620	-1.682	-1.669	-1.521	-1.626	-1.756	-1.835
0.15875 cm	-1.746	-2.207	-1.771	-2.270	-1.577	-2.232	-1.816	-2.444
0.19050 cm	-1.727	-2.743	-1.750	-2.825	-1.546	-2.813	-1.770	-2.970
0.22225 cm	-1.680	-3.067	-1.716	-3.160	-1.520	-3.200	-1.690	-3.280
0.25400 cm	-1.667	-3.150	-1.730	-3.270	-1.558	-3.340	-1.616	-3.420
0.28575 cm	-1.916	-3.120	-1.947	-3.420	-2.055	-3.300	-1.819	-3.630
0.31750 cm	2.025	1.080	-0.098	1.411	12.520	-3.930	-2.507	1.500

Cut	Average of 1,3,5 & 7	Average of 2,4,6 & 8	Avg. strain 1,3,5,7 ($\mu\varepsilon$)	Avg. strain 2,4,6,8 ($\mu\varepsilon$)
No Cut	0.0023	0.0010	0	0
0.03175 cm	-0.4340	-0.2388	-166.12	-91.39
0.06350 cm	-0.9740	-0.6263	-372.82	-239.71
0.09525 cm	-1.4258	-1.1130	-545.74	-426.03
0.12700 cm	-1.6548	-1.6875	-633.40	-645.93
0.15875 cm	-1.7275	-2.2883	-661.24	-875.89
0.19050 cm	-1.6983	-2.8378	-650.05	-1086.22
0.22225 cm	-1.6515	-3.1768	-632.15	-1215.98
0.25400 cm	-1.6428	-3.2950	-628.80	-1261.24
0.28575 cm	-1.9343	-3.3675	-740.38	-1289.00
0.31750 cm	-	-	-	-

The values for the average strain given in Table 1 on the previous page will be correlated with the IDEAS FEM analysis in the following section to obtain the residual stress profile in the 20 layer part, the results of which are given in Table 4.

Finite Element Modeling

The results of the cutting and strain gage monitoring summarized in the previous section will now be combined with a finite element modeling (FEM) analysis to obtain the residual stress profile in the 20 layer composite part. The finite element analysis was completed using IDEAS Master Series 4.0 (SDRC, 1990), a commercially available finite element modeling package, running on a Hewelett Packard Apollo Series 700 workstation. The purpose of this analysis is to be able to use the strain gage output from the step-by-step cutting process already completed to obtain a residual stress value at each of the ten cuts. This is accomplished by building a finite element model that is identical to the 20 layer composite part, including accurate dimensions and material properties. Then, unit loads are applied in the finite element model at the cut locations, and the resulting strains at the real strain gage location are recorded (refer to Figure 4). The strain values from IDEAS at the real strain gage location, due to the FEM unit loads, can then be correlated with the known strain gage output to find the residual stresses in the real part. The first two steps of this modeling and analysis procedure are given later to help illustrate the process.

IDEAS 20 Layer Part Model

The finite element model created in IDEAS is meant to replicate the actual part as closely as possible. This model will be used in subsequent sections to obtain the residual stress profile in the real part. The IDEAS finite element model for the 20 layer composite part is as follows:

- Analysis Units = cm / N
- Four Noded Quadrilateral Shell Finite Elements (Plane Stress)
- IM7/977-2 Orthotropic Material Properties (given in the following section)
- Part Inner Radius = 6.585 cm
- Part Thickness = 0.3175 cm

- Part Length = 5.08 cm
- Finite Element Nominal Size = 0.03175 cm × 0.03175 cm square
- 10 finite elements through the part thickness
- Element material x-direction is oriented along the arc (circumferential)

The use of plane stress elements instead of plane strain elements will lead to an error in the FEM results of less than 1% due to the orthotropic nature of the IM7/977-2 material (i.e. $1/(1-v_{xy} \cdot v_{yx})$ = 1.00532 $\cong$ 1.0) (Boresi, 1993). This small of an error is not significant for this analysis. In addition, the error will be consistent throughout the FEM analysis. Thus, because of the ratio method used in the FEM analysis (Equation 2), this will not lead to an error in the FEM/ step-by-step cutting methodology results.

Finite Element Analysis IM7/977-2 Material Properties

The relevant IM7/977-2 orthotropic material properties used in the IDEAS finite element analysis are given below (ICI Fiberite, 1995). The x-direction allowable stresses are given to illustrate that the residual stresses in the part (Table 4) are well below the failure values. As such, the linear elastic assumption is valid for this analysis. The material coordinate axes (x, y, z) are set up in the FEM so that the x-direction is along the fiber (the circumferential or hoop direction), the y-direction is perpendicular to the fiber (the axial direction), and the z-direction is also perpendicular to the fiber (the radial direction).

- Modulus in fiber direction, E_x = 1.72369×10^5 MPa
- Modulus perpendicular to fiber, E_y = E_z = 1.01353×10^4 MPa
- Poisson's ratio, v_{xy} = 0.30
- Poisson's ratio, v_{yz} = v_{xz} = 1.764×10^{-2}
- Shear modulus, G_{xy} = G_{yz} = G_{xz} = 6.27423×10^3 MPa
- Allowable stress in tension, x-direction = 2.81996×10^3 MPa
- Allowable stress in compression, x-direction = 1.61337×10^3 MPa

A picture showing the finite element model of the whole part is given in Figure 2 on the following page. The arrows at the bottom represent the fixed condition of the part along the bottom. The grid is the finite element mesh of the part. The line at the center of the part is used to mark the location of the centerline of the

3-8

cut. This line (i.e. the cut) is approximately 2.54 cm from both the fixed and free end as in the actual 20 layer test part.
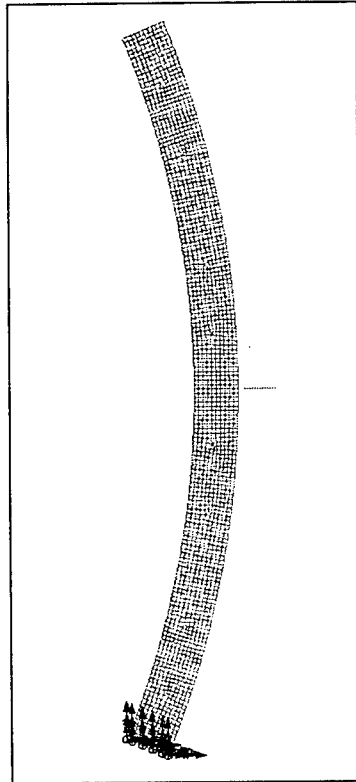

Figure 2 – IDEAS 20 Layer Part Finite Element Model

An enlarged view of Figure 2 is given in Figure 3 on the following page. This shows the finite element mesh near the cut in better detail. In addition, in Figure 3 the first row of elements is removed and unit loads (arrows) are applied to model the first cut.
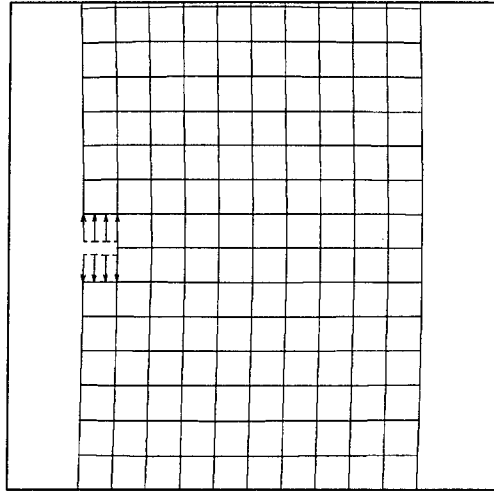
Figure 3 – IDEAS 20 Layer Part Finite Element Model /
Close Up of Cut Region with First Cut Modeled

In Figure 3 above, one column by two rows of elements (i.e. two elements) are removed on the inner face of the model to reflect the first cut of the step-by-step cutting procedure. The removal of one element horizontally reflects material removed in the first cut (element width = 0.03175 cm = 1/10th of the part thickness). In addition, unit loads are applied to the cut faces to model the residual stresses in the real part.

20 Layer Part IDEAS FEM Analysis

The step by step procedure used to correlate the strain readings from the cutting procedure and the finite element analysis is given below. This procedure is best explained by example. Therefore, the first two steps of the actual analysis for the 20 layer part are given below, followed by the general procedure and equations that govern the rest of the analysis.

After accurately modeling the 20 layer part in IDEAS, the first step is to model the first cut by removing elements from the mesh and applying unit loads to the faces of the cut. This is shown in Figure 3 above. This model is then run through the IDEAS post processing software to obtain the strains in the material-x (circumferential) direction. The results of this analysis are shown in Figure 4 on the following page.
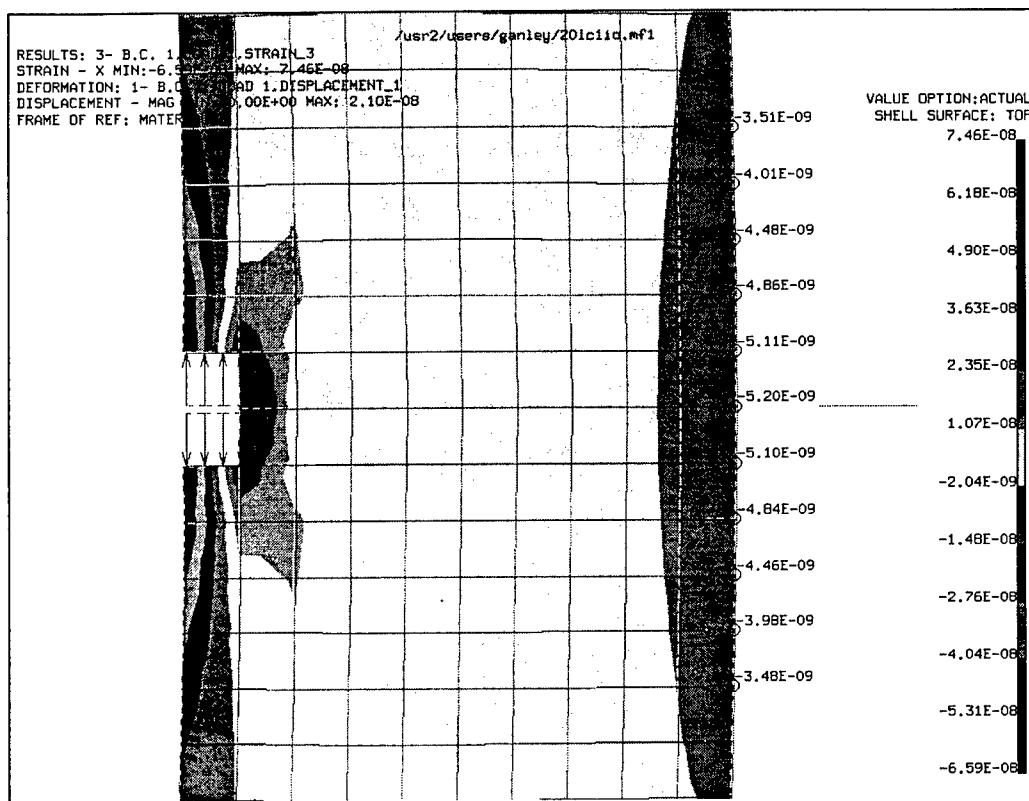
Figure 4 – IDEAS Model of 20 Layer Part / First Cut with Unit Loading

The FEM strain values due to the unit load applied at the cut are given at the location of the real strain gage on the outside of the part (i.e. opposite the cut) in Figure 4 above. In addition to this, the real strain gage output obtained from the C&C cutting experiment is given in Table 1. We can use these two strain values (FEM and real) to obtain the actual forces (residual stresses) that were relieved in the real part due to the first cut. Because of the similarity of the FEM and the real part, the unit loads and the residual stresses are related in the same proportion as the FEM strain and the real strain gage strain. This leads to the following equation:

$$x_1 = \varepsilon_{SG}^{\ 1} / \varepsilon_1^{\ 11} \qquad \text{(Equation 2)}$$

Where:

x_1 = residual stress in the part at the 1st cut (the desired quantity)

$\varepsilon_{SG}^{\ 1}$ = total strain from the real strain gage recorded after the 1st cut

$\varepsilon_1^{\ 11}$ = IDEAS strain due to the 1st load (unit load) applied at the 1st cut

3-11

The value for $\varepsilon_{SG}{}^1 = -166.12 \times 10^{-6}$ is given in Table 1. The value for $\varepsilon_I{}^{11} = -4.520 \times 10^{-9}$ is obtained by taking a simple mathematical average of the strain values in Figure 4. The fact that both of these values are negative indicates that they are compressive strains. Positive values would indicate tensile strains. The IDEAS strain values from Figure 4 are summarized in Table 2 below to illustrate how we obtain $\varepsilon_I{}^{11}$.

Table 2 – IDEAS FEM Analysis Data / Cut 1 (20 Layer Part)

First Cut		Load 1
		20lc1io.mf1
	Nodes Right	Mat'l-x Strain
	0	-5.20E-09
	1	-5.10E-09
	2	-4.85E-09
	3	-4.47E-09
	4	-4.00E-09
	5	-3.50E-09
	Avg. =	-4.520E-09
	-1.661E-04	= Real Gage Avg. Strain
	$x_1 =$	253.4044 MPa

The $x_1 = 253.4044$ MPa value given in Table 2 above was computed by plugging the appropriate values into Equation 2. The x_1 value represents the uniform residual stress that was relieved in the part on the faces of the first cut, due to the first cut. Because the unit load in IDEAS is acting toward the cut faces (refer to Figure 4), which represents the relieved residual stress, the original residual stress in the part (x_1) is tensile. Thus, a positive x_i value indicates a tensile residual stress in the part, and conversely, a negative x_i value indicates a compressive residual stress.

We now have the average residual stress in the part for the first 1/10th of the part thickness (x_1). It is important to note that this analysis procedure gives the average (i.e. uniform) stress value over the cut interval. We assume this constant value when we apply a constant unit load to the cuts in the FEM model. The actual profile is probably not constant. However, the true profile should be able to be modeled accurately if the cuts
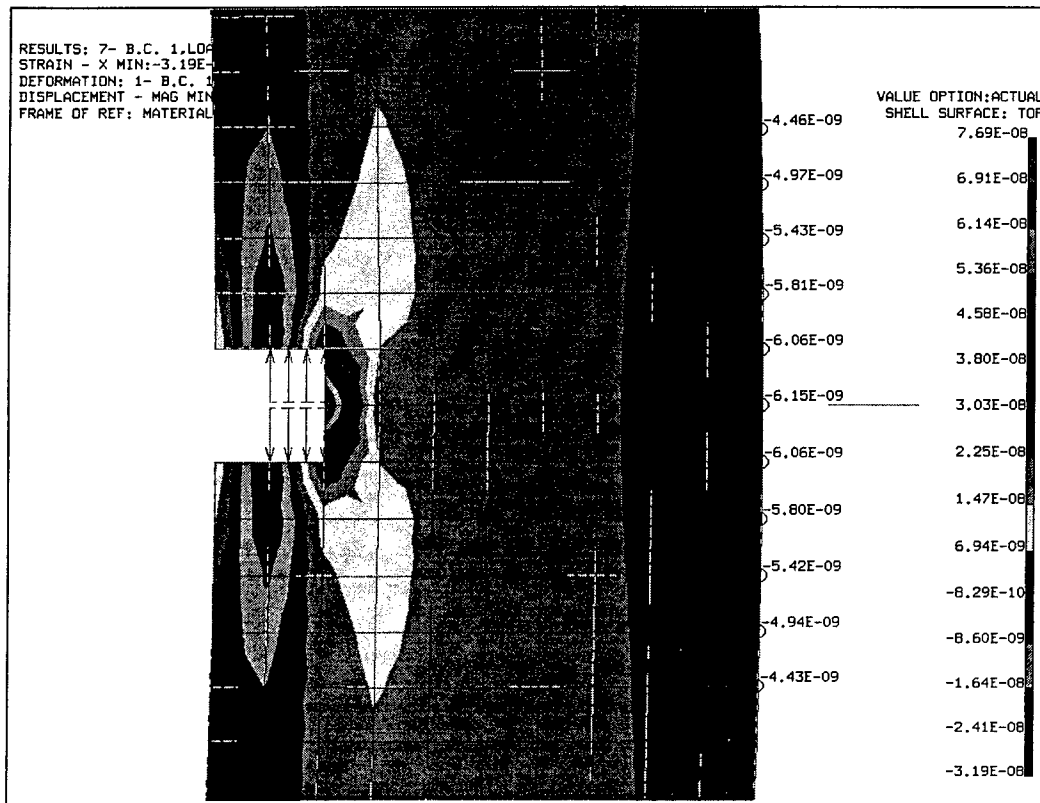
3-12

are small enough. This is similar to a piecewise linear approximation; the accuracy is improved as the interval is decreased.

The next step in the analysis is to obtain the residual stress value (x_2) for the second cut. To accomplish this, the second column of elements is removed in the FEM to model the second cut. Next, two sets of loading conditions are applied separately to the FEM. The first loading condition involves applying unit loads to the face of the elements of cut 1. These unit loads reflect the x_1 forces (relieved residual stresses) that are acting on the part. This is shown in Figure 5 below.

Figure 5 – IDEAS Model of 20 Layer Part / Second Cut with First Load

In addition, the model is loaded with unit loads on the second cut face. These loads represent the additional residual stress (x_2) that is relieved during the second cut. The results of this analysis are given in Figure 6 on the following page.

Figure 6 – IDEAS Model of 20 Layer Part / Second Cut with Second Load

The IDEAS FEM analysis was broken up into two steps for the second cut. This is due to the fact that, after second cutting, the loads acting on the part will be due to the residual stresses obtained in step 1 (i.e. x_1), plus loads due to the additional residual stresses relieved in cut 2. The total contribution of these residual stresses (or loads) to the strain gage location strains must be accounted for separately in the IDEAS analysis. The equation that results for the second cut is as follows:

$$x_2 = (\varepsilon_{SG}^2 - \varepsilon_I^{21} \cdot x_1) / \varepsilon_I^{22} \qquad \text{(Equation 3)}$$

Where:

x_2 = residual stress in the part at the 2nd cut (the desired quantity)

x_1 = residual stress in the part at the 1st cut (from step 1)

ε_{SG}^2 = total strain from the real strain gage recorded after the 2nd cut

ε_I^{21} = IDEAS strain due to the 1st unit load applied after the 2nd cut

ε_I^{22} = IDEAS strain due to the 2nd unit load applied after the 2nd cut

3-14

The value for $\varepsilon_{SG}^2 = -372.82 \times 10^{-6}$ is given in Table 1. The values for $\varepsilon_I^{21} = -1.094 \times 10^{-8}$ and $\varepsilon_I^{22} = -5.473 \times 10^{-9}$ are obtained in the same manner as in step 1 by taking a simple mathematical average of the strain values in Figure 5 and Figure 6 respectively. The IDEAS strain values and result for x_2 are summarized in Table 3 below.

Table 3 – IDEAS FEM Analysis Data / Cut 2 (20 Layer Part)

Second Cut		Load 1	Load 2
		20lc1io.mf1	20lc1io.mf1
	Nodes Right	Mat'l-x Strain	Mat'l-x Strain
	0	-1.24E-08	-6.15E-09
	1	-1.22E-08	-6.06E-09
	2	-1.16E-08	-5.80E-09
	3	-1.08E-08	-5.43E-09
	4	-9.87E-09	-4.96E-09
	5	-8.79E-09	-4.44E-09
	Avg. =	-1.094E-08	-5.473E-09
	-3.728E-04	= Real Gage Average Strain	
	x_2 =	-37.0092 MPa	

The above analysis illustrates the first two steps of the methodology that was developed to find the residual stresses in the 20 layer test part. The following is the general equation that can be used in the analysis procedure:

$$x_i = (\varepsilon_{SG}^i - \varepsilon_I^{i1} \cdot x_1 - \varepsilon_I^{i2} \cdot x_2 - \varepsilon_I^{i3} \cdot x_3 - \ldots - \varepsilon_I^{i(i-1)} \cdot x_{(i-1)}) / \varepsilon_I^{ii} \qquad \text{(Equation 4)}$$

Where:

x_i = residual stress in the part at the i'th cut (the desired quantity)

ε_{SG}^i = total strain from the real strain gage recorded after the i'th cut

ε_I^{ij} = IDEAS strain due to the j'th unit load applied after the i'th cut

In Equation 4 above, the load (j) is always numbered starting from 1 at the cut face of the part to (i) at cut number (i). The analysis proceeds step by step through the piece, using the previous (x_i) values to obtain the next. For this reason, the experimental error will accumulate as one proceeds through the part. This points out a

3-15

balance that must be used in the analysis procedure. More cuts (i.e. steps in the analysis procedure) will lead to a greater accumulated error. However, fewer cuts will take away from the desired resolution in the residual stress profile. These two conflicting influences were taken into account and an analysis procedure was developed to minimize the accumulated experimental error in the results while maximizing the resolution of the residual stress profile. This procedure is given by the following: The methodology of Equation 4 is used to determine the residual stress values (x_i's) in the 20 layer test part for the first five cuts from the outside-in. This process is then repeated for the first five cuts from the inside-out. When combined, this will give the complete residual stress profile through the thickness of the 20 layer part while minimizing the error in the results and maximizing the resolution of the residual stress profile.

This combined methodology was also used, instead of analyzing the part through the full thickness from inside to outside, because of the reduction in finite element modeling required. For each cut (n) added to the process, (n) additional FEM loading conditions must be analyzed. The results of the IDEAS residual stress profile analysis for the 20 layer part are presented in the following section.

IDEAS FEM Results (20 Layer Part)

The results of the IDEAS finite element modeling procedure for the 20 layer part are given in Table 4 below. The table reflects the residual stresses (x_i) at each cut labeled as 1 to 10 from the inside to the outside of the part. As was mentioned previously, a positive x_i value indicates a tensile residual stress in the part, and conversely, a negative x_i value indicates a compressive residual stress.

Table 4 – Residual Stress Profile From IDEAS Analysis (20 Layer Part)

INSIDE	
1	253.4044 MPa
2	-37.0092 MPa
3	-61.6092 MPa
4	-148.8423 MPa
5	-89.5525 MPa
6	-80.1752 MPa
7	-40.4260 MPa
8	10.2471 MPa
9	20.8638 MPa
10	136.9772 MPa
OUTSIDE	

IDEAS FEM Results Validation (20 Layer Part)

The values for the residual stresses in Table 4 above need to be checked to ensure their accuracy. To do this, we note that the residual stress profile of our 20 layer part should have no net force ($\Sigma F=0$) or net moment ($\Sigma M=0$) through the part thickness. This is due to the fact that the composite part has been cut and has sprung-in; and as such it cannot sustain a net moment or force. Thus, we can check the accuracy of the residual stress profile results in Table 4 by determining the sum of forces (ΣF) and sum of moments (ΣM) of the stress profile. If these sums are close to zero, we can assume that the profile of Table 4 is accurate. The results of this analysis, along with the relative error from zero, are given in Table 5 below.

Table 5 – Residual Stress Profile ΣF and ΣM (20 Layer Part)

	Residual Stress (MPa)		Arm from Center-line (cm)		Moment = Stress×Arm (KN/m)	
INSIDE	253.4044		0.142875		362.0515	
	-37.0092		0.111125		-41.1265	
	-61.6092		0.079375		-48.9023	
	-148.8423		0.047625		-70.8861	
	-89.5525		0.015875		-14.2165	
	-80.1752		-0.015875		12.7278	
	-40.4260		-0.047625		19.2529	
	10.2471		-0.079375		-8.1336	
	20.8638		-0.111125		-23.1849	
OUTSIDE	136.9772		-0.142875		-195.7062	
$\Sigma F =$	-36.1219	MPa		$\Sigma M =$	-8.1239	KN/m
$\Sigma F / \Sigma|F| =$	-4.11	%		$\Sigma M / \Sigma|M| =$	-1.02	%

3-17

As can be seen in the last row of Table 5, the error in the ΣF and ΣM calculations is relatively small. In addition, the more critical measure for our analysis, the ΣM error, is only 1%. This suggests that the step by step cutting/FEM analysis for the 20 layer part has yielded accurate results for the residual stress profile (Table 4).

Conclusion

This paper has outlined a step by step cutting / finite element analysis procedure that can be used to determine the residual stress profile in a thin composite part. This procedure was originally developed to assist in determining the spring-in in thin composite parts. However, this procedure can easily be expanded to include thick composite parts or isotropic materials.

References

- Boresi, A.P., Schmidt, R.J., Sidebottom, O.M., *Advanced Mechanics of Materials, 5th ed.*, John Wiley & Sons, Inc., New York, NY, 1993.

- ICI Fiberite Data Sheet, 977-2 Toughened Epoxy Resin, "Typical Properties of Fiberite 977-2 Composite Laminates," November 15, 1995 (Rev. E).

- Stover, Debbie, "Coping with Spring-In in Composite Tools and Parts," *Advanced Composites*, March/April 1993, pp. 38-45.

- Structural Dynamics Research Corporation (SDRC), I-DEAS Master Series 4.0, ©1990.

A STUDY OF THE EFFECTS OF NOVAE ON

THE INFRARED CELESTIAL BACKGROUND

David A. Joiner

Research Assistant

Department of Physics, Applied Physics, and Astronomy

Rensselaer Polytechnic Institute

Troy, NY 12180

A STUDY OF THE EFFECTS OF NOVAE ON

THE INFRARED CELESTIAL BACKGROUND

David A. Joiner

Research Assistant

Department of Physics, Applied Physics, and Astronomy

Abstract

The low densities and short timescales involved with dust grain formation in nova outflows imply that the grain size distribution of dust which forms does not conform with thermodynamic equilibrium, and grain growth in these environments should be modeled in terms of kinetic equations (Johnson et. al. 1993). One recent use of kinetic equations to model dust growth in stellar outflows is presented in Egan and Leung (1995.) We present corrections to the equations for kinetic growth presented in Egan and Leung (1995), and compare the method of contracting a large set of kinetic equations by taking moments of the kinetic equation to a method of binning equations.

To determine the effect of novae on the infrared background, and particularly data from the MSX mission, we first calculate the expected rate of nova observations present in the MSX catalog. We find that the expected number of classical novae for any given map in band A ($8.28\,\mu m$) is of the order of 10, and on the order of 1 in all other bands. We compare 1 known observation in the visual which brightened shortly before MSX measurements of it's location. We report a band A measurement of .322 Jy for Nova V4361 Sgr (Sgr 1996), and discuss the implications of this measurement relative to visual measurements published on this nova.

Introduction

Long ago when curious minds looked at the sky and saw a light appear where before there had been only emptiness, they thought they were witnessing the birth of a new star. They even gave it the name "nova stella", or "new star" (Bode and Evans, 1987). The phenomenon of the nova is now known to be part of a broad class of stars known as cataclysmic variables, in which large changes in brightness occur in very brief time periods. In the classical nova, matter accretes from a binary companion onto the surface of a white dwarf star. The heating of this material by the white dwarf erupts in a thermonuclear runaway, launching a shell of hydrogen, carbon, and other elements at $\sim 1000 \, km \, s^{-1}$, and the star is observed to brighten by many magnitudes in the infrared, visible, and ultraviolet ($\gtrsim 9$ magnitudes in the visible spectrum.) Peak luminosities in the visible can range from $10^4 - 10^6 L_\odot$ for classical novae, with anywhere from a few thousandths to all of the total luminosity reradiated in the infrared (Starrfield 1988).

Over the course of the nova's evolution, great changes can be seen in the infrared, visible, ultraviolet, and x-ray regions of the spectrum. The only major difference between visible light curves is the possible occurrence of a deep dip in the visible light curve during the decline period, associated with an increase in the infrared. Both changes are on the order of a few magnitudes. The current accepted explanation for this dip is that it is caused by the formation of dust in the nova outflow.

The nova event generally lasts for ~ 100 days, and the infrared excess associated with dust formation generally takes place over a few days or weeks. Approximately 100 novae occur in the galaxy every year, of which about 20% have an apparent visible magnitude above 6.0. While the infrared signature during the initial expansion is due only to the expanding shell of gas, the infrared signature of the dust formation event is dominated by the absorption and radiation of carbonaceous or silicate material in the dust shell. In order to understand the spectral signature of the dust formation period in classical novae, the growth of these grains must then be modeled, and the radiative transfer of light through this dusty shell determined from the dust characteristics.

Solving the kinetic equations which describe the growth of dust grains has primarily one obstacle. A $1 \, \mu m$ sized grain requires 10^{12} equations. Researchers generally reduce this set of equations by one of two methods, taking moments of the equations, or grouping equations into bins.

As part of this study I have also estimated the number of novae present in the MSX satellite data is estimated. Visual observations of the slow nova V4361 Sgr are interpreted with respect to an infrared observation ($8.28 \, \mu m$)from the MSX point source catalog. The density of the shell on July 19, 1996, is calculated to be $\sim 10^{10} \, cm^{-3}$.

Modeling Grain formation

Modeling the kinetics involved in grain formation require the solution of a large set of nonlinear ordinary differential equations. The general approach is to in some way contract the large numbers of equations required to a number which is within one's computational means, and integrate using a method suitable for stiff sets of equations, such as the backwards Euler method (Press et. al. 1992) or the Gear method (Kahaner et. al. 1989).

Improvement of computer code from Egan and Leung.

Egan and Leung (1995) cite the following equations for the kinetic growth of grains, determined via a method of taking moments of the kinetic equations, coupled to a truncated set of equations up to some cutoff:

$$\frac{df_i}{dt} = \sum_{j=1}^{M} f_j[-P_{i,i+j}f_i - P_{i,i-j}f_i + P_{i+j,i}f_{i+j} + P_{i-j,i}f_{i-j}] \qquad i > M$$

$$\frac{df_i}{dt} = \sum_{j=1+i}^{N} f_i l[-P_{j-i,j}f_{j-i} + P_{j,j-i}f_j] \qquad\qquad i \leq M$$
$$+\sum_{m=1}^{i-1} f_m[P_{i-m,i}f_{i-m} - P_{i,i-m}f_i + P_{i+m,i}f_{i+m} - P_{i,i+m}f_i]$$
$$-\frac{dK_3}{dt}\Big|_i$$

$$K_i = \sum_{j=N_c}^{\infty} j^{i/3}f_j$$

where $P_{i,i+j}$ is the reaction rate for the kinetic equation $C_j + C_i \rightarrow C_{j+i}$, f_j is the density of the C_j gas component, and only growth by accretion of clusters up to size M is considered. l is a factor which takes into account the difference in the rate for the collision between two clusters of the same size, and as it is written in the equations above is given by $l = (1 + \delta_{2i,j})$. $\frac{dK_3}{dt}\big|_i$ is the interaction of grains above the cutoff grain size N_c with the ith grain size. In the formalism presented by Egan and Leung for determining $\frac{dK_3}{dt}$, each i term is linearly independent, and the determination of $\frac{dK_3}{dt}\big|_i$ from $\frac{dK_3}{dt}$ is trivial.

This expression for the accretable species neglects reactions of the type $C_i + C_m \rightleftharpoons C_{i+m}$, and also has double counting for reactions with grains larger than N_c. If the total shell mass is given by $M = V\sum_{i=1}^{\infty} m_i f_i$, and assuming that the volume V is constant, and the mass of the ith grain size is $m_i = im_c$, then conservation of mass requires that

$$\frac{d}{dt}\sum_{i=1}^{\infty} if_i = \frac{d}{dt}\left[\sum_{i=1}^{N_c-1} if_i + \sum_{i=N_c}^{\infty} if_i \right] = \sum_{i=1}^{N_c-1} i\dot{f_i} + \dot{K_3} = 0$$

Taking these factors into consideration, the improved set of kinetic equations is given by

$$\frac{df_i}{dt} = \sum_{j=1}^{M} f_j[-P_{i,i+j}f_i - P_{i,i-j}f_i + P_{i+j,i}f_{i+j} + P_{i-j,i}f_{i-j}] \qquad i > M$$

$$\frac{df_i}{dt} = \sum_{j=1+i}^{N_c-1} f_i[-P_{j-i,i}f_{j-i} + P_{j,j-i}f_j] \qquad\qquad i \leq M$$

$$+\sum_{m=1}^{i-1} f_m[P_{i-m,i}f_{i-m} - P_{i,i-m}f_i + P_{i+m,i}f_{i+m} - P_{i,i+m}f_i]$$

$$+\sum_{m=1}^{i-1} f_m[P_{i+m,i}f_{i+m} - P_{i,i+m}f_i]$$

$$+\frac{1}{i}\sum_{j=N_c-i}^{N_c-1}(j-i)f_i[-P_{j+i,i}f_{j+i} + P_{j,j+i}f_j]$$

$$-\frac{dK_3}{dt}|_i$$

$$K_i = \sum_{j=N_c}^{\infty} j^{i/3} f_j$$

These alterations were made in Egan's time dependant grain growth code, and are currently being tested.

Comparison of bin and moment method

As was described in the previous section, the kinetic growth of dust grains by accretion of small clusters has been done primarily by two methods. This was originally attempted by Yamamoto and Nishida (1977), but they did not use any method to contract their system of equations, and their grain size was limited to the number of equations they could solve practically, which with the computing resources at that time was ~ 100 equations. Gail and Sedlmayr (1988) introduced a closed set of moments of the kinetic equations. Egan and Leung (1995) applied this method to the growth of dust grains in the outflows of Asymptotic Giant Branch stars.

A second approach was taken by Johnson, Friedlander, and Katz (1993), in which the equations are grouped into bins when the grain size becomes large.

For the purposes of this comparison, growth by accretion of monomers only will be considered for simplicity.

Consider the following model

$$E_i = (1 - 0.5\delta_{i-1,1})4\pi(r_{i-1} + a_0)^2\left[\frac{P_s}{(2\pi m_c k T_{grain})^{1/2}}\right]$$

$$\times \exp\left(\frac{4\pi a_0^2 \sigma_s}{kT_{grain}}\{i^{2/3} - (i-1)^{2/3}\}\right)\frac{N_0}{V}$$

$$C_i = (1 - 0.5\delta_{i,1})\pi(r_i + a_0)^2\left(\frac{8kT_{gas}}{\pi m_c}\right)^{1/2}$$

where C_i is $P_{i,i+1}$ and E_i is $P_{i,i-1}f_1$ in our previous notation. $\frac{N_0}{V}$ is a normalization factor allowing us to write the equation in terms of total numbers instead of densities. This gives us the following master equations to be solved

$$\frac{dN_i}{dt} = N_1[-C_iN_i + C_{i-1}N_{i-1}] \qquad i > 1$$

$$+[-E_iN_i + E_{i+1}N_{i+1}]$$

$$\frac{dN_1}{dt} = -\sum_{j=2}^{\infty} i\frac{dN_i}{dt} \qquad\qquad i = 1$$

Moments can be taken of this set of equations to reduce the number of equations needed to be solved. For

the above definitions, if $i > N_c$ then $N_i \approx N_{i+1}$,

$$\frac{dN_i}{dt} = N_1[-C_iN_i + C_{i-1}N_{i-1}] + [-E_iN_i + E_{i+1}N_{i+1}] \qquad i > 1$$
$$+[-E_iN_i + E_{i+1}N_{i+1}]$$

$$\frac{dN_1}{dt} = -\sum_{j=2}^{N_c-1} i \, \dot{N_j} \, -\dot{K_3}$$

$$\frac{dK_0}{dt} = C_{N_c-1}N_{N_c-1}N_{N_c} - E_{N_c}N_c$$

$$\frac{dK_i}{dt} = N_c^{i/3}[C_{N_c-1}N_{N_c-1}N_{N_c} - E_{N_c}N_c] \qquad i > 0$$
$$+\frac{i}{3}\left[4\pi a_0^2 \left(\frac{kT_{gas}}{2\pi m_c}\right)^{1/2} \frac{N_0}{V}N_1 + 4\pi a_0^2 \frac{P_s}{(2\pi m_c kT_{grain})^{1/2}} \right]K_{i-1}$$

Alternatively, if the master equations are expressed in binned form with i grain sizes g_i, then the rate of growth from bin i to bin $i + 1$ is given by the rate of accretion of $(g_{i+1} - g_i)$ monomers assuming that the rates are essentially unchanged until growth to the next bin has occurred. The binned equations can be written as

$$\frac{dN_i}{dt} = N_1\left[-\frac{C_iN_i}{g_{i+1}-g_i} + \frac{C_{i-1}N_{i-1}}{g_i-g_{i-1}} \right] \qquad i > 1$$
$$+\left[-\frac{E_iN_i}{g_i-g_{i-1}} + \frac{E_{i-1}N_{i+1}}{g_{i+1}-g_i} \right]$$

$$\frac{dN_1}{dt} = -\sum_{j=2}^{\infty} g_i \frac{dN_i}{dt} \qquad i = 1$$

The above problem is solved using each method. Since the moment method does not explicitly give us the grain size distribution, moments are taken of the grain size distribution from the bin method, and these are compared.

The parameters for the comparison models are given in table 1.

$n_{gas}(r = r_*)$	$2.893 \times 10^6 \, \mathrm{cm}^{-3}$
L_*	$10^4 L_\odot$
T_*	$2500\,\mathrm{K}$
$T_{gas} = T_{grain}$	$T_*(R_*/R)^{1/2}$
V_{out}	10^6

Table 1.

Values typical of an AGB star are used for comparison with the work by Egan and Leung. All integrations were performed using Kahaner and Sutherland's DDRIV2 subroutine, in Fortran77, on a Dec Alpha with a 225 MHz processor (Kahaner et. al. 1989). The time and memory requirements of each method depend primarily on the total number of equations required in the solution.

Results for each method agreed qualitatively, and Figure 1 shows grain size as a function of radius from the

4-6

central source.

The major approximation that is made in the derivation of the moment equations is the assumption that for large i, $N_i \approx N_{i-1}$. As N_c is increased, this approximation should improve, and the integration result should approach the exact solution.

In the bin method, the approximation is that a discrete set of grain sizes is treated as a set of bins above some cutoff N_b. The grid spacing after that is arbitrary, but we have chosen a logarithmic bin spacing. The solution should approach the exact solution as the bin widths decrease. There are then two parameters which can be changed to improve the accuracy of the results: the value of the cutoff at which binning begins, and the logarithmic spacing factor χ.
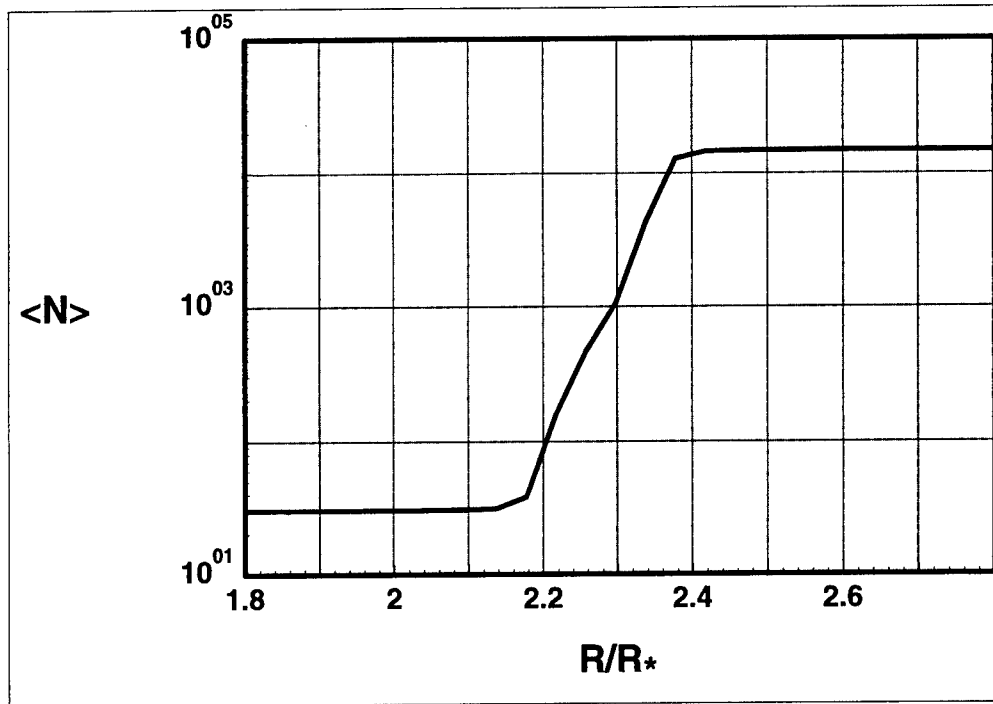
Figure 1. Grain size as a function of radius for the bin method with $N_b = 90, 75$ logarithmically spaced equations, and a maximum possible grain size of 10^8.

Figure 2 shows the maximum grain size from each model, plotted against the total number of equations required in the solution for 4 cases. Case 1 is the moment method. Case 2 is the bin method, with the cutoff value N_b held constant. Cases 3 and 4 show how the solution changes with N_b if the logarithmic spacing factor χ is held constant. The total number of equations required in the moment method depends on the number of extra kinetic equations above N_c used, and on the number of moments solved for. For these models, $N_{moment} = N_c + 7$. In the bin method, the number of equations beyond N_b is determined by χ, and is set so that the size of grains in the last bin is 10^8 carbon atoms.

All methods show an increase in grain size with an increase in the accuracy of the equations. The bin method seems to be leveling off at a smaller number of equations. It is not yet clear exactly if the moment method will converge to the same solution, and this will require further calculations to determine. If we assume that all models are approaching the same value, which due to the monotonic increase in each curve must be greater than the values plotted, then it appears that the bin method is capable of achieving greater accuracy for the same number of equations used.
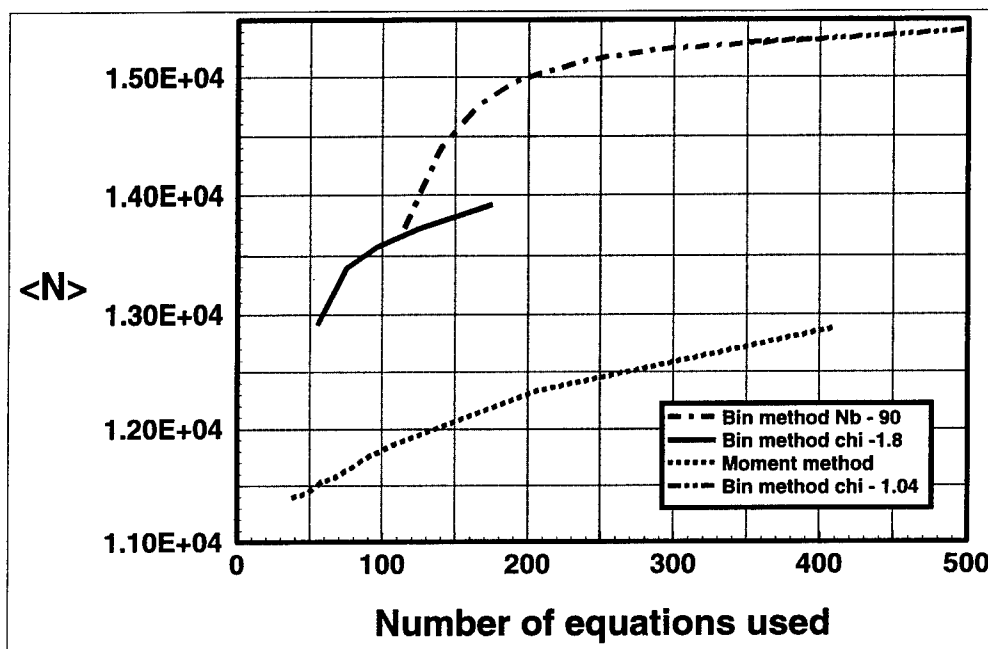
Figure 2. Average grain size plotted against number of equations used
for moment and bin methods. For the bin method, either the logarithmic
spacing for the binned equations or the grain size at which binning begins
is held constant

Novae in Celestial Backgrounds

The continuous novae spectrum can generally be described in three phases. At outburst, an optically thick fireball expands at constant velocity and constant bolometric luminosity, with a decreasing effective temperature. As the shell becomes optically thin, the continuous spectra consists of an optically thin blackbody in the visible, free-free excess at optically thin wavelengths, and an optically thick blackbody at long wavelengths, where the optical depth is dominated by free-free absorption. The effective temperature of the nova rises, while the bolometric luminosity remains constant, and the visible flux decreases. For many novae, particularly those with higher mass loss and lower luminosity, a dust formation event takes place which produces an optically thick shell in the visible, radiating as a ~1500 K blackbody in the infrared.

Parameters for a typical nova that will be used in determining the rate of occurrence of novae in the MSX

data are listed in table 2.

For the temperature of the novae, T is determined by the radius-luminosity-temperature relation when the shell is optically thick, and is picked so that the decline of the visible luminosity matches a decline speed of $t_2 \sim 50$ days in the optically thin phase.

Outflow velocity	V_{out}	$5.0 \times 10^7 \, \mathrm{cm \, s^{-1}}$
Sound speed	V_{sound}	$1.5 \times 10^6 \, \mathrm{cm \, s^{-1}}$
Shell radius	R	$V_{out}t$
Shell thickness	l	$V_{sound}t$
Luminosity	L	$10^5 L_\odot$
Effective Temperature	T	$\tau < 1 \quad T_\odot (L/L_\odot)^{1/4}(R/R_\odot)^{-1/2}$ $\tau > 1 \quad$ determined by $t_2 \sim 50$ days
Grain Temperature	T_g	$T(R_*/R)^{1/2}$
Mass Loss	M	$10^{-5}M_\odot$
Carbon Mass	M_C	$5 \times 10^{-2}M$
Grain size	a	$0.3 \, \mu\mathrm{m}$

Table 2.

The flux is modeled as

$$F_\lambda = (1 - e^{-\tau})B_\lambda * A + \varepsilon_\lambda^{FF} * V * e^{-\tau}$$

where τ is the optical depth at the given wavelength, A is the area of the shell, V is the volume of the shell, and ε_λ^{FF} is the free-free emissivity (Rybicki and Lightman 1979),

$$\varepsilon_\lambda^{FF} = \frac{d\nu}{d\lambda}\varepsilon_\nu^{FF} = \frac{c}{\lambda^2}\left(\frac{2^5\pi e^6}{3mc^3}\left(\frac{2\pi}{3km}\right)^{1/2}T^{-1/2}Z^2 n_e n_i e^{-h\nu/kT}\bar{g}_{ff}\right)$$

Approximately half of all novae form dust shells, so for the purposes of these calculations a typical classical novae has a 50% chance of forming an optically thick dust shell at $T_g = 1500\,\mathrm{K}$. It is also assumed that the hydrogen is completely ionized.

Figures 3 and 4 show the average flux in each band for MSX bands A, $B1$, $B2$, C, D, and E. The values plotted are D^2F_ν, where D is the distance to the source in centimeters, and F_ν is the flux in Janskys. Figure 3 applies to a nova with an optically thick dust shell forms, and figure 4 applies to a nova which does not form dust.

The average rate of novae in our galaxy is $100\,\mathrm{y^{-1}}$ (Bode and Evans 1987). If the majority of these novae occur in the plane, and the solid angle subtended by the plane of the galaxy is approximately $0.2\,\mathrm{rad}$ by $2\pi\,\mathrm{rad}$, or $\sim 1.25\,\mathrm{sr}$, this yields a rate per year per steradian in the galactic plane of $80\,\mathrm{y^{-1}\,sr^{-1}}$. Assuming these novae are evenly distributed along a line of sight out to 20 kpc, but the area subtended by a solid angle passing through a flat cylinder is proportional to R, then the probability function of a novae occurring spatially will be

4-9

$p(r) = (5 \times 10^{-3}\text{kpc}^{-2})R$, where integration of $p(r)$ out to 20 kpc has been normalized to 1. The rate of occurrence of novae at a given radius looking out along a line of sight is then $\tau_N^{-1} = 0.4\,\text{y}^{-1}\,\text{sr}^{-1}\text{kpc}^{-2}RdR$. The timescale for these events will be days, which is much longer than the duration of the measurements, so the number actually seen will be the rate of occurrence multiplied by the duration of the event.
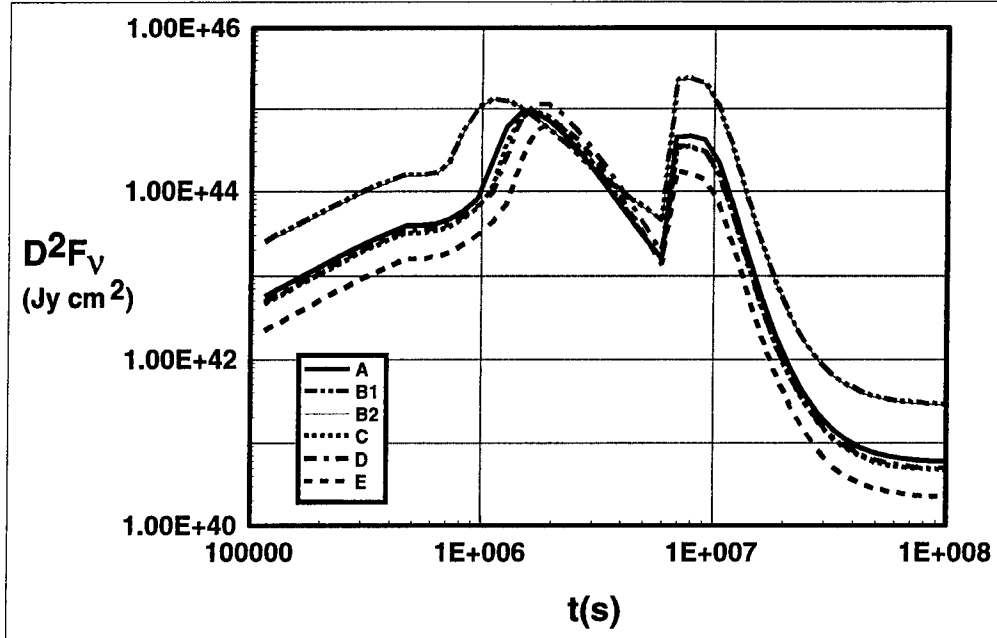

Figure 3. Band A flux, normalized by the distance to the source, for a typical dust producing nova.

4-10

The duration (Δt) that a novae will be intense enough to be seen by the instrument will change as the novae

occurs farther away from us, so the average number seen per steradian in an observation will be

$$N = 0.4 \int \Delta t(R) R dR$$

The results for each band are given in table 3.

Band	A	B1	B2	C	D	E
$N(\text{sr}^{-1})$	13.1	.47	.78	1.40	1.39	.46

Table 3.

At best, this should be considered an order of magnitude calculation, however, due to the assumptions

made throughout the calculation. To an order of magnitude, the rate of nova per observation per steradian in

the MSX data should be ~ 10 in band A, and ~ 1 in each of the other bands.

Nova V4361 Sgr
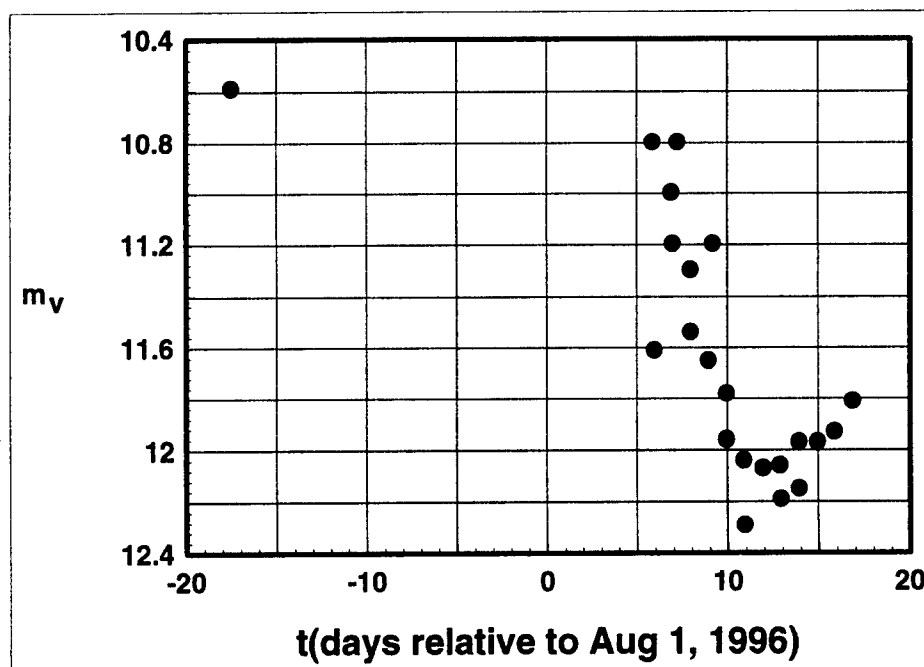
Figure 5. Light curve in V band for V4361 Sgr. All values are from IAU
circulars, and authors for each data are listed in table 4.

In the interest of finding novae in the MSX data set, any nova observed at visible wavelengths during the

time of the MSX mission were considered. Two novae occurred during the MSX mission that were observed in

the visible, and occurred in the galactic plane, but only one of these, V4361 Sgr, occurred shortly before MSX

observed that part of the sky. V4361 was first observed after outburst on July 11, 1996, at $b = -2.28$, $l = 13.7$. MSX measured this part of the sky once on July 19th, and later 3 times in early September. There was a point source detected in band A (8.28 μm), and no other bands, in the July 19th measurement, and no detections at all in the September data.

Table 4 gives data published in IAU circulars 6443, 6447, 6450, 6453, and 6454 by various authors. The visual light curve is plotted in figure 5.

Source	Day (Aug 96)	U	B	V	R	I	J	H	K
Nakano et. al.	-18.327			10.1					
Gilmore and Kilmartin	-17.502	11.89	11.69	10.59	9.79	9.04			
Monard	5.86			10.8					
Morrison and Argyle	5.94			11.61					
Ripero Osorio	6.88			11					
Morrison and Argyle	6.94			11.2					
Dillon	7.22			10.8					
Schmeer	7.9			11.3					
Morrison and Argyle	7.94			11.54					
Morrison and Argyle	8.93			11.65					
Dillon	9.15			11.2					
Sostero et. al.	9.924		12.78	11.78	10.92	10.14			
Morrison and Argyle	9.93			11.96					
Martin	9.965						8.93	8.73	8.35
Sostero et. al.	10.877		13.03	12.04	11.19	10.39			
Morrison and Argyle	10.93			12.29					
Morrison and Argyle	11.92			12.07					
Sostero et. al.	12.855		12.99	12.06	11.24	10.45			
Morrison and Argyle	12.92			12.19					
Sostero et. al.	13.917		12.97	11.97	11.17	10.38			
Morrison and Argyle	13.92			12.15					
Sostero et. al.	14.973		12.95	11.97	11.18	10.37			
Sostero et. al.	15.868		12.95	11.93	11.08	10.29			
Sostero et. al.	16.854		12.87	11.81	11.02	10.22			

Table 4.

Dust formation phase

A classical novae reaches a maximum in infrared wavelengths at the time the nova shell becomes optically thin in thermal Bremsstrahlung absorption. A second infrared emission phase can occur in novae which form dust. V4361 did have a significant dust formation event. There were 3 MSX maps that covered the area of the sky in which V4361 Sgr occurred after the dust formation event. The optical depth of the dust formation event,

computed by comparing the minimum of the light curve during the event with an extrapolation of the light curve from before the dust formation event, gives us an optical depth of $\tau_v = 1.1$ for the dust shell at the time of maximum extinction. However, the dust shell had expanded to the point of being optically thin well before the MSX measurements, so it is not surprising that no detection was made. While a direct estimate without knowing the dynamics of the shell is difficult, it is known that the light curves of all nova are similar on a dimensionless time scale, i.e., the ratio of the time at which an event occurs in the light curve to the outburst time is similar for all novae. If we consider an outburst time of July 10th, and a dust formation time of August 8th, and scale our typical A band light curve from figure 3 accordingly, we see that the flux around September 10th is 4 orders of magnitude less than the maximum Bremsstrahlung emission.

Bremsstrahlung emission phase

The July measurement did get a glimpse of emission in band A, at $\lambda = 8.28$ μm ($\Delta\lambda = 4$ μm), of .322 Jy, well above the sensitivity limit of the instrument (0.07 Jy). In units of F_λ, this is 1.41×10^{-15} erg cm^{-2} s^{-1} Å^{-1}. Due to the time of this measurement with respect to the novae outburst, and the fact that the value at this wavelength exceeds the blackbody radiation at the novae temperature, this is most likely thermal bremsstrahlung emission.

Color color correction

The nearest spectra to this date are the U,B,V,R,I spectra taken by Gilmore and Kilmarten on July 13.498. Given the very slow speed class ($t_2 \sim 200$ d) of the novae, and due to the fact that the dust formation does not occur for another 16 days, the spectra at the time of the MSX measurement should be approximately the same as the spectra taken 6 days earlier. The general trend in novae is towards a slowly rising temperature, with constant bolometric luminosity, so any error in doing this would lead to an underestimation of the IR excess due to free-free emission.

This data must first be corrected for reddening by foreground material. A value of $E(V - [12])$ for the galactic plane is taken from Egan and Price (1996).

$$E(V - [12]) = R(b,l) = \frac{0.1}{\sin(|b|) + 0.03(2 - \cos(l))}$$

Values from Whittet are used for the average interstellar extinction curve (1992). The interstellar extinction curve follows a power law in the infrared, given by

$$\frac{E(\lambda - V)}{E(B - V)} = 1.19\lambda^{-1.84} - 3.05$$

holds at least up to 5 microns. Assuming that the same power law holds beyond 5 microns, then

$$E(B - V) = \frac{-R(b,l)}{1.19[12]^{-1.84} - 3.05} = .329R(b,l)$$

4-13

The position of V4361 Sgr is b=-2.28, l=13.7, which leads to

$$E(B - V) = 3.29R(-2.28, 13.7) = 0.466$$

Band	m_λ	$E(\lambda - V)$	M_λ	f_λ	f_{BB}
U	11.89	.746	11.14	1.49e-13	1.35e-13
B	11.69	.466	11.22	2.11e-13	1.88e-13
V	10.59	0	10.59	2.11e-13	2.11e-13
R	9.79	-0.363	10.15	1.51e-13	1.83e-13
I	9.04	-.746	9.786	1.01e-13	1.27e-13
A	6.91	-1.41	8.32	3.83e-16	9.54e-17

Table 5.

While exact values require knowing the extinction A_V, relative values can be determined by using a value of $A_V = 0$. The blackbody spectrum shown is the best fit to the U, B, V, R and I measurements, using the method of simulated annealing, which matched a temperature of 5330 K. Dereddened values are listed in table 5.

Hydrogen gas density

If all of the radiation in band A is from Bremsstrahlung emission, the gas density at the time of measurement can be estimated. The main spectral line seen in novae outburst near band A is the NVI line at $7.6\,\mu m$, but that is generally seen much later in the nova outburst (Gehrz 1988). At the time the measurement is taken, the ratio of the infrared emission to a blackbody extrapolated from a fit to the $U, B, V, R,$ and I measurements yields

$$\frac{E_{FF}}{E_{BB}} = \frac{F_\lambda}{F_{BB}} = 4.01$$

Using the previous definitions of the nova flux,

$$\frac{E_{FF}}{E_{BB}} = \frac{(1 - e^{-\tau_v})B_v + \varepsilon_v^{FF}Le^{-\tau_v}}{\tau_{VIS}B_v}$$

This function is solved numerically for $Z = 1$, $T = 5330$, and $n_e = n_i = n$, to obtain a relationship between the shell thickness, L, and the gas density, n. The results are shown in figure 6.

The thickness of the shell needs to be less than 10^{12} cm for the shell to be in the optically thin regime. Clearly for any realistic values of L, the band A measurement is taken at an optically thick wavelength, and

$$\frac{E_{FF}}{E_{BB}} = \frac{1}{\tau_{VIS}} = (n_e\sigma_T L)^{-1}$$

For V4361 Sgr, $n_e = (4.0\sigma_T L)^{-1}$. While the geometry of this particular novae is not well known, given a typical shell thickness of $L=10^{13}$, a gas density of 4.2×10^{10} is calculated. Given uncertainty in the thickness of the nova shell, this should be considered at best an order of magnitude, and $n \sim 10^{10}\,cm^{-3}$.

n (cm^{-3})

1.00E+14

1.00E+12

1.00E+10

1.00E+08

1E+009   1E+011   1E+013   1E+015
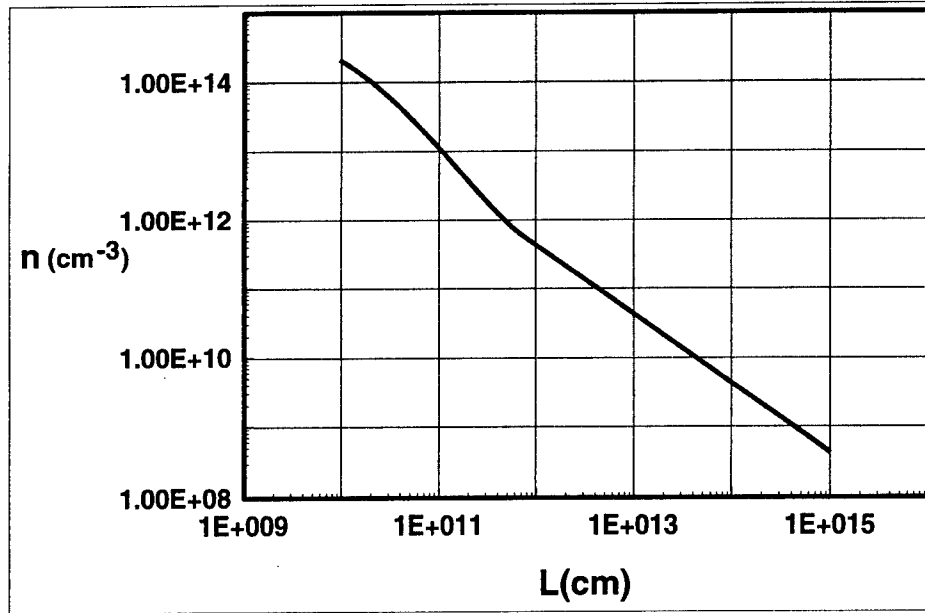
L(cm)

Figure 6. Results of numerical solution for shell density as
a function of shell thickness for V4361 Sgr.

Conclusions

Grain growth

In order to conserve mass, alterations are required in the method of Egan and Leung. We have implemented, but are still in the process of testing the results of these changes, both for the past application of this method to AGB stars, and to the current application of this method to the study of grain growth in nova shells.

For the case of monomer accretion, while there is good qualitative agreement between the bin and moment methods, there can be as much as 50% difference in the results of calculations for parameters typical of AGB stars. We intend to continue this testing as it applies to novae. Current results seem to imply that the bin method attains greater accuracy for a smaller number of equations. It should be noted, however, that this testing was for the case of monomer only accretion. It is not yet clear how well suited the bin method is to the growth of grains by accretion of larger clusters, and comparison of this to the moment method would help to further differentiate between these two methods. Also, while the bin method gives explicit information about the grain size distribution, the moment method requires the use of a reconstruction method to determine the grain size distribution. Future work should compare a maximum entropy reconstruction as in Vicanek and Ghoniem (1992) with the explicit distribution from the bin method.

Novae in the MSX data

Classical novae should be expected to appear in the MSX data set, but not in great abundance. However,

the timing of the experiment was sufficient to obtain useful infrared data for at least one nova, V4361 Sgr. While the likelihood of using MSX data to account for other classical novae is not high, one might consider the effect of dwarf novae on the MSX measurements, as their frequency is higher, and their eruptions are recurrent.

Nova V4361 Sgr

We confirm the sighting of a known nova, V4361 Sgr, in the MSX data, and compare the infrared flux with other visual measurements to calculate a hydrogen shell density of $10^{10}\,\mathrm{cm}^{-3}$ at July 19, 1996. Wagner et. al. report taking spectra of hydrogen Balmer lines, Fe II, and Ca II, but have not yet published an analysis of these lines to determine the outflow velocity of the source (Nakano et. al. 1996). Knowledge of the outflow velocity will help to better constrain these calculations.

References

Bode, M. F. and Evans, A. **Classical Novae**. New York, Wiley, 1987.

Egan, M. P. and Leung, C. M. *Grain Formation Around Carbon Stars. I. Stationary Outflow Models*. ApJ, 444:251-269, 1995.

Egan, M. P. and Price, S. D. *The MSX Infrared Astrometric Catalog*. AJ 112:2862-2871, 1996.

Gail, H.-P. and Sedlmayr, E. *Dust formation in stellar winds. IV - Heteromolecular carbon grain formation and growth*. A&A 206:153, 1988.

Gehrz, R. D. *The Infrared and Temporal Development of Classical Novae*. ARA&A, 26:377-412, 1988.

Kahaner, D. et. al. **Numerical Methods and Software**. Englewood Cliffs, NJ, Prentice Hall, 1989.

Martini, P. et. al. *Nova Sagittarii* 1996. IAU Circular 6453, 1996.

Monard, L. et. al. *Nova Sagittarii* 1996. IAU Circular 6447, 1996.

Morrison, L. V. et. al. *Nova Sagittarii* 1996. IAU Circular 6450, 1996.

Nakano, S. et. al. *Nova Sagittarii* 1996, IAU Circular 6443, 1996.

Press et. al. **Numerical Recipes in Fortran**. Second Edition, Cambridge University Press, 1992.

Rybicki, G. B. and Lightman, A. P. **Radiative Processes in Astrophysics**. New York, Wiley, 1979.

Sostero G. et. al. *Nova Sagittarii* 1996. IAU Circular 6454, 1996.

Vicanek, M. and Ghoniem, N. M. *Two-Group Approach to the Kinetics of Particle Cluster Aggregation*. Journal of Computational Physics, 101:1-10, 1992.

Whittet, D. C. B. **Dust in the Galactic Environment**. New York, Institute of Physics Publishing, 1992.

Yamamoto, T. and Nishida, S. Prog. Theor. Phys., 57:1939, 1977.

A COMPUTATIONAL ANALYSIS OF STACKED BLUMLEINS
USED IN PULSED POWER DEVICES

Johnelle L. Korioth
Doctoral Candidate
Department of Electrical Engineering

University of Texas at Dallas
2601 N. Floyd Rd.
Richardson, TX 75080

A COMPUTATIONAL ANALYSIS OF STACKED BLUMLEINS
USED IN PULSED POWER DEVICES

Johnelle L. Korioth
Doctoral Candidate
Department of Electrical Engineering
University of Texas at Dallas

Abstract

Blumleins are transmission-line structures that allow the formation and propagation of electromagnetic waves. They have existed for decades and their use has been widely documented for a variety of applications. The most common form of the single Blumlein is, perhaps, the three-conductor coaxial line. The widespread use and the coaxial cable's simple geometry lend itself well to today's needs. The tri-plate Blumlein configuration, on the other hand, is not as well known. Due to its more complex geometry, certain aspects must be considered which are not at all relevant in the coaxial case. This work attempts to explore the intricacies of not one triplate Blumlein, but a stack of such devices. A model has been constructed which not only accounts for wave propagation in the time domain, but also Blumlein charging and commutation. Each portion of the model has been compared to modified (existing) analyses of similar structures. The limits of validity for this analysis have also been tested through experimental studies.

A COMPUTATIONAL ANALYSIS OF STACKED BLUMLEINS
USED IN PULSED POWER DEVICES

Johnelle L. Korioth

Introduction

Modern applications for electromagnetic waves have a basis with the discoveries of Maxwell, Faraday, Ampere and Hertz. There has been much success in most all frequency ranges with regard to fundamental understanding and technological implementation. To some extent, though, there still exists a gap in the millimeter and sub-millimeter regions.[1] This zone is of great interest because some of the typical resonant frequencies of many biological and physical objects lie in this domain and, more simply, because this is the area of crossover from radio to optical frequencies. It is imperative that this gap be mastered if applications like enhanced radar systems, atmospheric chemical analysis, industrial materials processing, and advanced accelerators for high-energy physics research are to be realized. To this end, the primary thrust of this research is the development of a model for a stacked Blumlein microwave source used in such a radar system.

Model Development

In 1948, A. D. Blumlein patented a device[2] capable of both pulse formation *and* propagation. It consists of two transmission lines that share a common, charged conductor. When connected to a matched load impedance, Z_L, the measured output is, ideally, a rectangular pulse with an amplitude that is equal to the full charging voltage, V_0. The width of this pulse is roughly twice the one-way transit time of a constituent transmission line. The remarkable achievement of this invention is that it overcomes the obstacle of a regular transmission line for which only one half of the charging voltage, at best, is observable across a matched load. Because the transmission lines are effectively charged in parallel and later discharged in series, a stack of Blumleins (Figure 1) can be constructed whose output approaches the charging voltage multiplied by the number of Blumleins comprising the stack, thereby producing the additional benefit of voltage multiplication.

The charging and discharging of Blumleins is essentially a time domain problem. While the propagation of a pulse on a lossy line is best dealt with in the frequency domain, the transmission lines considered in this work are lossless. This means that frequency dependent dispersion is not a factor as long as only a single dielectric is present. The computational analysis, therefore, utilizes space-time diagrams,[3] otherwise known as bounce diagrams, for a purely time-domain treatment of stacked Blumlein pulse generators. However, the method of moments is first employed to calculate the system parameters, such as the matrices for the capacitance per unit length and the characteristic impedance.
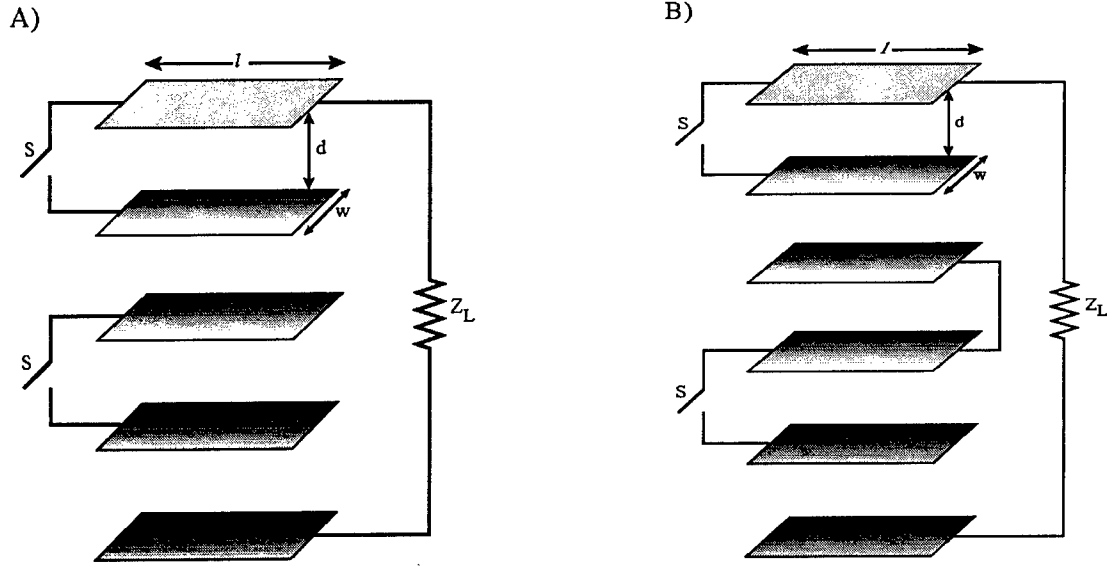
Figure 1: A stack of two Blumleins in the (A) shared and (B) separate conductor configurations. In both instances, the conducting plates are all separated by a distance d. For configuration in (B), however, the spacing between Blumleins is variable.

In this research, the moment method was applied in two dimensions by employing the following equation[4]

$$\Phi_i = -\frac{2\lambda_i}{2\pi\varepsilon}\int_0^{w_i/2}\ln x\,dx - \sum_{j\neq i}^{M}\frac{\lambda_j w_j \ln|\vec{r}_i - \vec{r}_j|}{2\pi\varepsilon}$$

$$= -\frac{\lambda_i w_i}{2\pi\varepsilon}\left[\ln\frac{w_i}{2}-1\right] - \sum_{j\neq i}^{M}\frac{\lambda_j w_j \ln|\vec{r}_i - \vec{r}_j|}{2\pi\varepsilon},$$

where Φ_i is the known potential at the center of the ith subsection. The first term on the right hand side of the equation represents the potential of the ith subsectional element due to itself. The second term reflects the influence of all other elements. In this case, w is the width of each subsection. It is constant for all M elements of the structure. In other words, $w_i = w_j = w = W/m$. The variable λ_i is the linear charge density for each element to be determined in the computation. Although it is evenly distributed over each element, the charge density is treated as a point charge located at the center of the subsection. The distance between elements is $r_i - r_j$. Thus the final form of equation above is

$$\Phi_i = -\frac{w}{2\pi\varepsilon}\left[\lambda_i(\ln\frac{1}{2}-1)+\sum_{j\neq i}^{M}\lambda_j \ln|\vec{r}_i - \vec{r}_j|\right].$$

5-4
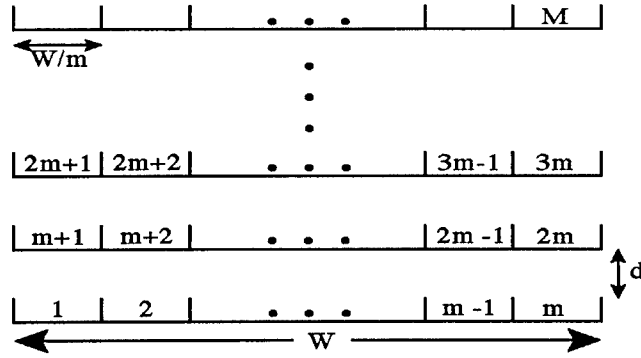
Figure 2: Cross-sectional view of a stack of N Blumleins. Each conducting plate is divided into m equal segments, creating a total of M elements for the entire structure.

There are M of these equations to solve simultaneously for the M charge densities. This is easily accomplished with a computer software package designed to handle matrix operations, such as MATLAB. The matrix equation used for this research is

$$[\Phi] = [C]^{-1}[q],$$

where $[\Phi]$ is an M x 1 matrix of the potential on each subsectional element. $[C]^{-1}$ is the inverse of the capacitance-per-unit-length matrix. The inverse capacitance matrix can be generalized as follows

$$[C]^{-1} = \frac{1}{\varepsilon}[fg]$$

where *[fg]* is the "per-element" matrix of geometric factors.[5] This matrix is computed instead of *[C]^{-1}* because it can be used to calculate matrices for quantities such as inductance, impedance and admittance. In order to proceed with the development of the model, however, the "per-element" matrix of geometric factors has to be reduced to a matrix with "per-plate" entries, with one of those plates as a reference. This is required because the electric potential between plates is measured with respect to some point of reference. Without this reduction, we would therefore be unable to properly keep track of the transient waves (and their associated voltages) established and propagated by a stack of Blumleins.

The process of reducing the "per-element" matrix of geometric factors to a "per-plate" one is not accomplished by simply summing all [fg] matrix elements for each plate. When calculating the matrix of geometric factors per plate, *[FG]*, we must first invert *[fg]*, then perform the summation of *[gf]* matrix entries for each plate. This produces *[GF]*, which is the $n \times n$ inverted "per-plate" matrix of geometric factors having matrix elements

$$GF_{ab} = \sum_{i=m(a-1)+1}^{am} \left(\sum_{j=m(b-1)+1}^{bm} gf_{ij} \right).$$

Inverting the *[GF]* matrix finally yields the "per-plate" matrix of geometric factors. Now, this needs to be reduced yet further so that the bottom-most plate becomes the point of reference for the system. This is accomplished with the following equation

$$Fg_{ij} = FG_{i+1,j+1} - FG_{i+1,1} - FG_{i,j+1} + FG_{11} \qquad i = 1...n-1 \quad j = 1...n-1,$$

where Fg_{ij} are the elements for the reduced "per-plate" geometric factor matrix, *[Fg]*.

Now that these fundamental matrices have been determined, it is straightforward to compute the capacitance and characteristic impedance of the stacked Blumlein structure. The per-unit-length characteristic impedance matrix is given by

$$[Zc] = \sqrt{\frac{\mu}{\varepsilon}}[Fg],$$

while the other circuit parameter, the per-unit-length capacitance, is related to *[Fg]* by

$$[C] = \varepsilon[Fg]^{-1}.$$

These matrices alone do not give all of the information needed to track the propagation of TEM waves. They do, however, prove necessary in the determination of the scattering matrix for each termination of the stacked Blumlein. At the switching end, we find

$$[S0] = \left(\frac{[ZT1] - [Zc]}{[ZT1] + [Zc]}\right),$$

where *[ZT1]* is the termination impedance matrix at the switch end of the Blumlein. At the opposite termination we find

$$[SL] = \left(\frac{[ZT2] - [Zc]}{[ZT2] + [Zc]}\right).$$

[ZT2] is the termination impedance matrix for the load end of the Blumlein. Consequently, a properly matched load must be determined that is a scalar value, not a matrix.

As seen in Figure 1, the load is placed between the outermost plates. Ideally, a load whose impedance matches that of the Blumlein stack will have an optimized output. As Figure 3(A) indicates, the load "sees" the series summation of the four adjacent-plate impedances if there is no field coupling between non-adjacent plates. Complications arise because that field coupling does indeed exist, as evidenced in Figure 3(B).

The stacked Blumlein model computes and suggests two reasonably "matched" loads. The first is simply the series summation of each transmission line's characteristic impedance (Figure 3(A))

$$ZL = zc_{11} + \sum_{i=1}^{n-1} zc_{i,i+1}.$$
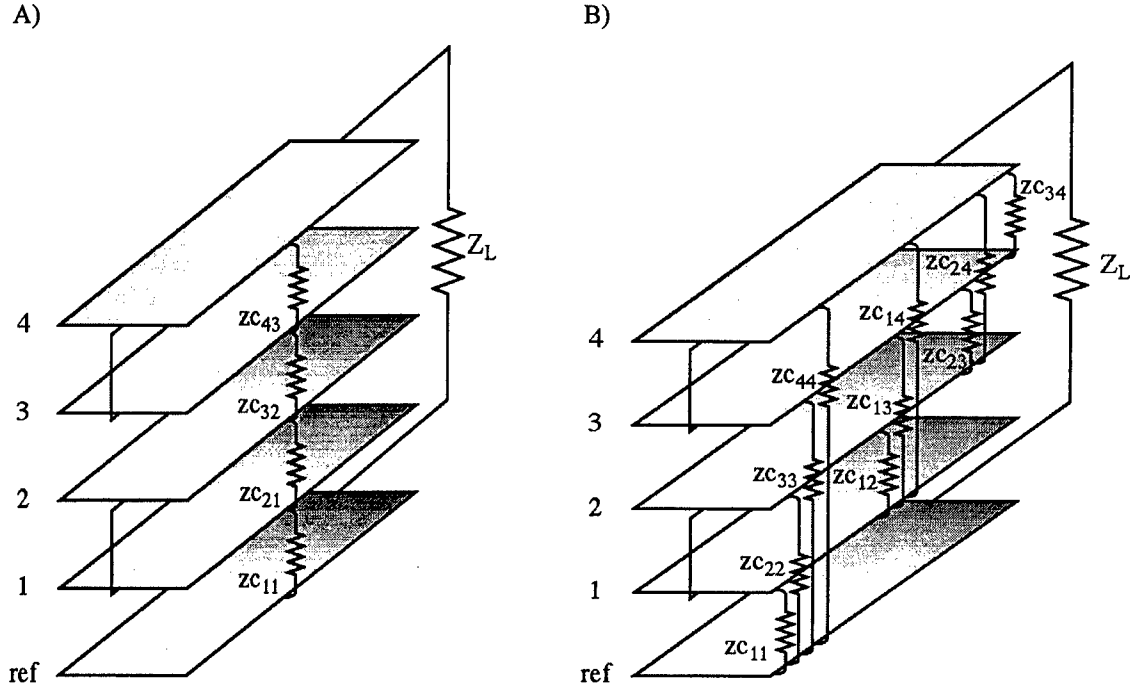
Figure 3: (A) The generally accepted view of the characteristic impedances involved in obtaining a "matched" load of a stacked Blumlein. (B) The matrix formulation of this problem reveals all of the "other" characteristic impedances present for this structure, complicating the computation of a true "match." (The placement of impedances does not reflect their actual position.)

The second includes coupling contributions. For a stack of two Blumleins that have no spacing between them (Figure 3(B)), this amounts to

$$ZL = \left(\left(\frac{1}{zc_{11} + zc_{12} + zc_{23} + zc_{34}} \right) + \left(\frac{1}{zc_{22} + zc_{24}} \right) + \left(\frac{1}{zc_{44}} \right) \right)^{-1}.$$

Since the load is connected solely between the outermost conductors, we need only concern ourselves with single or equivalent series impedances that mirror that connection.

Having determined all of the pertinent matrices, all that remains is the utilization of space-time diagrams to track the propagation of the transient TEM waves. This is accomplished with voltage vectors and matrices. As Figure 4 indicates, all potential differences are measured with respect to the bottom-most plate. In this case, the electrostatic potentials are shown. If the stack of Blumleins shown in Figure 4 is charged to a voltage V_0, the resulting static potential vector is

$$[Vs] = \begin{bmatrix} V_0 \\ 0 \\ V_0 \\ 0 \end{bmatrix}$$

5-7
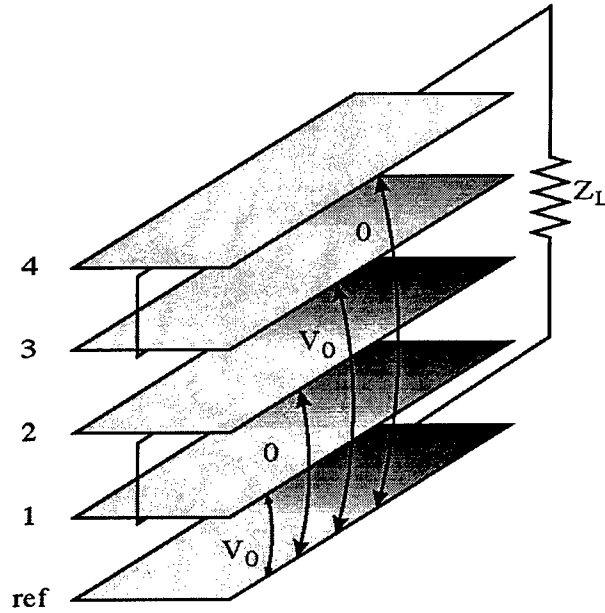
Figure 4: The "illustrated" components of the static potential vector. "Vector" simply refers to a single column matrix.

and the static voltage matrix is

$$[vs] = \begin{bmatrix} V_0 & -V_0 & 0 & -V_0 \\ -V_0 & 0 & V_0 & 0 \\ 0 & V_0 & V_0 & -V_0 \\ -V_0 & 0 & -V_0 & 0 \end{bmatrix}.$$

Once the switches are closed, the first transient waves are established. Their voltage component is determined by

$$[Vt1] = \left(\frac{-[Zc]}{[Zc] + [ZT1]} \right) [Vs].$$

When the waves reach the load termination, they undergo another reflection governed by the scattering matrix *[SL]*. Thus, the second set of traveling waves have voltage components evaluated by

$$[Vt2] = [SL][Vt1].$$

(Although not shown here, the total voltage vectors and matrices for each termination are also computed.) During the third transit time, the second set of transient waves reaches the $z = 0$ termination, where the scattering matrix is *[S0]* and forms the third set of traveling waves whose voltage components are

$$[Vt3] = [S0][Vt2].$$

The process is repeated for ten transit times, which is usually long enough to establish the dissipation of energy for well matched loads.

Results

The simulation of pulse formation and propagation in stacked Blumleins is performed by a program written with MATLAB (Version 4.0 for Windows). This analysis is very versatile despite being limited to a single homogeneous dielectric and only one basic conducting plate geometry. The flexibility arises from the number and type of variables that are required as input. First and foremost, the user must enter the number of Blumleins being stacked. The code is capable of handling a single Blumlein, as well as stacks of two or more. If the user wishes to investigate multiple Blumleins, they are then prompted for the vertical distance between the Blumleins, where an entry of zero corresponds to shared conductors, as seen in Figure 1.

The user must enter the length and width of the constituent conducting plates of the Blumleins, as well as the distance that separates them. The thickness of a plate is considered infinitesimally thin. Each plate in the stack is assumed to have identical dimensions and equal vertical spacing. The volume between and around the conductors is filled with dielectric. The relative permittivity is, therefore, the final bit of structural information requested as input.

The accuracy of the simulation depends on the number of elements into which a cross-sectional slice of the stack is divided. For instance, reasonable results can be obtained if a conductor with a width of 2.54 cm is sectioned into 15 elements. The code, in that case, takes a noticeably shorter amount of time to run than if 50 elements were chosen. Of course, better results are generated as the number of elements increases, but this is at the expense of increased computational time. The choice of acceptable accuracy is left to the discretion of the user. For all plots displayed here, however, a 2.54-cm wide Blumlein is always divided into 50 subsections.

The user must also input the operational parameters of the stacked Blumlein system. These include the charging voltage and the load impedance. As mentioned earlier, two different load impedance values are calculated and displayed on the screen. The user can choose an impedance that optimizes either the voltage multiplication factor or the power of the main output pulse, or opt for another value entirely.

Due to errors that will arise (division by zero/multiplication by infinity), every open and short are assigned finite, non-zero values. Since this simulation is wont to treat a closed switch as a short, the user is presented with the opportunity of determining the resistance of the switching element. Although this treatment is not entirely accurate, it is more than adequate for this research, for the creation of a thorough model of a semiconducting photocondutive switch or a thyratron is beyond the scope of this work.

By requiring all of the variables mentioned above, the model is more complete than if the user were only to input the number of Blumleins, the characteristic impedance of the Blumleins, and the charging voltage for the system. Even though a single characteristic impedance is measured in the lab, theory dictates that it is produced by a combination of characteristic impedance measurements. Therefore, this computer model of stacked Blumleins incorporates all of this information to determine the capacitance and characteristic impedance of the structure. These matrices are then used to calculate the initial energy stored by the Blumlein and the "matched" load impedances, respectively. The initial energy is, in turn,

utilized in the computation of the energy efficiency of the stacked Blumlein. The load impedance is fed into the portion of the program responsible for generating the scattering matrix for the $z = l$ termination, and also into the equations used to compute the final energy seen across the load.

Because of this, the matrices for characteristic impedance, capacitance, and scattering at both ends of the stacked Blumlein are displayed on the screen. It is trivial to modify the code so that it displays any other matrix or vector encountered during each run of the program. This might include the voltage vector for any of the transient waves or the matrix of total voltage between all the plates in the stack for either termination at any desired time. All of the pertinent information about the structure and operational parameters of the Blumleins is available on the generated plots of voltage against transit time, which can be printed to the default printer. Perhaps the information of most interest that appears on these graphs is the energy efficiency and the voltage multiplication factor. The efficiency is determined by dividing the energy in the output pulse by the total energy initially stored by the stacked Blumleins, or

$$E_{initial} = \sum_{i=1}^{n-1} \left(\sum_{j=1}^{n-1} \frac{C_{ij} V_{ij}^2}{2} + \sum_{k=2}^{n-1} \frac{C_{i+1,k} V_{i+1,k}^2}{2} + \sum_{l=3}^{n-1} \frac{C_{i+3,l} V_{i+3,l}^2}{2} + \frac{C_4 V_4^2}{2} \right),$$

if, for example, there are two Blumleins, and

$$E_{final} = \frac{V_{out,max}^2}{ZL} 2\tau.$$

The energy initially stored in the structure is calculated by adding the energy stored between all plates. Obviously, some sets of plates store nothing because the electrostatic potential between them is zero. The output energy is comparatively easy to compute as it involves only the maximum voltage of the main output pulse, the temporal width of that pulse, and the load impedance.

The voltage multiplication factor is calculated by dividing the maximum output voltage of the main pulse by the charging voltage.

$$VMF = \frac{V_{out,max}}{V_{charge}}$$

Ideally, the voltage multiplication factor should be equal to the number of Blumleins being stacked. As the following simulation results indicate, this hardly ever occurs. What *is* noticeable, though, are the trends that appear with changes to input variables such as the number of Blumleins and the choice of load impedance. As can be deduced from the plot below, there is a definite correlation between efficiency and the number of Blumleins. It is easy to conclude that as the number of Blumleins increases, the efficiency suffers a marked decrease. The graph in Figure 5 shows this trend as the ratio of plate separation, d, to plate width, w, varies. We might gather from the plot that a more efficient machine can be built by minimizing the geometric ratio. In reality, though, there is a limit as to what is physically plausible. The graph also suggests that the number of Blumleins in a vertical stack should be kept below four or possibly five due to the fact that beyond this limit, the efficiency drops below what most would consider an acceptable level.
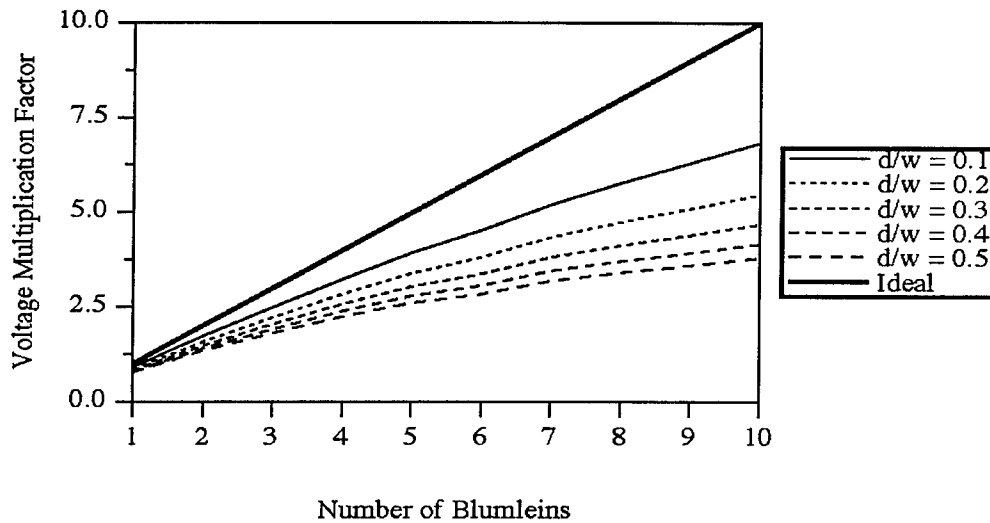
5-10
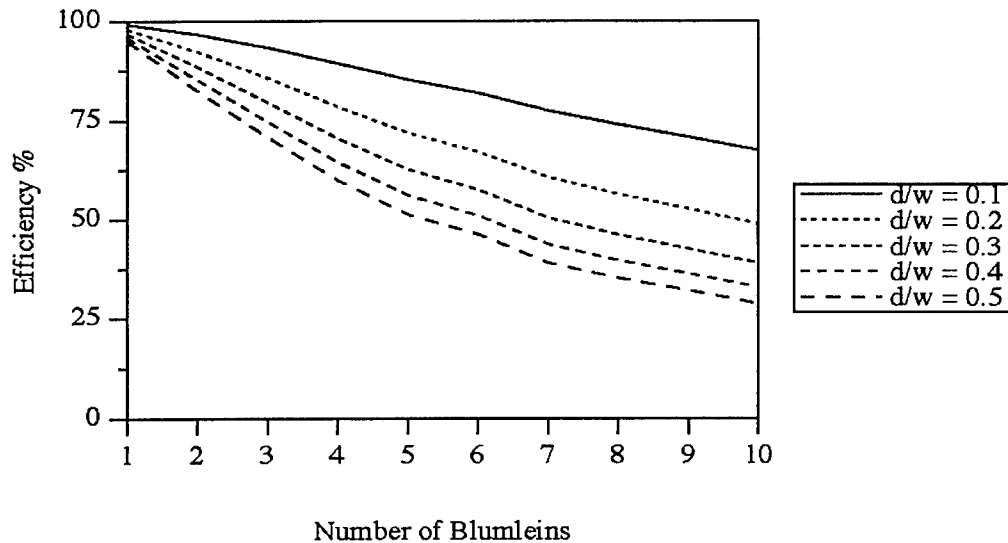
Figure 5: Variation of efficiency with the number of Blumleins in a stack and the geometric ratio, d/w. The following variables are constant: dielectric constant (transformer oil), Blumlein separation (none), and load impedance (efficiency maximized).

The trends of the graph in Figure 5 are hardly surprising. As the geometric ratio increases, the capacitance decreases and the characteristic impedance increases. Clearly, the amount of energy initially stored will be affected (diminished) by the change in capacitance. The variation in the characteristic impedance translates to an alteration of the computed load impedance suggestions. As the characteristic impedance increases, so does the load impedance since it is calculated with the elements of the aforementioned matrix. Recall, too, that the load impedance is used to determine the termination impedance matrix, which is in turn involved in the evaluation of the scattering matrix for the load end of the Blumleins. Additionally, the characteristic impedance matrix is itself a component of the scattering matrix calculation. Thus, a change in the elements of the scattering matrix will evoke a response in the vectors and matrices of the voltage component of the waves formed and propagated by the Blumleins. As the maximum voltage across the load diminishes, so too will the energy and efficiency. Clearly, then, increasing the geometric ratio only serves to decrease the efficiency of a stack of Blumleins.

As the number of Blumleins increases, field fringing and coupling occurs between more and more conductors. The strength of field coupling is related to the characteristic impedance. The strongest coupling (smallest value of Zc) occurs between adjacent plates. Hence the majority of energy is found in the waves propagating between these plates. Even though the coupling associated with non-adjacent plates is weaker than that for adjacent conductors, the overall effect is the reallocation of some energy that would have otherwise been propagated between the adjacent conductors. We can infer, then, that the voltage associated with the propagating waves likewise diminishes. Thus, the efficiency of the device is lowered.
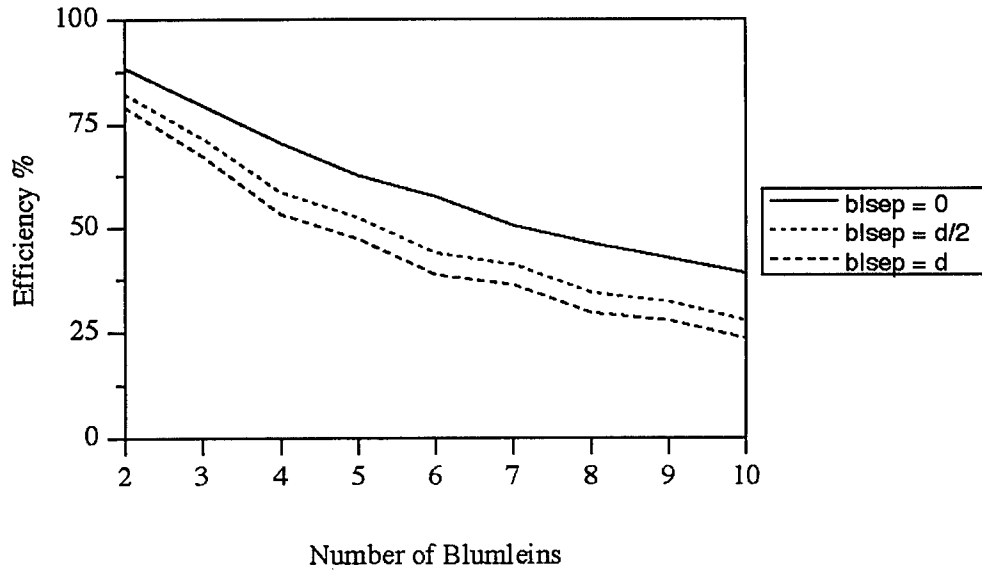
Figure 6: Variation of the voltage multiplication factor with the number of Blumleins in a stack and the geometric ratio, *d/w*. The following variables are constant: dielectric constant (transformer oil), Blumlein separation (none), and load impedance (efficiency maximized).

Parallel conclusions can be drawn upon investigation of the plot of the voltage multiplication factor versus the number of Blumleins (Figure 6). Because the maximum output voltage decreases with increasing *d/w*, the voltage multiplication factor will also suffer the same fate. Once again, the model seems to suggest that stacks of no more than four Blumleins are worth constructing in this particular situation.

The impact of conductor spacing is clear. Now consider the effect of the spacing between Blumleins, as depicted in Figure 7. We would expect the efficiency to fall off as the Blumlein separation increases for the same reasons discussed when the conductor separation was increased. Basically, the losses arising from the coupling of fringing fields become more pronounced with larger Blumlein separation because an additional wave is propagated between the top-most conductor of the lower Blumlein and the bottom-most conductor of the upper Blumlein. The wave is obviously eliminated when these two conductors are replaced by a single, shared plate. No energy is initially stored between these two conducting plates (they are at the same potential), so increasing the separation between them does not affect the amount of energy initially stored in the stack of Blumleins. The energy of the wave that travels between the conductors after switch closure must therefore detract from the energy available to the waves propagated by other adjacent conductors, thereby lowering the efficiency of the device.

The marked difference in efficiencies does not appear when the voltage multiplication factor is plotted against the number of Blumleins for a variation in Blumlein separation (Figure 8). Instead, increasing the separation between the Blumleins apparently increases the voltage multiplication factor. This comes about as a result of the extra wave propagated between each pair of Blumleins. Its voltage adds to all of the others, increasing the output despite the fact that all of the other waves have a slightly lower voltage as a result of the presence of that wave.

Figure 7: Variation of the efficiency with the number of Blumleins in a stack and the Blumlein separation, *blsep*. The following variables are constant: dielectric constant (transformer oil), geometric ratio ($d/w = 0.3$), and load impedance (efficiency maximized).
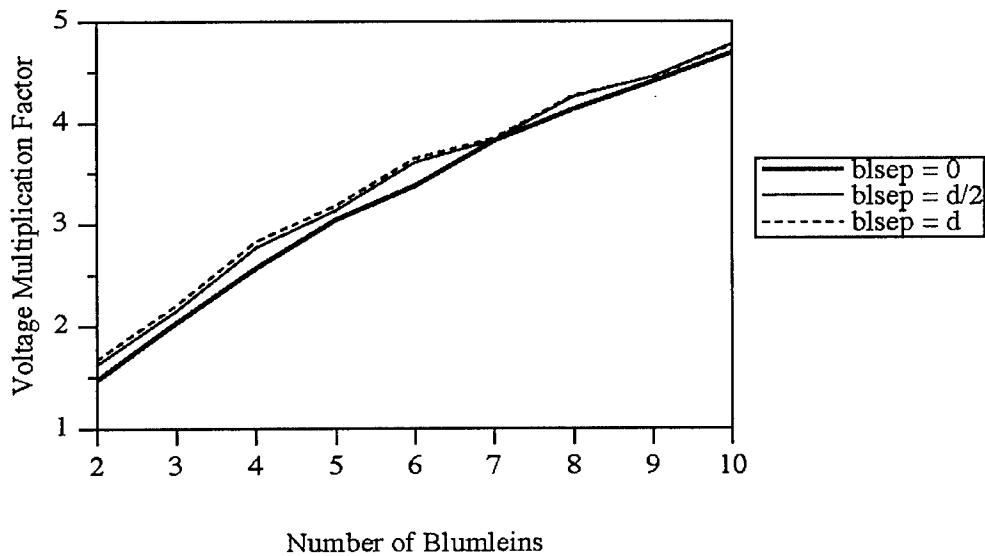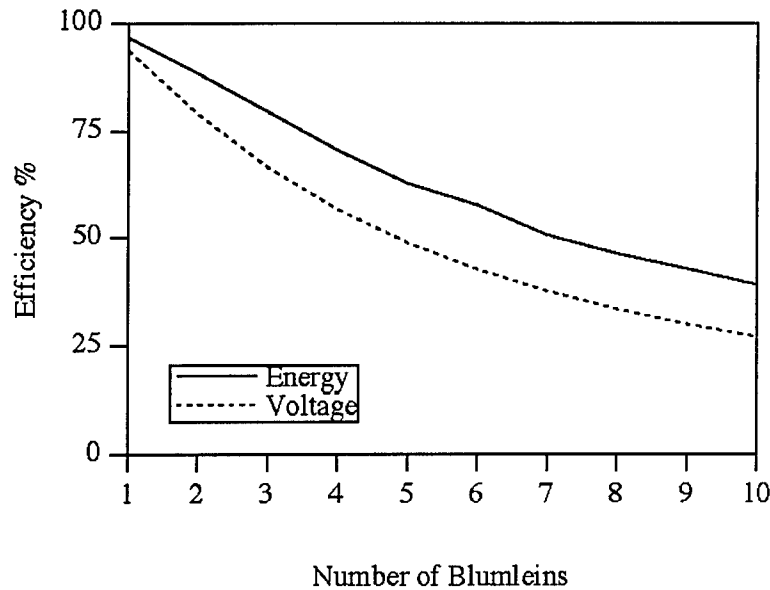

Figure 8: Variation of the voltage multiplication factor with the number of Blumleins in a stack and the Blumlein separation, *blsep*. The following variables are constant: dielectric constant (transformer oil), geometric ratio ($d/w = 0.3$), and load impedance (efficiency maximized).

The next two plots (Figures 9 and 10) nicely illustrate the effect that different load impedances have on the efficiency and voltage multiplication factor. Earlier, we saw the formulation of a "matched" load by omitting or including the characteristic impedances of some of the non-adjacent plates. It was suggested that a truer match might be made by including more characteristic impedances. In other words,

5-13

the latter formulation was more accurate because it allowed a larger portion of the wave to be transmitted, which meant that there were fewer reflections and that the stored energy was dissipated more quickly.

Since the load impedance is determined from the characteristic impedance matrix, the inclusion of more characteristic impedances in the load impedance computation results in a smaller calculated load impedance. Clearly, this also affects the scattering matrix for the load end of the Blumlein, thereby decreasing the maximum output voltage. Since the change in voltage is less pronounced than the change in load impedance, a greater efficiency is achieved. Thus, this method of determining a "match" is referred to as optimizing for higher output power or greater energy efficiency.

The omission of the characteristic impedances of non-adjacent plates, on the other hand, results in an increased load impedance because nothing is in parallel with the series equivalent of the adjacent plate impedances. This, then, decreases the efficiency because the output energy is divided by a larger number, despite the small increase in the maximum output voltage. It does clearly increase the voltage multiplication factor (Figure 10) because of that increase in output voltage. Hence, this "match" is denoted as optimization for a higher voltage multiplication factor. Obviously, if we were designing a stacked Blumlein pulse generator, we would have to decide which is more important for our intended application, a device which has better voltage multiplication capabilities or one that produces higher power pulses.

Figure 9: Variation of the efficiency with the number of Blumleins in a stack and the load impedance, Z_L (*energy* efficiency or *voltage* multiplication number optimized). The following variables are constant: dielectric constant (transformer oil), geometric ratio ($d/w = 0.3$), and Blumlein separation (none).
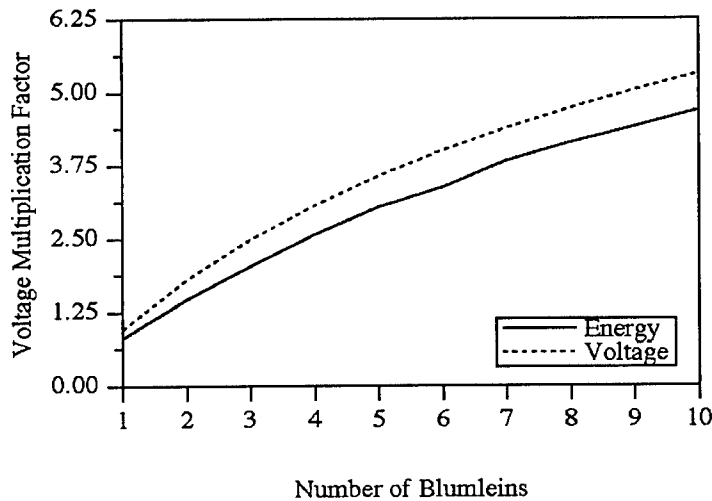
Figure 10: Variation of the voltage multiplication factor with the number of Blumleins in a stack and the load impedance, Z_L (energy efficiency or voltage multiplication factor optimized. The following variables are constant: dielectric constant (transformer oil), geometric ratio (d/w = 0.3), and no Blumlein separation.

Conclusions

(Due to the limited amount of space available, this section will be kept unusually brief. For a more in-depth discussion, please refer to my dissertation.)

The model of stacked Blumleins developed for this research was verified using three different procedures. The matrices for the capacitance, characteristic impedance, and scattering were checked against a frequency-domain software package from France called CRIPTE.[6] Excellent agreement was exhibited between the two models. The efficiency was compared to a QBASIC analysis written by lab scientist Jim O'Loughlin[7] that approximated a stack of Blumleins as a network of resistors. Due to major differences in treatment of this problem (circuit theory versus electromagnetic wave theory), agreement was not as well defined, although both methods concur that constructing stacks of more than two to four Blumleins would be unwise because of operation inefficiency. Finally, experimental results for a stack of two Blumleins were used. Again, the model agreed with reality as well as could be expected considering the approximations made during code development.

Obviously, more work can still be done. Future extensions of this research might include the introduction of multiple dielectrics, conducting plates of variable width, or conductor thickness. A more rigorous treatment of the terminations should also be attempted. For example, non-simultaneous switch commutation might be investigated, or perhaps the effects of attaching a TEM horn antenna might be explored. This naturally leads to questions pertaining to the determination of a better matched load. Finally, different parallel plate Blumlein arrangements should be considered, say side-by-side instead of vertical stacking. Clearly improvements can be made, but the model, as it currently stands, does provide a reasonable starting point for a researcher designing a stacked Blumlein pulse generator.

References

1. V. L. Granatstein and A. V. Gaponov-Grekhov, *High-Power Microwave Electronics: A Survey of Achievements and Opportunities*, Applications of High-Power Microwaves, A. V. Gaponov-Grekhov and V. L. Granatstein, editors, Artech House, 1994, pp.1 - 24.

2. A. D. Blumlein, U. S. Patent No. 2,465,840 (1948).

3. S. Ramo, J. R. Whinnery, and T. Van Duzer, Fields and Waves in Communication Electronics, John Wiley & Sons, 1994, pp. 213 - 320.

4. N. N. Rao, Elements of Engineering Electromagnetics, Prentice Hall, 1994, pp. 358 - 421.

5. C. E. Baum, T. K. Liu, and F. M. Tesche, *On the Analysis of General Multiconductor Transmission-Line Networks*, Interaction Note 350, November 1978.

6. CRIPTE (Calcul sur Réseaux des Interactions Perturbatrices en Topologie Electromagnétique) Version 3.0, developed by ONERA (Office National d'Etudes et de Recherches Aérospatiales) in France, 1998.

7. J. P. O'Loughlin, private communications, May 10 and July 27, 1995.

APPROXIMATING MORSE POTENTIALS NUMERICALLY AND ANALYTICALLY

Elizabeth Monaco
Research Student

Holy Cross College
1 College St.
Worcester MA 01610

APPROXIMATING MORSE POTENTIALS NUMERICALLY AND ANALYTICALLY

Elizabeth Monaco
Student
Holy Cross College
Department Of Chemistry

Abstract

Using the results derived by Akira Matsumoto and Kenichi Iwamoto

published in two papers[1,2] studying Morse potentials, we attempted to calculate

transition probabilities between vibrational levels. We used two methods for

calculating the probabilities, the first method involved numerically evaluating the

analytic eigenfunctions and the second method was to evaluate the analytic

solution to the electric dipole matrix elements, both of which were provided by

Matsumoto and Iwamoto's papers.

Introduction

Much research has been done on electric dipole matrix elements and vibrational transition probabilities and much data has been provided to approximate these values. However, there is still more to be learned at high vibrational levels and there is still a need for better, more accurate models of the potentials of diatomic molecules. We attempted to get numerical values for the current analytical solutions to then use for analysis of spectra obtained in the laboratory.

Methodology

For the first approach, we wrote computer programs in Series Processing Language for use with Dadisp software. The code was written in a style similar to C and the purpose of the programs was to numerically calculate the solutions to the analytic eigenfunctions. The eigenfunctions contain associated LaGuerre polynomials, so we had to write code to evaluate these polynomials using the recurrence function for these polynomials. Once the numeric results for the eigenfunctions were obtained, we plotted the Morse potential (using the equation in the two referenced papers) and overlaid the eigenfunctions (which were

6-3

normalized) with the potential and saw that they were well behaved. The next step in this project is to numerically calculate the transition probability between two levels by integrating the product of the two eigenfunctions and the radius (the operator). We expect that these numbers will match the numbers obtained in our other approach to the problem.

Our other approach was to take the analytic solution to the electric dipole matrix elements derived by Iwamoto and Matsumoto[1,2] and numerically evaluate it for molecular nitrogen using experimental spectroscopic values for W_e, W_eX_e and r_e taken from the Journal of Physical and Chemical Reference Data[3]. We confirmed that the programs written to carry out the calculations were working correctly by first reproducing the data for CO reported by Matsumoto and Iwamoto[1,2] before we then changed the parameters for our own experimental interests (N_2). We were then able to plot this data as relative transition probability versus the vibration level and see the trends in probability of transitions as you go up in vibrational level. The next step in this project is to see if these numbers match the probabilities calculated using the original eigenfunctions and to apply this information to experimental data. By theoretically modeling the transition probabilities, we can analyze experimental spectra by comparison of theoretical predictions to experimental results.

6-4

Results

At this point, it would be preliminary to report any official results because the two phases of the project have not yet been compared. Once it can be confirmed that both approaches to solving the problem give logical results, then these values can be reported and utilized in analysis of experimental spectra.

However it can be stated that at this point, all codes are running properly and appear to be giving correct numerical results. This is evidenced by overplotting the eigenfunctions with the Morse potential and seeing that they are well behaved as well as seeing reasonable looking plots of relative transition probability versus v level. This project is still underway and hopefully there will be some quantitative results to report in the near future.

Discussion

One suggestion for improvement to this experiment that may be implemented before its conclusion is to utilize a more powerful and scientifically capable programming language to carry out the calculations for actual data analysis. There still exists some concern that round off error and the limitations

6-5

on variable size may cause deviation from actual values. This is an area still under investigation. The programs involve very large numbers and exponents as well as utilize complex mathematical functions such as the gamma function and the recurrence functions for associated LaGuerre polynomials. Therefore the values of some variables within the program often approach the technological limits of the system on which they are being run.

However our results at this point in the project are reasonably similar to those found by other researchers. This is evidenced by the ability of our programs to reproduce the electric dipole matrix element values for CO reported by Iwamoto and Matsumoto[1,2].

Conclusion

At this point in the project, we feel that we have developed accurate and functional programs to calculate Morse potentials, vibrational transition probabilities and vibrational electric dipole matrix elements. We intend to finalize these programs, confirm the accuracy of their results and utilize this information in the analysis of spectroscopic data taken in the laboratory.

References

1.) Kenichi Iwamoto and Akira Matsumoto, J. Quant. Spectrosc. Radiat.

Transfer, vol. 55, p. 457-462, 1996

2.) Kenichi Iwamoto and Akira Matsumoto, J. Phys. B, vol 30, L335-L338, 1997.

3.) Journal of Physical and Chemical Reference Data, vol. 6, #1, p.195, 1977

CONDUCTING FLUID REAL-TIME 2-D ELECTRONIC INTERPOLATOR AND SPATIAL FILTER FOR WAVEFRONT SENSOR-TO-CORRECTOR INTERFACING.

TYRONE OSPINO-MARTHE
GRADUATE STUDENT
Department of Physics

UNIVERSITY OF PUERTO RICO
MAYAGUEZ CAMPUS
Mayaguez - P.R.
P.O. BOX 5000

CONDUCTING FLUID REAL-TIME 2-D ELECTRONIC INTERPOLATOR AND SPATIAL FILTER FOR WAVEFRONT SENSOR-TO-CORRECTOR INTERFACING.

Tyrone Ospino-Marthe
Graduate Student
Department of Physics
University of Puerto Rico/Mayaguez Campus

INTRODUCTION

The situation often exist in adaptive optics that the geometry of wavefront sensing is different than that of wavefront correcting. By virtue of Nyquist Theorem, more wavefront sensing elements are usually required than for wavefront correcting, and the geometrical arrangement may differ. In our case, the wavefront sensor has rectangular geometry while the correcting element has hexagonal. Another situation arises when the reconstructed wavefront solution is noisy and must be spatially filtered to the lower order modes. We propose a solution using the **Fluidic Interpolator Module(henceforth called FILM).**

An aqueous solution of $CuSO_4$ provides for a resistive medium which allows for freedom of movement. Electronically driven, etched copper circuit board traces and pads with the input geometry provide for spatially defined potentials in the medium. A receiving plate etched with the field distribution and resulting fluid potentials interpolates and smoothes the output plate data. When the output plate is "close" to the input plate i.e. the separation is much less than the separation between input plate elements, the output plate senses essentially bilinear interpolation. Separating the plates tends toward averaging of the fields, and hence 2-D smoothing and interpolation of the output data.

CONDUCTING FLUID REAL-TIME 2-D ELECTRONIC INTERPOLATOR AND SPATIAL FILTER FOR WAVEFRONT SENSOR-TO-CORRECTOR INTERFACING.

Tyrone Ospino-Marthe

Methodology

The procedures for solving these problems are the following:

a. I need to calculate in every point in the square 16x16 the capacitance, next calculate the contribution to every point to the square on the hexagonal, and to know the values for the capacitance in every 127 points in the hexagon.

b. Assuming and entry to voltages in the wavefront, calculate the total voltages in the square.

c. Calculate next the Charge in every point to the square 128 X 128.

d. Calculating the first layer, make it 16 times and calculating the 16 layers.

e. Addition noise to the principal function and make the process other time.

f. After to calculate the first layer, calculate again the 16 layers.

g. Make the electronic part constructing two parallels boards , one square 128x128 and other hexagesimal 127 under a "place" fill with $C_uSO_4 + 5H_2O$, with the three(3) axis movements.

Results

Here we have to solution many problems, one to the principal restriction are that I need to work in three-dimensions, and the formulas and bibliography's don't mentioned this cases in his examples. First, need us to solve and have clear the physics process here.

We idealize an square to 16x16 and apply this formulas for the corners, sides and interior.

CORNERS	$q_{ij} = q_o(2 + 1/\sqrt{2})$
SIDES	$q_{ij} = q_o(3 + 2/\sqrt{2})$
INTERIOR	$q_{ij} = q_o(4 + 4/\sqrt{2})$

must be remember , in this point the calculate is to the relative capacitance not the "real" capacitance, with this values we making a CAPACITANCE MAP (in all this process, the simulations, I will make it with matlab's programs).

7-3

Next to this calculus, find the contribution for every point to the square over the hexagon, calculate in every 127 point to the hexagon with 127 formulas, seeing geometrically the contribution with a superposition to the hexagon over the square and neglected the corners . Maybe one way to make this calculus are using numerical methods, maybe the relaxation method, images method, or other , but we can't used for geometrical problems.

Now knowing the contribution into the boards , we continuos with a program for to make a net with only voltages in specifics points in a matrix to 128x128, the positions are: (row ,column)

1,1	1,9	1,18	1,27	...	1,126	1,128
9,1	9,9	9,18	...	...	9,127	9,128
18,1	18,9	18,18	...	...	18,126	18,128
.	.	.	.	.	.	.
.	.	.	.	.	.	.
.	.	.	.	.	.	.
128,1	128,9	128,18	...	...	128,126	128,128

table-1

, this are others programs with **Matlab (with your graphic for analyze the behavior).**

Next to this, generates the matrix, we generates other matrix in 3-d and put the anterior matrix , how the floor to this one.

Now the procedure is calculate with the numerical method, *iteration method,* the values to the voltages in the other points in the net, different to zeros .
Here we have positions for to solve in the borders and in the interior to the 'imaginary' cube.

The method work graphically in this form:
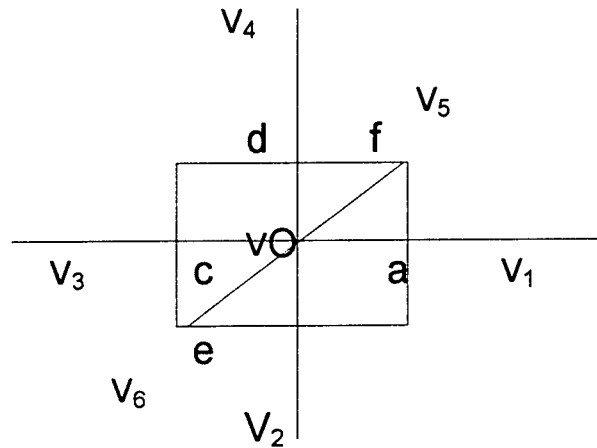
$$\frac{\partial^2 V}{\partial^2 x} + \frac{\partial^2 V}{\partial^2 y} + \frac{\partial^2 V}{\partial^2 z} = 0$$

$$\Delta x = \Delta y = \Delta z = \Delta h$$

$$\frac{\partial V}{\partial x}\Big|a \approx \frac{V_1 - Vo}{\Delta h} \Rightarrow \frac{\partial V}{\partial y} d = \frac{V_4 - Vo}{\Delta h}\Big|y \frac{\partial V}{\partial z} f \approx \frac{V_5 - Vo}{\Delta h}\Big|$$

In similar manner make it the other derivates, point's(d,f,c,b and e), next have:

$$\frac{\partial^2 V}{\partial X^2}\Big|po = \frac{\partial}{\partial X}\left(\frac{\partial V}{\partial X}\right)\Big|po = \left(\left(\frac{\partial V}{\partial X}\Big|a\right) - \left(\frac{\partial V}{\partial X}\Big|c\right)\right)\Big/\Delta h$$

$$V_1 - V_o - V_o + V_3 \Big/ (\Delta h)^2$$

$$V_1 + V_3 - 2VO \Big/ (\Delta h)^2$$

with the similar procedure, we calculate the other two axis (y,z), and have in the final:

7-5

$$V_1 + V_3 - 2VO + V_4 + V_2 - 2V_O + V_5 + V_6 - 2V_O = 0$$

$$V_1 + V_3 + V_4 + V_2 + V_5 + V_6 - 6V_O = 0$$

$$V_O \approx \frac{V_1 + V_2 + V_3 + V_4 + V_5 + V_6}{6}$$

We make the programs relative a this problem and I find a "solution", the iterations or the number of times, has many variations, the variation range are between [10-100] loops, we obtain various graphics showing the behavior to the simulation. We know that the behavior is good, analyzing the graphics. The betters behaviors was analyzed with 100 iterations, yours can see the next graphic.

simulating the floor of 3-d voltage matrix
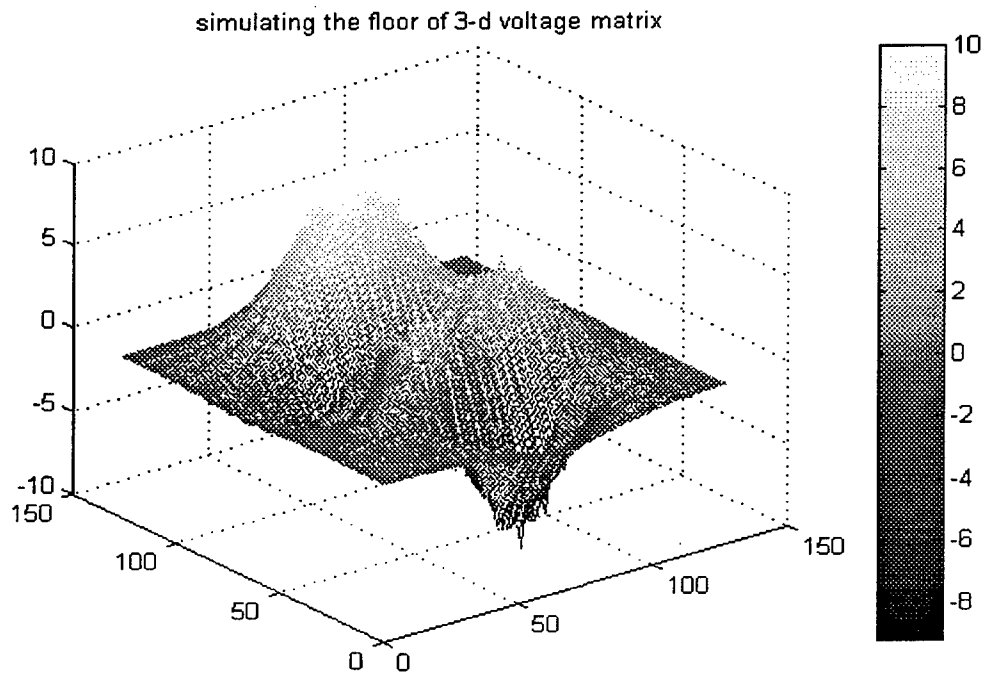
We look in this graphics, that have it a smooth slope, the peaks correspond to values generated by the "randomly peak" function , the range to the function are between [+10,-10] volts, and the extremes values in the anterior picture are +10 and -9.24 volts.

Other question in this part are to maintain fixed the points showed in table-1; Only the points around every these anterior points, will be modified . With this anterior process, we will fill the floor to the cube, every 128x128 points will has a value. The graphic to these fixes points are :

basic matrix-mvol
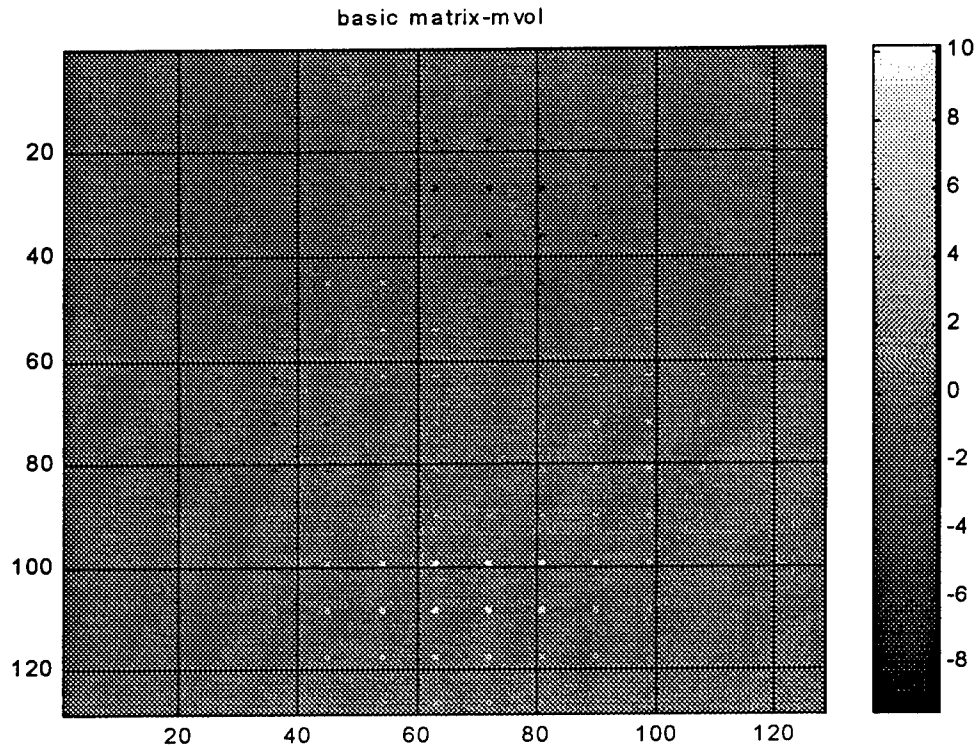
Now we work with the mother matrix (mvol) and will fill it in the "space" with 16 levels, graphing the first, eight and last levels, the first level is the same that the anterior "smooth peak matrix" (mvol3d). With a program, I calculate the voltage in every point, in this case, could change the values in the "specials points", and in the formula, use information about the upper space, we will neglected by be zeros in all the process; in this program the principal formula is:
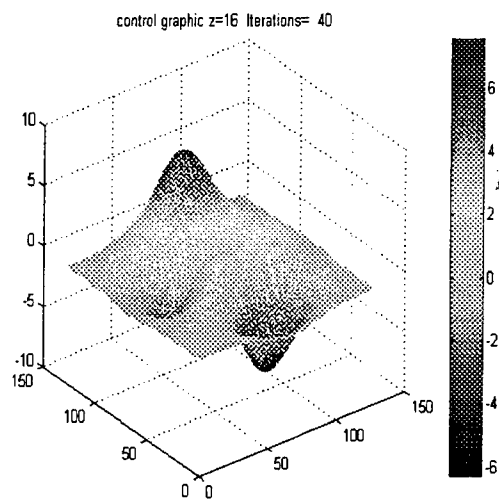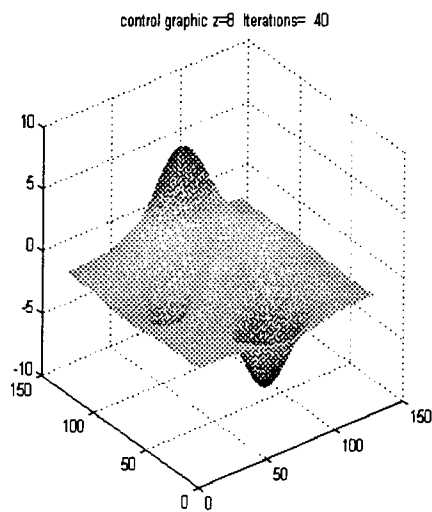
$$v(i,j,k) = (v(i,j,k-1) + v(i-1,j,k) + v(i+1,j,k) + v(i,j-1,k) + v(i,j+1,k)) / 5$$

this formula has changes if we work in the corners or in the borders to the spaces, modifying the numbers of factors by 3 or 4 (dependent). In this program we recalculates many times using iterations in the loops hoping by betters solutions and more exact values in every point.

The results, was good, we maintain the smooth slope and the figures are corrected in every layer with the iterations without error in the borders (we has many in the process), our last proof was with 40 iterations and finding the information in the 16 layers, the three graphics show the advantage using these mathematical method, and the figures, repeat again, look very good.

control graphic z=2 Iterations= 40
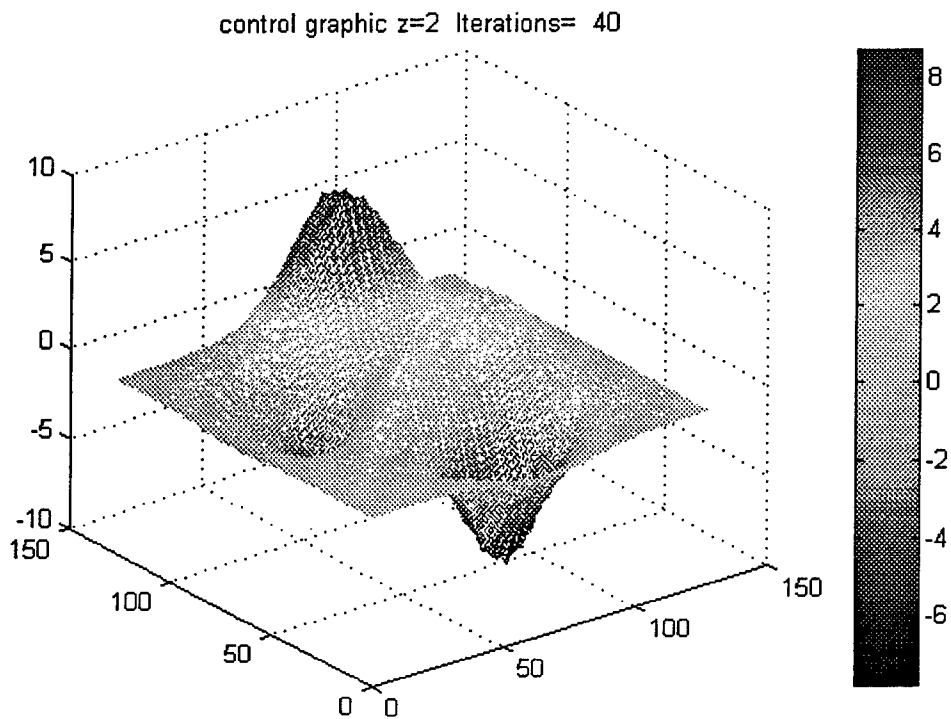
If yours look the graphic (z=2), yours can see the peaks and the uniformly picture, if you see z=8 and z=16, yours can see now how the method correct the images and convert a unstable picture in a smooth layer,

control graphic z=8 Iterations= 40

control graphic z=16 Iterations= 40

7-8

Next to the anterior process, we add noise to the signal and repeat a similar process that the anterior. We work with a noise signal generated with this equation:

noise = (2.5*((2*rand(16))-1)),

when **rand()** is the **Matlab** random function, [0,1], the random data's interval.

Now the   **final signal = "pure" signal + noise signal**

The "pure" signal is generated with a smooth peak function, in this simulation.
The process was similar but the result are different, logically.
In the reality, this is the kind of signal with that we work in the future, remember, all this process
is only computer's simulation's, when will go to the experimental table, or to the space, we will
work with many types to noise and with other types of turbulence.
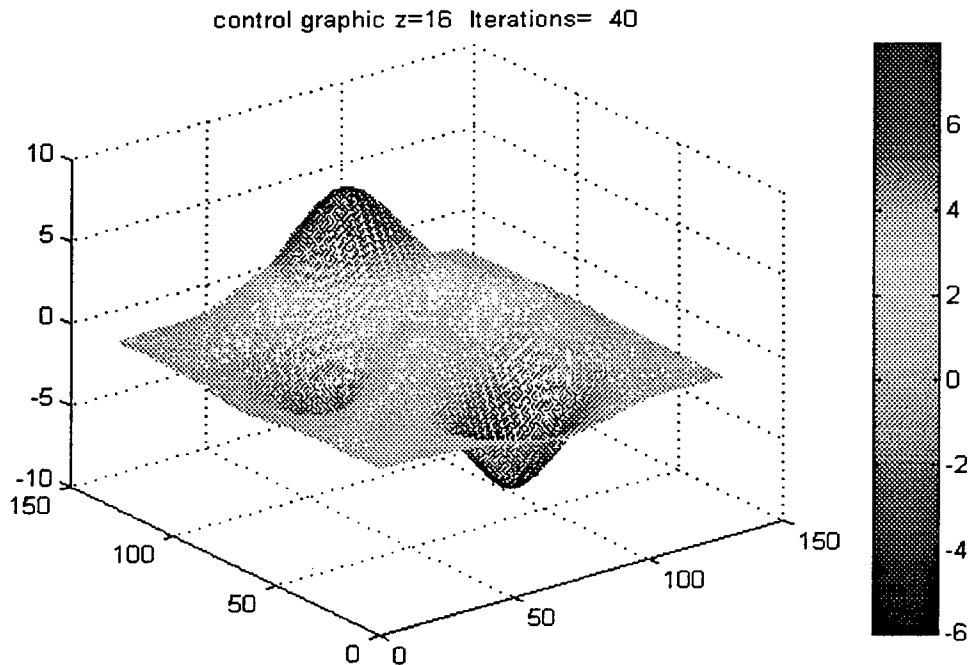With this process have this pictures:

First layer-iterations= 100
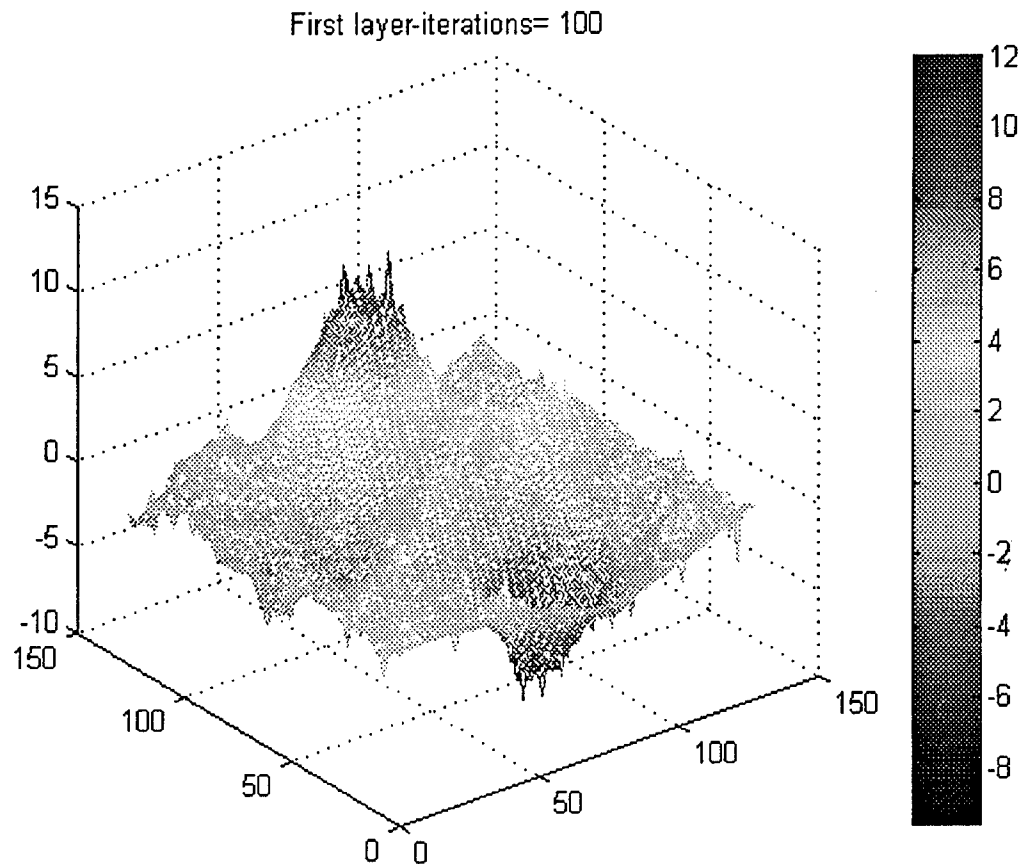
and the other graphic, with a comparison images picture,

7-9

Combination-simulation floor

combination - images graphic
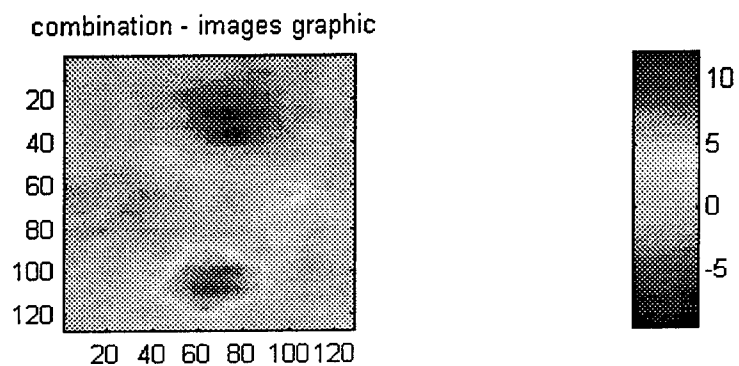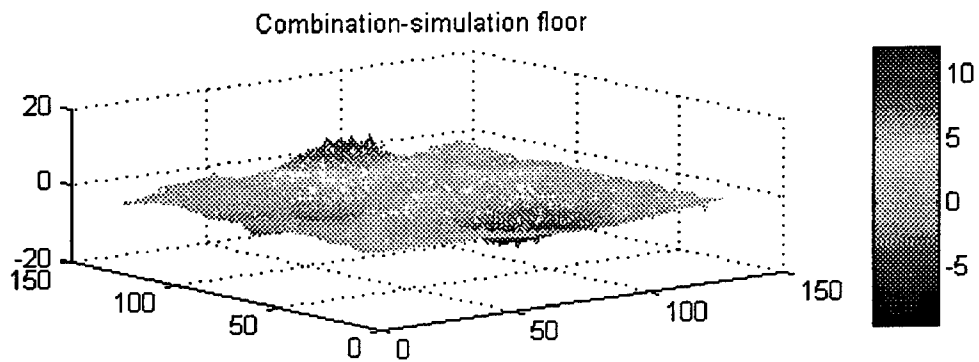
Now we make the process with the 16 layers and the graphics to the second, eight and sixteen layers are in the following pictures .
Yours can analyze the images process between the first layer , the eight layer and the sixteen layer,

control graphic z=8 Iterations= 40

control graphic z=2

control graphic

analyzing the last 10 rows

7-10

control graphic z=16 Iterations= 40
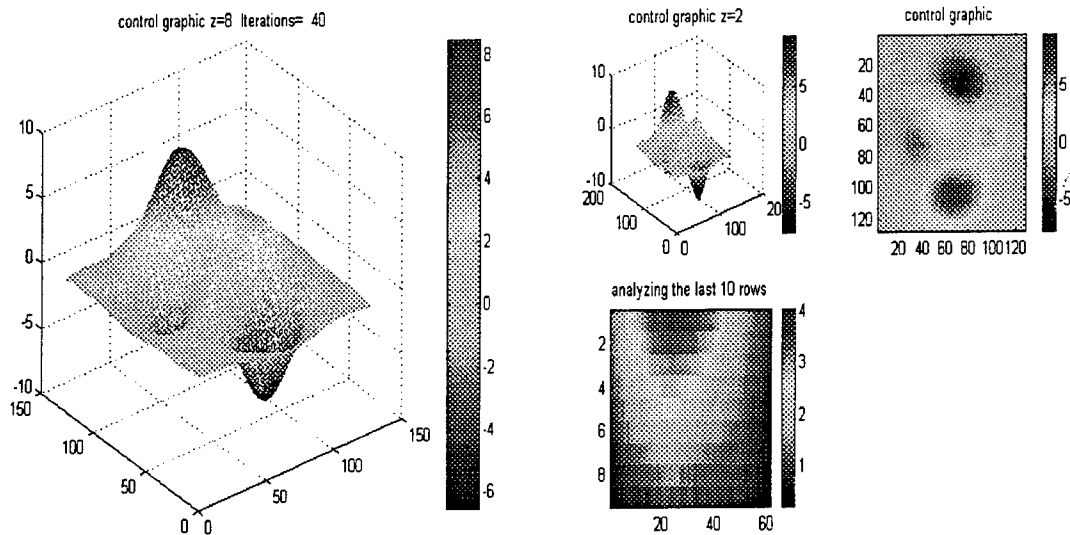
yours can see the change and how convert these method a distortion graphic in a smooth and clear picture, the mathematical method was functioning.

Now the process will consist in to construct the "electronic part", we will go now to the Real world, I need now to construct the hardware for all the process, to make all these simulations, "real".

I will construct two parallels boards, one square 128x128 and other hex127, these boards are immersed into a solution of cupric sulfate(C_uSO_4).

In the principle, the boards are fixed in the same axis, but next can it moved one into the space, the system has movement in the X axis with one plaque fixed and the other moved (hex127 plaque), moving in the Y axis (up, down), one fixed again and the other with movement and for last in the Z axis (left-right), how a car drive, again, one fixed and the other with movement.

I need too a mechanical system for control the movement to the board.
Yours can see the next schematic picture, and in there explain to yours graphically, how work in the real world the summer project, in this case put the **in's and out's** in the intermediate positions to the schema .

7-11

The picture is this:
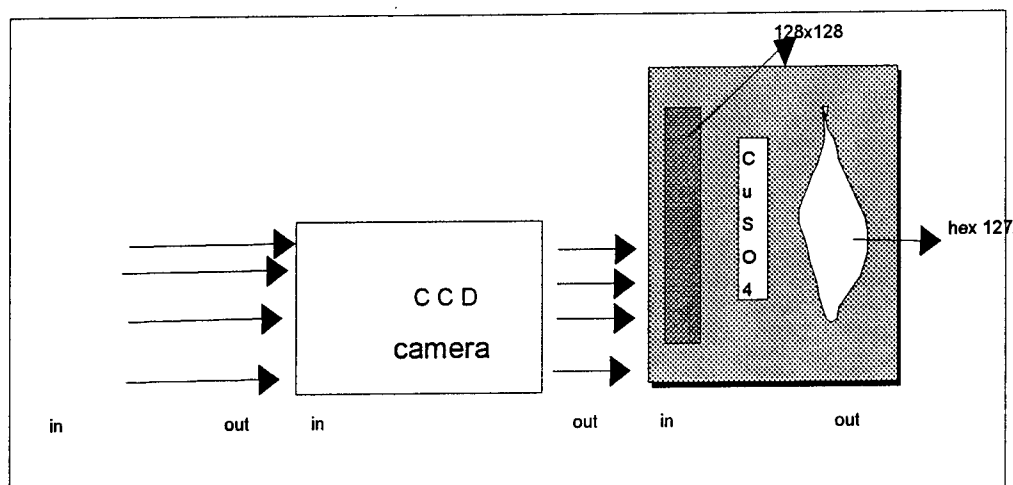
For this process , the solution between the boards (C_uSO_4, cupric sulfate), will server to us how medium to the " electric field movement" , if when we put near or fair the boards, this solution will work how medium and iterpolator.

I will construct the two terminals (one for transmit other receiving), one for every board, the "electricity" go out by the 128x128 terminal and will receive it the hex127 terminal, and the electric waves "surfer" into the cupric sulfate, when the process are finish, will see the changes(if have it) to the electric field and we can find the "perfect distance" between the boards and we know , what values has between the different separations, and will reconstruct the initial signal (square 128x128) in a final signal (hex127), we need too construct others boards, one for square and other for the hexagesimal board, with this boards, we make the amplification to the signal and transform a initial signal to 16 in a 256 signal, we will transmit the "pulses" and next to the capture, we make other board and make the remap in a hexagesimal 127.

How chemical information, we have that the volume susceptibility to the water is -90x10^{-6} and for the cupric sulfate is $C_uSO_4*5(H_2O)$ =+176x10^{-6}

This information will need it to calculate the perfect distance and the electric field make it how a constant value.

Others chemical properties are:
1. The cupric sulfate is soluble.

2. The cupric sulfate is soluble into the water

3. The chemical reaction by which it is formed is called a precipitation reaction.

4. The electrical properties to the elements are:

The last are only a few properties to the solution.

Re-writing about the electronic part, we can say that will need op-amp in the boards, in the moments don't have a electronic schema to the boards.

Conclusions

Maybe the conclusions about my summer job are only a few words, maybe the best or the betters conclusions are when I finish all the project, including the electronic part and makes the finals and "real" measures, the following punctual information reflex my personal conclusions to this part to the project:

1. Sometimes the mathematical method, in this case, iteration method, could help to the solution for our physics problems.
2. In this case, we can look the process graphically and we could saw how the figure change in every layer, to a not very smooth initial graphic, transform in a very smooth and "clean" final graph(with and without noise).
3. If you compare the noises graphics and the without noise graphic you can say that the initial graphics are very , very different but in the final had "similar" smooth pictures, saw the right bar in the graphic and saw to you the 'VOLTAGES" intervals , are both are similar.
4. In the real simulation, we will hope that the cupric sulfate work how the medium into the boards, and the "layers" in the computational simulations, are the different distances in the hardware world.
5. We can reconstruct initials signal, wavefront, by example, in pulses, and reconstruct in any form, in this case a 16x16 → 128x128 in 16 different layers.
6. Matlab are a very good software-packet for solve mathematical/physics problems.
7. The team work is very important to solve any problem, I received here, many and useful help, thank you for all.

Reference

Books

Masterton, Slowinski and Stanitski. *CHEMICAL PRINCIPLES*,Fifth edition,Saunders College
Publishing,Philadelfia,1981.

HANDBOOK OF CHEMISTRY AND PHYSICS, 61st edition, CRC press,1980-1981.

USING MATLAB MANUAL , version 5, The math works Inc, 1996

Horowitz & Hill, *THE ART OF ELECTRONICS*, Second edition, Cambridge university press,
Cambridge, 1989

Clayton R.P., Syed A.N., *INTRODUCTION TO ELECTROMECHANICS FIELDS*, Mc Graw Hill,
New york, 1982

Shampine, Gordon, *COMPUTER SOLUTION OF ORDINARY DIFFERENTIAL EQUATIONS.*

Van Bladel.J, *ELECTROMAGNETIC FIELDS*, Revides printing, springer-verlang editorial.

Eriksson.K, Estep.D, Hansbo.P, Johnson.C, *COMPUTACIONAL DIFFERENTIAL EQUATIONS*,
Cambridge University press

Articles

Zikanov.O , and Thess.A, *DIRECT NUMERICAL SIMULATION OS FORCED MHD
TURBULENCE AT LOW MAGNETIC REYNOLDS NUMBER*, (november 1997)

http://luda.uam.mx/cursoc2/tema2/interpol.html

www.gerpycna.gob.mx/SIR/cursoMDT/Tema1/Page16.html

http//:amiga.vip.at/uni/sls/kap06/f00.htm

SIMULATION OF PLASMA-WALL MIXING IN A MAGNETIZED TARGET FUSION CONCEPT

Kenny F. Stephens II
Doctoral Candidate
Department of Physics

University of North Texas
Denton, TX 76203

SIMULATION OF PLASMA-WALL MIXING IN A MAGNETIZED TARGET FUSION CONCEPT

Kenny F. Stephens II
Doctoral Candidate
Department of Physics
University of North Texas

Abstract

Magnetized target fusion provides a method to reach fusion ignition conditions that is intermediate to inertially confined and magnetically confined fusion schemes. Although a magnetic field is used to inhibit thermal conduction from the plasma to the confining liner, plasma-wall mixing still poses a problem. When this mixing occurs, increased impurities in the plasma reduce the plasma temperature and prevent the plasma from reaching ignition conditions. Computer simulations studying the effect of plasma-wall mixing due to the Rayleigh-Taylor instability in an imploding cylindrical linear are presented. The simulations are performed using the 2D magnetohydrodynamic code, MACH2.

SIMULATION OF PLASMA-WALL MIXING IN A MAGNETIZED TARGET FUSION CONCEPT

Kenny F. Stephens II

I. Introduction

Achieving controlled nuclear fusion has been a goal of the scientific community for several decades. Commonly employed schemes include Inertial Confinement Fusion (ICF) and magnetic confinement (MFE). Typical ICF methods compress a gas to sufficient density and temperature to initiate fusion. For the minimum laser energy, the implosion process must occur on time-scales shorter than the time required for thermal conduction into the capsule wall. This requires expensive driving systems which deliver the necessary energy on nano-second time-scales. Compressing a non-magnetized plasma on micro-second time-scales provides time for the high-temperature plasma to transfer energy to the environment. This reduces the plasma temperature and hence, the fusion rate. Yet the presence of a sufficient magnetic field within the plasma can reduce the thermal conduction between the plasma and its surroundings. This is the idea behind MFE designs. An alternative approach, whose density and time scales fall between those of ICF and MFE, is Magnetized Target Fusion (MTF).

Forming a union between ICF and MFE, MTF is a two-step process. The first stage requires the formation of a warm (~100 eV), magnetized (~100 kG) wall-confined "target" plasma prior to implosion. The "target" plasma is then quasi-adiabatically compressed by an imploding liner during the second stage. The joining of these two methods requires mating a plasma formation system with a target implosion driver. At the Air Force Research Laboratory-- Phillips Research Site, a plasma formation system has recently been combined with a quasi-spherical liner implosion system [1]. Since the magnetized plasma reduces the rate of thermal losses, electrical pulsed-power technology (which operates on micro-second time-scales) can be used. Such pulsed-power implosion experiments, similar to those required for MTF, have already been conducted [2-4]. Thus, the necessary technology and experimental know-how for MTF exists.

The principle feasibility issue for the MTF concept is the mixing of the fuel and boundary material. When a plasma is

SIMULATION OF PLASMA-WALL MIXING IN A MAGNETIZED TARGET FUSION CONCEPT

Kenny F. Stephens II

in contact with a material surface, heavy ions can be sputtered off the material. These sputtered ions are highly ionized and are responsible for large amounts of radiation losses. This increased radiative loss cools the plasma and reduces the chance of reaching ignition conditions. Although the magnetic field is intended to provide a barrier to plasma particles reaching the liner, instabilities can develop between the plasma and the liner that reduce the effectiveness of the magnetic field. A well-known source of non-uniform behavior in electromagnetic implosions is the Rayleigh-Taylor instability. In ordinary hydrodynamics, this instability occurs when a heavy fluid is supported, against the force of gravity, atop a light fluid. The interface between the two fluids becomes rippled and allows the heavy fluid to mix into the light fluid. In MHD, the roles of the heavy and light fluids can be assumed by the plasma and magnetic field, respectively. The Rayleigh-Taylor instability occurs when the acceleration points from the heavy fluid (plasma) to the light fluid (magnetic field). During implosion processes, the interface between the plasma and the liner can become unstable between the times of maximum inward liner velocity and maximum compression. In the simulations considered here, there is no magnetic field in the plasma. For this case, the plasma plays the role of the light fluid and the aluminum liner that of the heavy fluid. The present work considers plasma-wall mixing in a cylindrical liner due to the Rayleigh-Taylor instability.

Using the 2-1/2 dimensional magnetohydrodynamic code, MACH2 (Multiblock Arbitrary Coordinate Hydrodynamics, 2D) developed at the Air Force Research Laboratory -- Phillips Research Site, a cylindrical liner imploding on a deuterium plasma is simulated. Section II provides a brief description of MACH2. Section III details the simulation model. The simulation results are presented in Section IV. Conclusions and future simulation considerations are given in Section V. The input deck used for one of the simulations is provided in the appendix.

SIMULATION OF PLASMA-WALL MIXING IN A MAGNETIZED TARGET FUSION CONCEPT

Kenny F. Stephens II

II. MACH2 Description

MACH2 [5] is a finite-difference code that solves the time-dependent, single-fluid, multi-temperature MHD equations. Using an Arbitrary-Lagrangian-Eulerian multi-grid scheme, the problem geometry is constructed from multiple blocks (logically rectangular collections of cells) of arbitrarily shaped quadrilateral cells, in either planar or axi-symmetric coordinates. The code calculates all three components of the velocity and magnetic field, though no variation is allowed normal to the problem geometry (i.e., no z-dependence in planar problems or theta-dependence in cylindrical problems). The finite-differencing is carried out according to a finite-volume technique, along with second-order Van Leer convection and flux-conserving, constrained transport for magnetic advection [6]. Solving the resistive MHD continuity, momentum, energy and magnetic field equations, MACH2 closes the system of equations through the equation of state, of which several options are available. Among these are analytic and tabular models (SESAME tables at Los Alamos National Laboratory), which include the transport coefficients. Several options are available for radiation modelling. Multiple circuit solvers are also available.

III. Simulation Model

The simulation model [7] considers a 30 cm high aluminum liner with an inner radius of 4.9 cm and wall thickness of 0.1 cm. The liner encloses a deuterium plasma with a particle density of 10^{17} cm^{-3}. The liner and plasma originally have a temperature of 27 meV and 300 eV, respectively. The liner is connected to an RLC model of the SHIVA STAR capacitor bank. At t=0, the applied voltage is 84 kV with an inductance of 39 nH and resistance of 1 mΩ. The deuterium properties were determined from the SESAME tables, except for the resistivity and thermal conductivity for which a Spitzer model was used. For the aluminum, tabular values were used for the resistivity and thermal conduction coefficients, along with a Steinberg-Guinan elastic-plastic model. For simulations run in Eulerian mode, a hydrogen gas was allowed to flow through the outer boundary (i.e., radius) of the grid. This prevents the volume left

SIMULATION OF PLASMA-WALL MIXING IN A MAGNETIZED TARGET FUSION CONCEPT

Kenny F. Stephens II

behind by the moving liner to be filled with a non-physical aluminum gas. The hydrogen gas employed a tabular equation of state with constant electric diffusivity (10^4 m^2/s) and thermal conduction coefficients (10^4 W/m·eV). The gas was brought in at 0.2 eV and 0.01 kg/m^3.

Preliminary simulations were run in a Lagrangian fashion to allow the grid to follow the liner. These simulations used the initial conditions, as described above, and ran for 25 μs. The problem geometry was scaled from 30 cm down to 1 cm; the plasma and the aluminum were each dimensioned with 8 cells in the radial direction and 16 in the axial direction. As indicated in Figure 1, the liner reached a 2:1 compression ratio and a maximum inward velocity at ~18 μs. At approximately 22.5 μs, maximum compression occurred with a radius of about 1.5 cm.
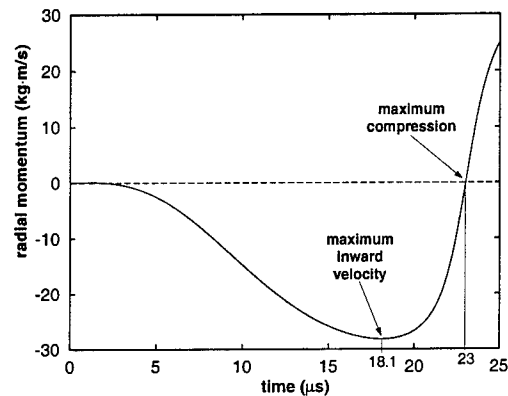

Figure 1 Radial momentum (in a 1-radian slice of the full 2π, axi-symmetric simulation) from a preliminary study. The temperature, velocity and mass density profiles, as well as the magnetic field and current, at t = 18 μs were used as initial conditions for the stability simulations. For the run shown, the maximum inward velocity occurred at t = 18.1 μs and the maximum compression at t = 23 μs.

To reduce computation time, the stability simulations were started at 18 μs, using the results of the preliminary runs as "initial conditions". The temperature, mass density and velocity profiles, as well as the magnetic field and current, at 18 μs were used to initialize the problem. These were run for an additional 5 μs (the case of 64 axial-cells was run for 4 μs) in an Eulerian fashion to prevent "twisting" of the grid. In order to stimulate instability, a sinusoidal mass density perturbation was added throughout the volume of the aluminum. In each case, the perturbation amplitude was ±10% with four complete cycles in the axial direction.

Clear indicators of mixing between the plasma and aluminum melted off the liner are the radiation cooling rate and the

8-6

SIMULATION OF PLASMA-WALL MIXING IN A MAGNETIZED TARGET FUSION CONCEPT

Kenny F. Stephens II

neutron production rate. An emission radiation model was used. It computes the time rate of change of the specific internal energy according to the opacity. The aluminum was allowed to radiate only for cells in which the aluminum density was less than 100 kg/cm^3. The neutron production model considers only those cells that are predominately deuterium. For each such cell, the plasma mass density and temperature are used to compute the number of neutrons produced. This model is not considered to be extremely realistic, but does provide qualitatively acceptable results.

For the Rayleigh-Taylor instability, the fastest growing modes are those with the shortest wavelength. Thus, the cell-size governs which modes will be present in the simulation. Since the proposed MTF geometry has a height of 30 cm, studying a mode with a 125μm wavelength would require at least 240 cells in the axial direction, as well as sufficient cells in the radial direction. Problems with such a large number of cells require extremely long simulation run-times. In order to the reduce the number of cells and shorten the execution time, the height was scaled to much shorter lengths. This change in height reduces the liner inductance and ultimately alters the current flowing through the liner. In order to maintain the same current as would flow through a 30 cm liner, an option was added to MACH2 that scales the inductance and the voltage along the circuit path. This option is called htsclfac and occurs in the contrl namelist (It is applied only to the first circuit element.). Defaulted to 1, htsclfac need only be set if scaling is desired. Using a htsclfac=10 means that a 30 cm problem can be simulated using a simulation height of 3 cm. This reduction in the total number of required cells for a particular resolution allowed significant improvements in execution times.

IV. Simulation Results

To discover when the instability becomes significant, three different axial cell dimensions were considered: 32, 64 and 128 cells per centimeter. Figure 2 shows the radial momentum for each run, including a run with no perturbation

SIMULATION OF PLASMA-WALL MIXING IN A MAGNETIZED TARGET FUSION CONCEPT

Kenny F. Stephens II

and 32 cells per centimeter, and indicates that the perturbation delayed the time at which the liner pinched for each case. However, a significant instability was not obtained until a mode wavenumber of 64π cm^{-1} was considered (i.e., 128 cells per centimeter). The reason for the lack of compression can be discerned from the radiation cooling rate, shown in Figure 3. At ~20.5μs, spikes develop in the radiation caused by aluminum ions sputtering off the liner and mixing with the plasma. These ions then radiate significant amounts of energy and cool the deuterium. Com-
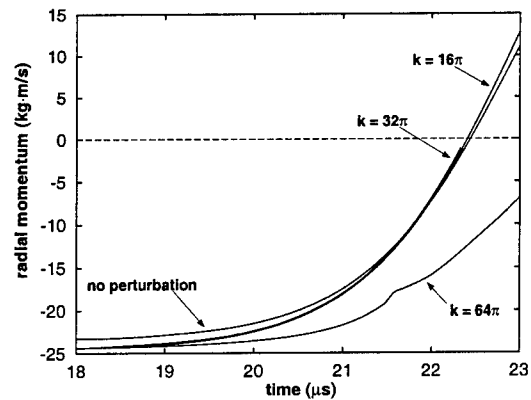
Figure 2 Radial momentum for various Rayleigh-Taylor instability modes. For k = 32π and below, the perturbation has only a minor effect as indicated by the case when no perturbation was applied. For the k = 64π case, the instability is highly evident. The "bump" at ~21.5μs indicates a drop in plasma pressure due to plasma-wall mixing lowering the plasma temperature. The delayed "pinch-time" resulted from a reduced liner inductance which decreased the driving current. The larger momentum values at 18 μs for the perturbed cases is because the perturbation added more mass to the liner compared to the non-perturbed case.
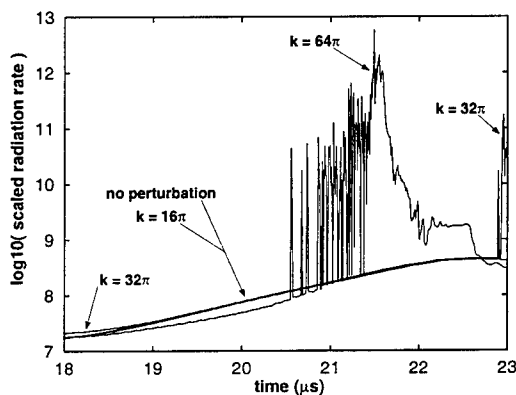
Figure 3 Base-10 logarithm of the scaled radiation cooling rate. The radiation rate is scaled by multiplying the rate by the ratio of problem height to 0.5 cm (the k = 16π and non-perturbed height); this gives each case the same volume properties. The perturbation has essentially no effect on the radiation cooling rate until the k = 64π case. Then, considerable amounts of energy are lost. The reason for the larger radiation rate for the k = 32π at the start and end of the simulation is uncertain. (Wavenumbers are given in terms of 1/cm.)
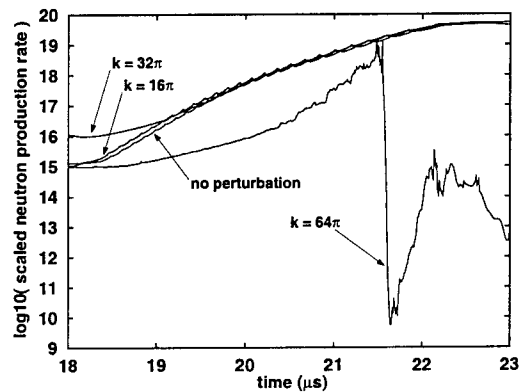
Figure 4 Base-10 logarithm of the scaled neutron production rate. The scaled rate means that the production rate is multiplied by the ratio of problem height to 0.5 cm (the k = 16π and non-perturbed height); this gives each case the same volume properties. At ~21.5 μs, there is a sudden drop in neutron production for the 64π case due to increased radiative losses. The larger production rates for 16π and 32π, compared to the unperturbed rate, are due to larger temperatures prompted by the perturbation; this is probably a result of the method by which the neutron production rate is calculated. (Wavenumbers are given in terms of 1/cm.)

paring the radiation cooling rate and the neutron production rate (see Fig. 4) shows that the plasma has lost sufficient energy that the neutron production drops several orders of magnitude. This drop in plasma temperature results in a loss of plasma pressure. With a lower pressure, the liner experiences less resistance to compress the plasma which

SIMULATION OF PLASMA-WALL MIXING IN A MAGNETIZED TARGET FUSION CONCEPT

Kenny F. Stephens II

causes the change in concavity of the radial momentum at 21.μs, shown in Figure 2. The liner then pinches much later than 22.μs. This is related to the loss of material from the liner, reducing the liner inductance and lowering the driving current. With a lower current, the liner is driven more slowly and thus takes longer to pinch.

V. Conclusion

Magnetized target fusion (MTF) is a promising possibility for break-even fusion production. Although the presented results lack the primary appeal of MTF designs (i.e., magnetized plasma), they are necessary for an adequate understanding for the effects of high-Z contaminants in the plasma; such plasma pollutants can occur even in a magnetized target plasma. The simulations demonstrate that a major source of instability during the compression phase is short-wavelength perturbations. These can result from nonuniform mass density or uneven current flow within the aluminum liner . Furthermore, the complexity of the simulations and the numerous physical processes considered show that MACH2 can successfully simulate complicated phenomena with confidence.

The next step in the MTF modelling process is to magnetize the plasma. MACH2 already has a built-in option (FRC-frese) to supply the desired magnetic configuration. Another consideration would be employing MACH2's material tracking interface. This would allow the liner to be followed in detail during the development of an instability. Also, development of a more discerning neutron production rate routine would allow more quantitative results to be obtained.

Acknowledgment

SIMULATION OF PLASMA-WALL MIXING IN A MAGNETIZED TARGET FUSION CONCEPT

Kenny F. Stephens II

ance from the beginning. As always, I am deeply indebted to Dr. R. E. Peterkin, Jr. Without his help, the joy (and

agony) of MHD and MACH2 would be foreign to me.

Appendix

This appendix contains the MACH2 input deck for the $k = 64\pi$ simulation presented above. It was run using a modified

version 9805. The modifications include a *pwlinear* option for roinit, uinit, vinit and teinit.

```
Scaled MTF. Multigrid. Strength. Eulerian. Perturbation.
pert02
$contrl
  t = 18.0e-6,
  dt = 1.e-15,
  dtmax = 1.0e-10,
  twfn = 23.0e-6,
  cyl = 1.,
  eoson = .true.,
   tsplit = 0,
  radiate = .true.,
   radmodl = 'emission',
  ciron = .true.,
  neutrons = .true.,
  thmldif = .true.,
   anisot = .true.,
   mgmodet = 'converge',
   nthrmax = 2000,
   flxlmt = 0.4,
   tdtol = 1.e-4,
   tdrelax = 1.5,
  bdiff = .true.,
   mgmode = 'converge',
   itmaxrd = 1000,
   rdtol = 1.e-4,
   rdrelax = 1.5,
   aresfdg = 0.05,
   aresvac = 1.e4,
  hallon = .false.,
  magon = .true.,
  brbzon = .false.,
   itpot = 10,
   potrelx = 0.25,
  hydron = .true.,
   theb = 1.,
   volratm = 0.8,
   courmax = 5.0,
   rmvolrm = 0.9,
   itopt = 20,
   mu = 5.6,
   eps = 1.e-6,
  strength = .true.,
  meshon = .true.,
   nsmooth = 4,
   wrelax = 0.25,
   nigen = 0,
   niter = 3,
   eqvol = 1.,
   zeroghcl = .false.,
   multgrd = .false.,
   mglmax = 4,
   trackon = .true.,
   htsclfac = 240.0,
$end
$output
   dtrst = 2.25e-6,
! display every 500
   intty = 'edits,50',
    intty(2) = '0',
   ncyctty = 500,
   dtp = 0.1e-6,
    plot(0) = 'cpt',
     plot(1) = 'grid',
     plot(2) = 'velocity',
      plottype(2) = 'vector',
     plot(3) = 'velocity',
      plottype(3) = 'contour',
      plotcomp(3) = 'vectorz',
     plot(4) = 'ni',
      plottype(4) = 'contour',
      plotcomp(4) = 'scalar',
     plot(10) = 'radheat',
      plottype(10) = 'contour',
      plotcomp(10) = 'scalar',
     plot(15) = 'density',
      plottype(15) = 'contour',
      plotcomp(15) = 'scalar',
     plot(16) = 'pressure',
      plottype(16) = 'contour',
      plotcomp(16) = 'scalar',
     plot(17) = 'thrmflux'
      plottype(17) = 'vector',
```

SIMULATION OF PLASMA-WALL MIXING IN A MAGNETIZED TARGET FUSION CONCEPT

Kenny F. Stephens II

```
  plot(18) = 'material',
    plottype(18) = 'contour',
    plotcomp(18) = 'scalar',
  plot(19) = 'tcone',
    plottype(19) = 'contour',
    plotcomp(19) = 'scalar',
  plot(20) = 'nrate',
    plottype(19) = 'contour',
    plotcomp(19) = 'scalar',
  plot(21) = 'sigfac',
    plottype(19) = 'contour',
    plotcomp(19) = 'scalar',
  kpltreg(1) = 1,2,
  kcon(1) = 11,
  intbound = .false.,
  clabpict = .true.,
  fichfram = 1,
 dtslic = 0.1e-6,
   slice(0) = 'cpt',
    slice(15) = 'tcone',
    slice(16) = 'nrate',
    slice(17) = 'sigfac',
  lblkslic = 1,
   ibdyslic = 4,
   ijslic = 8,
  ncychist = 100,
   histenrg = .true.,
$end
$curnt
 circtype(1) = 'rlc',
! values at t = 18 us
 current(1) = 4.654e6,
 volt(1) = -2.877e4,
 exind(1) = 8.497e-8,
 exres(1) = 1.e-3,
$end
$ezgeom
! height was 30cm
  nblk = 2,
  npnts = 8,
  pointx(1) = 0.0e-2, pointy(1) = 0.000e-2,
  pointx(2) = 2.1e-2, pointy(2) = 0.000e-2,
  pointx(3) = 2.5e-2, pointy(3) = 0.000e-2,
  pointx(4) = 0.0e-2, pointy(4) = 0.125e-2,
  pointx(5) = 2.1e-2, pointy(5) = 0.125e-2,
  pointx(6) = 2.5e-2, pointy(6) = 0.125e-2,
  corners(1,1) = 4,5,2,1,
  corners(1,2) = 5,6,3,2,
$end
$ezphys
  matnamig = 'd',
  siecoldg = -1.e99,
  resmodlg = 'tabular',
  etamaxg = 1.e4,
$end
$matmdl
  matnam(1) = 'd',
! ...except use hydrogen's category 3 table: resistivity, etc.
  mattabs(3,2) = 25252,
```

```
!    ...and in this case use spitzer resistivity.
  resmodl(1) = 'spitzer',
  tcnmodl(1) = 'spitzer',
! setup Al
  matnam(2) = 'al-new',
  resmodl(2) = 'tabular',
  tcnmodl(2) = 'tabular',
  elpmodl(2) = 'steinb-g',
  elpname(2) = 'al-1100',
  rocrad(2) = 1.0e2,
! setup inflow gas
  matnam(3) = 'gas',
  sesanam(3) = 'h',
  eosmodl(3) = 'tabular',
  tcnmodl(3) = 'constant',
  etc0(3) = 1.e4,
  resmodl(3) = 'constant',
  eta0(3) = 1.e4,
$end
$bfield
  momfld = 2.1e-2,
$end
$inmesh
  icells(1) = 42,
  jcells(1) = 16,
  roi(1) = 7.02e-3,
  tempi(1) = 965.2,
   teinit(1) = 'pwlinear',
   teir(1,1) =  0.0, 0.01725, 0.019125,
   teiprfr(1,1) = 1.0, 0.9998, 0.998,
  ui(1) = -3.415e3,
   uinit(1) = 'pwlinear',
   uir(1,1) =  0.0, 0.021,
   uiprfr(1,1) = 0.0, 1.0,
  magxybc(1,1) = 'contnutv',
  magxybc(3,1) = 'contnutv',
  gdvl(1) = 0.0,
   tethrm(1,1) = 0.1,
   rothrm(1,1) = 8.8e3,
  gdvlb(2,1) = 0.0,
   tethrm(3,1) = 0.1,
   rothrm(3,1) = 8.8e3,
  hydbc(4,1) = 'axis',


  icells(2) = 8,
  jcells(2) = 16,
  matnami(2) = 'al-new',
  roi(2) = 2.7e3,
   roinit(2) = 'pwlinear',
   roir(1,2) =  2.1e-2, 2.15e-2, 2.2e-2, 2.3e-2, 2.4e-2, 2.5e-2,
   roiprfr(1,2) = 0.28,  0.65,  1.00,  0.99,  0.97,  0.95,
  tempi(2) = 4.0e-2,
   teinit(2) = 'pwlinear',
   teir(1,2) =  0.021,0.022,0.0225,0.023,0.0235,0.024,0.0245,0.025,
   teiprfr(1,2) = 1.26, 1.00, 1.07, 1.24, 1.47, 1.72, 2.00, 2.15,
  ui(2) = -3.523e3,
   uinit(2) = 'pwlinear',
   uir(1,2) =  2.0625e-2, 2.125e-2, 2.4375e-2, 2.5e-2,
```

SIMULATION OF PLASMA-WALL MIXING IN A MAGNETIZED TARGET FUSION CONCEPT

Kenny F. Stephens II

```
 uiprfr(1,2) = 1.0,     0.979,  0.920,   0.914,
magxybc(1,2) = 'contnutv',
magxybc(3,2) = 'contnutv',
gdvl(2) = 0.0,
 gdvlb(2,2) = 0.0,
 hydbc(2,2) = 'flowthru'
 matbc(2,2) = 'gas',
   roflow(2,2) = 1.e-2,
 tflow(2,2) = 0.2,
 magzbc(2,2) = 'insulatr',
 currcir(2,2) = 1,
 gdvlb(4,2) = 0.0,
ropert(2) = 'roderick',
 roprtam(2) = 0.10,
 roprtmy(2) = 4.0,
 roprtln(2) = 0.125e-2,
binit(2) = 'annulrjy',
 bzi(2) = 109.0,
$end
```

ĭ

SIMULATION OF PLASMA-WALL MIXING IN A MAGNETIZED TARGET FUSION CONCEPT

Kenny F. Stephens II

References

[1] Degnan, J. H. *et al*, in *Proceedings of the Seventh International Conference on Megagauss Magnetic Fields and Related Topics* (1996).

[2] Degnan, J. H. *et al*, *Megagauss IV Proceedings*, p. 699 (1987).

[3] Degnan, J. H. *et al*, *Megagaus V Proceedings*, p. 623 (1990).

[4] Degnan, J. H. *et al*, Fusion Technology **27**, 155 (1995).

[5] Peterkin, R. E., Jr, A. J. Giancola and J. E. Sturtevant, MACH2: A Reference Manul -- Fifth Edition, Phillips Laboratory, July 1992.

[6] Peterkin, R. E., Jr, M. H. Frese and C. R. Sovinec, "Transport of Magnetic Flux in an Arbitrary Coordinate ALE Code", J. Comp. Phys. **140**, p. 148-171 (1998).

[7] Frese, M. H., private communication.

CHARACTERIZATION OF SPATIAL LIGHT MODULATOR FOR ABERRATION COMPENSATION OF SEVERELY DISTORTED PRIMARY MIRROR

Michael V. Wood
Graduate Student
Department Of Electrical Engineering

The Pennsylvania State University
121 Electrical Engineering East
University Park, PA 16802

CHARACTERIZATION OF SPATIAL LIGHT MODULATOR FOR ABERRATION COMPENSATION OF SEVERELY DISTORTED PRIMARY MIRROR

Michael V. Wood
Department of Electrical Engineering
The Pennsylvania State University

Abstract

Spatial light modulators are used in a wide variety of applications ranging from optical computing to display. The application that is of interest for this report is that of real-time holography. A system architecture has been developed that uses a spatial light modulator as a real-time holographic element in a telescope system to perform adaptive optical correction of primary mirror distortions. This allows a less expensive, lightweight primary mirror to be used with little or no degradation of the resulting image. The spatial light modulator is the key element to this system. A phase conjugate projection system is also being investigated for beam collimation/projection applications using a similar inexpensive, lightweight primary mirror.

CHARACTERIZATION OF SPATIAL LIGHT MODULATOR FOR ABERRATION COMPENSATION OF SEVERELY DISTORTED PRIMARY MIRROR

Michael V. Wood

Telescope aberration compensation

Modern telescope designs require the use of large primary mirrors to achieve the high-resolution images desired. In order to maintain the high optical quality necessary for these mirrors, they are generally manufactured as a heavy, monolithic component. Fabrication of such a component is very costly, and transporting it is very difficult. Because of these factors, the size of ground- and space-based telescopes is limited. By using an adaptive optics technique, the optical requirements for the primary mirror can be relaxed so a large, low optical quality primary mirror can be used in conjunction with some compensation optics to achieve high-resolution images with a considerably reduced cost.

One proposed method of adaptive optic compensation for low quality primary mirrors is by using real-time holography with an optically addressed spatial light modulator. This technique uses holographic phase subtraction to remove the aberration of the low quality mirror. Figure 1 shows a conceptual set-up of the holographic phase subtraction technique. A beacon laser probes the mirror and picks up the aberration of the primary mirror, ϕ_a, where $\phi_a = \left(2\pi/\lambda\right)(\text{OPD})$ with λ is the wavelength of the beacon laser and OPD is the optical path difference. The aberrated beacon, $Be^{i\phi_a}$, is interfered with a reference plane wave, B, from the beacon laser to form a hologram. For an amplitude hologram the transmission is proportional to the squared modulus of the illuminating field, given by:

$$T \sim 2 + e^{i\phi_a} + e^{-i\phi_a}$$

This hologram is then illuminated by the aberrated object field, $Ae^{i\Phi}e^{i\phi_a}$ where $Ae^{i\Phi}$ is the undistorted object field. Multiplying the aberrated object beam with the transmission function of the hologram:

$$Ae^{i\Phi}e^{i\phi_a}T \sim 2e^{i\Phi}e^{i\phi_a} + Ae^{i\Phi}e^{2i\phi_a} + Ae^{i\Phi}$$
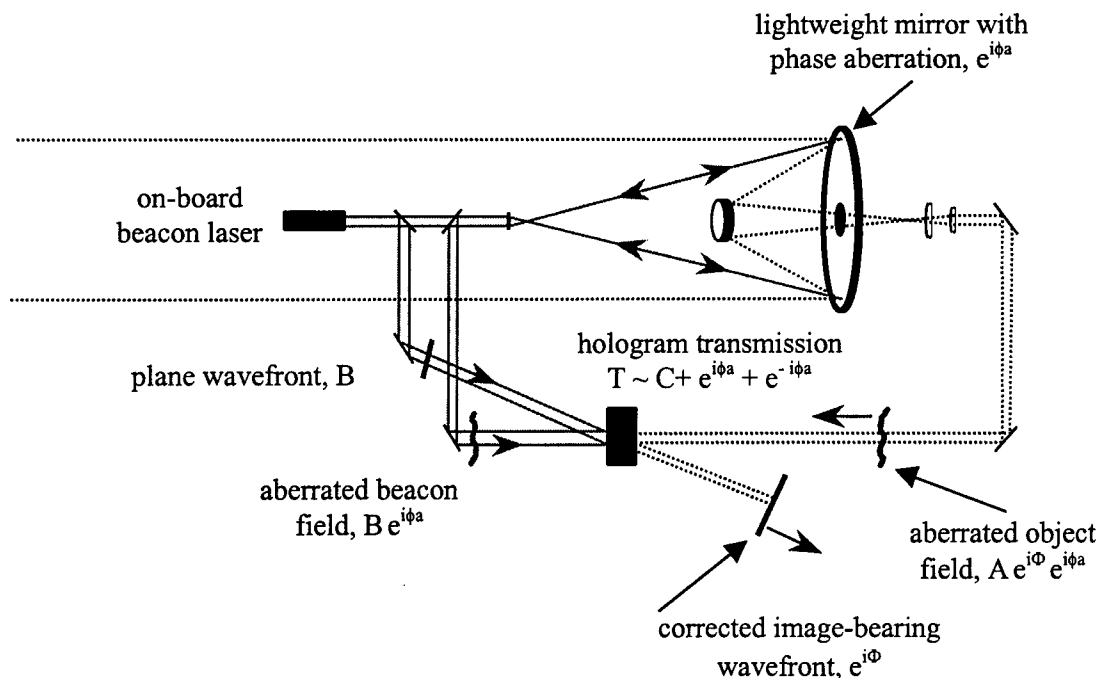
9-3

Figure 1. Schematic of an adaptive optical technique for phase subtraction.

The three terms represent the zero, plus one, and minus one diffracted orders, respectively. The zero order,

proportional to $e^{i\Phi}e^{i\phi_a}$, is the original aberrated object beam transmitted through the hologram. The plus one order,

proportional to $e^{i\Phi}e^{2i\phi_a}$, is the addition of the aberrated phases, creating further distortion. The minus one order,

proportional to $e^{i\Phi}$, is the subtraction of the aberrated phases, leaving only the unaberrated phase information, Φ.

Real-time holographic element

The key component to this whole procedure is the real-time holographic element, the OASLM. There are

several important characteristics to consider when thinking about dynamic compensation of larger aberrations and

severe distortion, namely sensitivity, speed, diffraction efficiency, and resolution. OASLM devices have been used

to compensate for large distortions (hundreds of waves of aberration) with beam intensities as low as 50 μW/cm^2.

Aberration compensation requires that the OASLM react at a speed greater than that at which the aberration

is changing, which is very dependent on the specific application. Nematic liquid crystal limits the response time to

about 30 Hz due to the slow recovery time but devices have been built that have high diffraction efficiency, ~30%. Surface stabilized ferroelectric LC can have a much faster response time, >1kHz, but typically have much lower diffraction efficiency, <10%, because of the low tilt angle of the molecules.

Since the compensated image is found in the first order diffraction, the diffraction efficiency of the OASLM is also a major source of loss. For a phase only sinusoidal modulation the refractive index profile can be written as $\tilde{n} = n + \Delta\tilde{n}\cos qx$. The diffraction efficiency of this index profile is:

$$\eta = |J_1(2\pi\Delta\tilde{n}d/\lambda)|^2$$

where $2\pi\Delta\tilde{n}d/\lambda$ is the phase associated with the transmittance, or half the total phase modulation. With a nematic OASLM operating in the analog phase modulation mode the largest theoretical diffraction efficiency achievable is only about 34% at a phase modulation of about 3.7. In addition, phase modulation occurs for only one polarization direction in nematic liquid crystal, so for unpolarized readout light the diffraction efficiency is reduced to about 15%. If a binary phase grating could be written in a polarization independent material, the diffraction efficiency could theoretically go as high as 40%

The resolution of the OASLM is limited by the diffusion of charges in the photoconductor and by electric field fringing effects in the photosensor, reflecting layer, and liquid crystal layer. The resolution of the OASLM limits the severity of distortion that can be corrected for. It is desirable to have a resolution of greater than 100 line pairs per mm while maintaining high diffraction efficiency, however, commercially available OASLMs have greatly reduced diffraction efficiencies at spatial resolutions above about 30 lp/mm.

A prototype device, which has been built under contract to the US Air Force by the Research Institute for Laser Physics and Peterlab in St. Petersburg, Russia, uses a new type of photoconductor and a deformed helix ferroelectric liquid crystal (DHFLC) in order to improve the resolution, diffraction efficiency and the response time. A schematic of this device is shown in figure 2. The photoconductor is carbon-doped amorphous hydrogenated silicon (α-Si:C:H) which has a very low dark conductivity as well as low carrier diffusion . The liquid crystal layer is a ferroelectric liquid crystal (smectic C*) with a high tilt angle of 40° aligned in deformed helix configuration. The photoconductor allows an increase in the resolution while the DHFLC increases the speed and diffraction
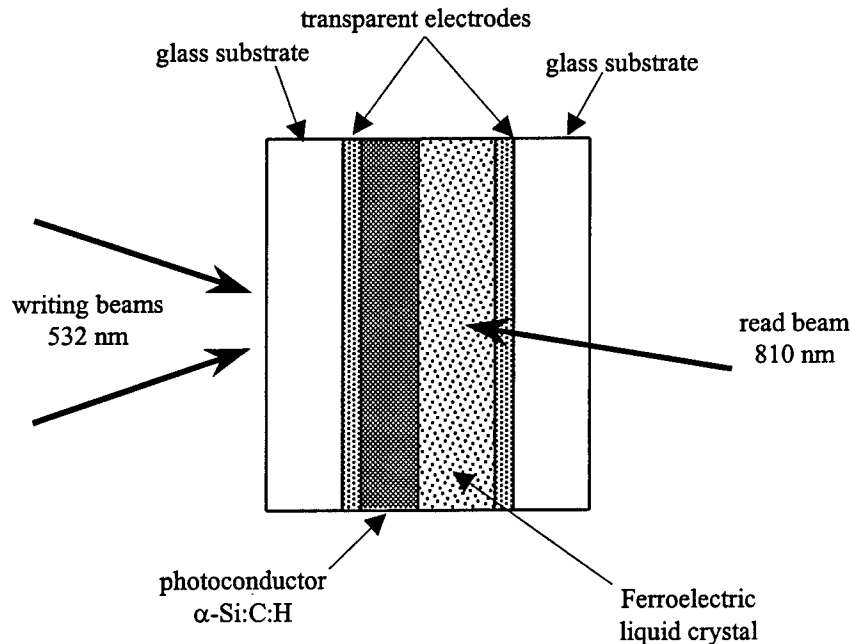
9-5

Figure 2. Schematic depiction of the prototype optically addressed spatial light modulator.

efficiency. In addition, if the high tilt angle of the ferroelectric liquid crystal makes it less sensitive to the polarization of the read-out beam.

This device can operate as a binary phase modulator with the application of a driving voltage and the writing light. Initially the DHFLC is driven to one of its stable states, ±40°, by the application of a large voltage (initialize voltage) across the device, which results in a large electric field across the liquid crystal layer. The polarity of this voltage is arbitrary, the effect is the same regardless of the starting state. Then the voltage is switched to a small, opposite value and the writing light is allowed to strike the photoconductor. Where light hits the photoconductor the local conductivity increases and the electric field across it drops, therefore the electric field across the liquid crystal layer increases and causes the molecules to switch to the other stable state rapidly. This process is illustrated in figure 3. The areas not illuminated by the writing light also switch to the other stable state, albeit on a slower time scale, causing a decay of the written pattern. This decay can be avoided if the entire process is repeated before the molecules in the dark regions have time to completely switch states. The response time of the device is the time it takes to reach maximum diffraction efficiency. The refresh rate of the OASLM is determined by the repetition rate of the device, not by the response time of the liquid crystal itself.
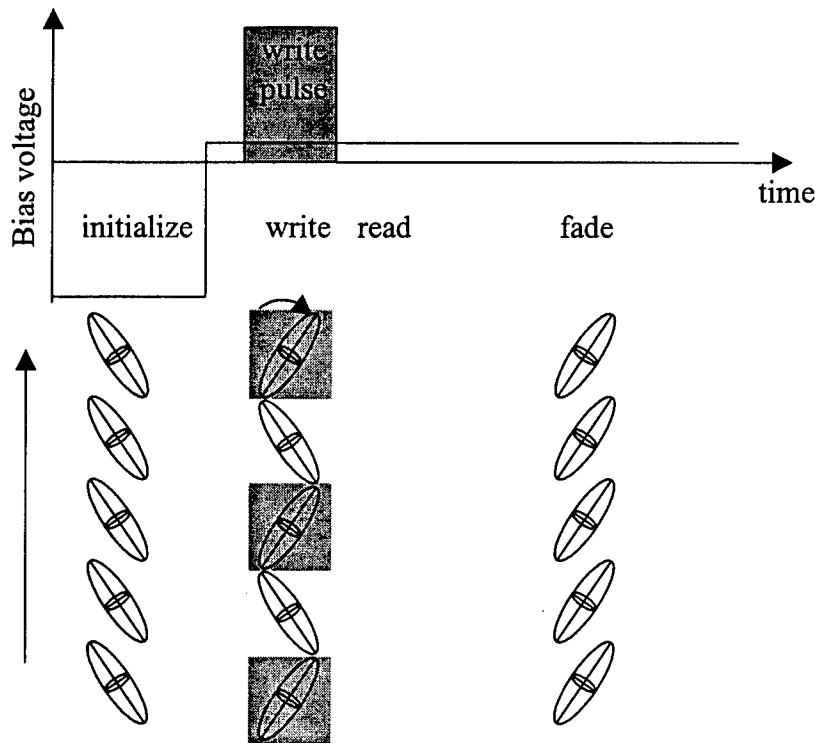
Figure 3. Timing diagram for hologram formation in the prototype OASLM showing the bias voltage, spatial and temporal profile of the writing intensity pulse and the orientation of the index ellipsoid.

Ideally the light regions would switch rapidly and the dark regions would maintain their orientation for an extended time creating a persistent hologram. Physically, however, there is a tradeoff between the response time and the hologram persistence. In order to have a fast response time there must be a large electric field across the liquid crystal. So faster response times require higher applied voltages that also result in higher electric fields in the dark regions and a faster decay rate.

Results

A primary focus of the investigation is the speed and diffraction efficiency of the OASLM when writing and reading a hologram. Figure 4 shows the experimental set-up used to characterize these properties. A doubled Nd:YAG (532 nm) laser was used as the writing beam and a diode laser (810 nm) was used as the readout beam. The two different wavelengths were used because this device doesn't have a reflective layer and must be used in the
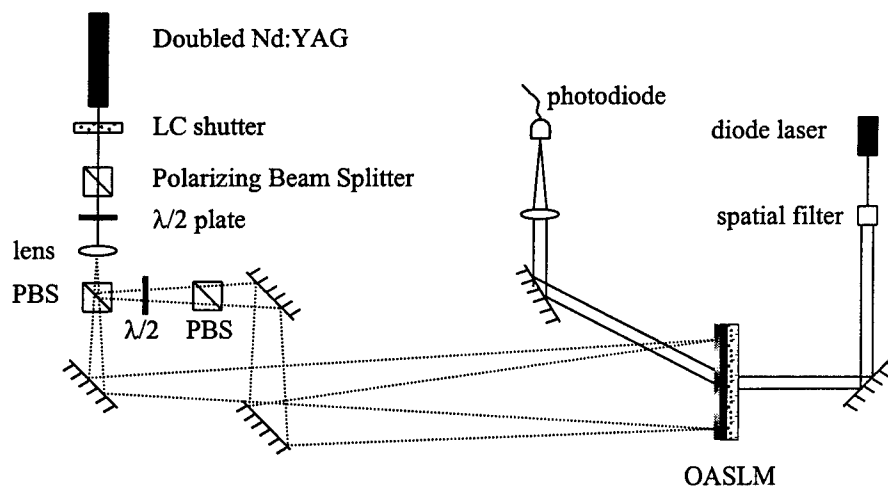
Figure 4. Experimental configuration used for characterizing the prototype
OASLM

transmission geometry. In order to avoid the readout beam being absorbed in the photoconductor and degrading

performance, a higher wavelength was used. The writing beam was passed through a liquid crystal shutter to control

its temporal profile and then defocused and sent through a Mach-Zehnder type interferometer. The two arms of the

interferometer were overlapped on the photoconductor, creating a straight-line interference pattern and phase grating

in the liquid crystal. The readout beam was diffracted from this grating and the temporal dynamics of the first order

were measured using a fast photodiode. Because the device has no anti-reflection coating and there was still some

absorption of the read beam in the photoconductor, the diffraction efficiency is defined as the power in the first

diffracted order divided by the power in the transmitted zero order when there is no grating present.

The resolution of the device is measured by changing the crossing angle of the writing beam and therefore

the spatial frequency of the grating being written and observing the resulting diffraction. The diffraction efficiency

can also be changed by varying the values of the applied voltages and the parameters of the writing pulse. Figure 5

shows a family of curves that were obtained by changing the resolution of the pattern being written on the OASLM.

For these curves, the resolution was set at 350 line pairs / mm and the voltage and write pulse were adjusted to

achieve the maximum peak diffraction efficiency. These settings were then left constant and the resolution was

changed by adjusting the crossing angle of the writing beams. The solid lines represent the diffraction efficiency,

the write pulse is the dotted line and the voltage is the dashed line. The decay in efficiency was discussed earlier
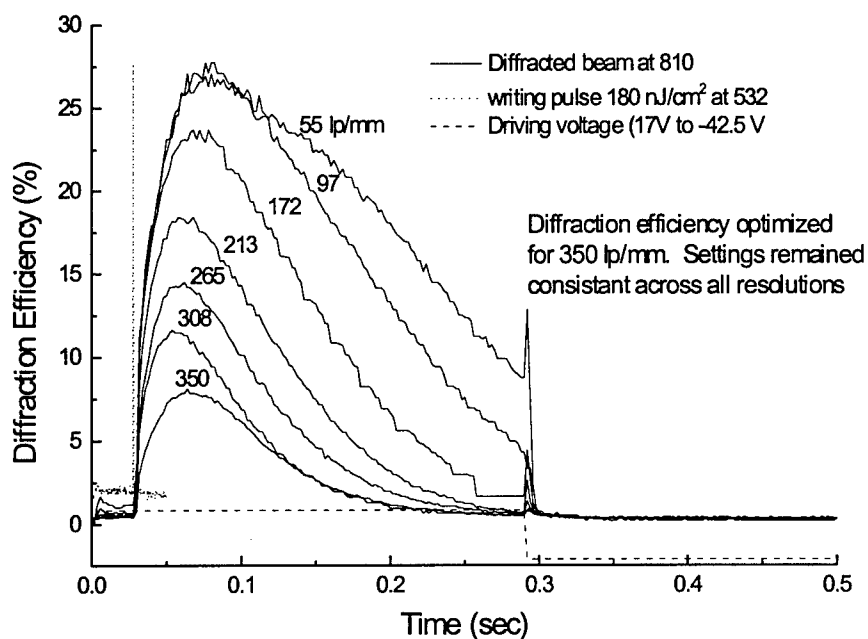
Figure 5. Transient diffraction efficiency as the grating resolution is changed.

(c.f. fig. 3) and the sharp drop-off of efficiency is due to the voltage switching back to the large initializing value. It has been shown that by changing the amplitude, duty-cycle and frequency of the driving voltage it is possible to make the diffraction efficiency nearly constant over the entire read-out time.

Figure 6 shows the maximum peak diffraction efficiency as a function of the spatial frequency of the grating. The maximum peak efficiency was found by making small adjustments to the voltage and write pulse at each spatial frequency. A peak diffraction efficiency of 34% can be attained at 18 lp/mm and at 370 lp/mm a diffraction efficiency of 8% is still achieved. Note that the resolutions were calculated from the angle between the zero order and first order diffracted beams
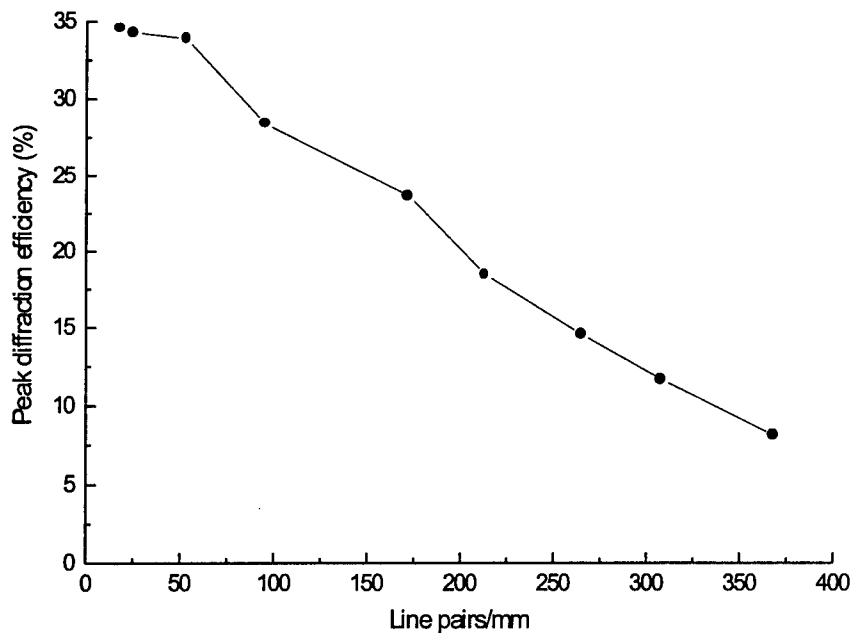
9-9

Figure 6. Maximum peak diffraction efficiency as the spatial grating constant is changed.

Phase Conjugate Projection

It is sometimes desirable to have a large scale beam collimator for use with a telescope system for such uses as illuminating an object. Figure 7 shows a schematic of a system that uses phase conjugation with a large, low optical quality projection mirror to achieve beam collimation. As in the system above, the aberrations of the primary mirror are probed with a beacon laser resulting in a wavefront of $Be^{i\phi_a}$. The aberrated probe beam is then directed into a degenerate four-wave mixing phase conjugate mirror. The phase conjugate of the probe beam, with a wavefront of $Be^{-i\phi_a}$, is projected onto the primary mirror and the aberrations in the conjugate beam cancel the aberrations on the mirror leaving only a plane wave. At this time the investigation of this system is just beginning and there are no publishable results.
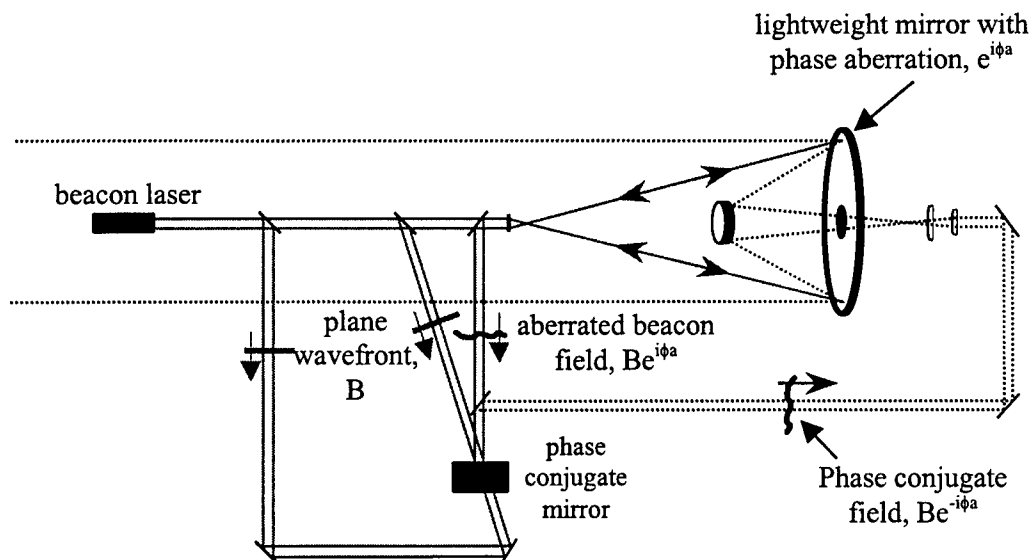
9-10

Figure 7. Schematic of a phace conjugate projection system

Conclusion

For applications involving real-time compensation of large dynamic aberrations requires the use of a spatial light modulator beyond the capabilities of what is currently available commercially. A prototype ferroelectic SLM was built under contract to Phillips Laboratory to meet these capabilities. This deformed helix ferroelectric liquid crystal SLM shows increased diffraction efficiency and a much larger resolution than existing devices. For lower resolutions the diffraction efficiency can be made as high as 33%. In addition to having high diffraction efficiency, the prototype device shows a very high resolution, at 350 line pairs per mm the diffraction efficiency was still near 10%! This device shows characteristics that would make it a very good candidate to be used to compensate for severe aberrations.

References

1. D.V.Wick, T. Martinez, M.T. Gruneisen, and J.M. Wilkes "High Diffraction Efficiency with Sub-milllisecond Response Times from a Deformed Helix Ferroelectric Liquid Crystal Spatial Light Modulator" To be published

2. Mark T. Gruneises, David V. Wick, Ty Martinez, James M. Wilkes, Christopher M. Clayton "Correction of Large Dynamic Aberrations by Real-time Holography using Electro-Optical Devices and Nonlinear Optical Media"

3. M.T. Gruneisen, K.W. Peters, J.M. Wilkes, "Compensated Imaging By Real-Time Holography With Optically Addressed Liquid Crystal Spatial Light Modulators," SPIE Annual Meeting, San Diego, CA, 17 July-1 Aug 1997.

4. U. Efron, *Spatial Light Modulator technology materials, devices, and applications*, Marcel Dekker Inc., New York, NY. 1995

5. M.T. Gruneisen, J.M. Wilkes, "Compensated Imaging By Real-Time Holography With Optically Addressed Spatial Light Modulators," Spring Topical Meeting on Spatial Light Modulators, Lake Tahoe, NV, March 17-19, 1997, Paper StuB5.

6. Hammamatsu technical data sheets for model X5641 PAL-SLM parallel aligned nematic liquid crystal spatial light modulator.